SOLAR FLARE PARTICLE PROPAGATION -- COMPARISON OF A NEW ANALYTIC SOLUTION WITH SPACECRAFT MEASUREMENTS

Thesis by

John Edward Lupton

In Partial Fulfillment of the Requirements

For the Degree of

Doctor of Philosophy

California Institute of Technology

Pasadena, California

1972

(Submitted December 2, 1971)

ACKNOWLEDGMENT

This thesis is to a great extent the result of the guidance of my faculty sponsor, Professor Edward C. Stone. I am grateful for his suggestions and encouragement, and especially for his ability to find time for me within his busy schedule.

My thanks go to Dr. Stephen S. Murray, whose thesis was the predecessor of the work presented here, and whose advice concerning many of the particulars of the OGO-6 experiment was indispensable. Steve was responsible for the calibration of the instrument response to protons, and many of his data analysis programs were borrowed directly for this work.

I would also like to acknowledge Professor Rochus E. Vogt, who is co-investigator on the OGO-6 experiment. Dr. Vogt's support, both moral and technical, is appreciated.

My theoretical efforts were greatly aided by discussions with Caltech Professors J. R. Jokipii, Jon Mathews and Don Cohen, and by talks with Dr. L. A. Fisk of GSFC and Miriam A. Forman of the State University of New York. I also greatly appreciate discussions with Dr. John Fanselow, and with my fellow graduate students Lawrence Evans, Tom Garrard, Alan Cummings, and James Brown.

Special thanks go to my undergraduate helpers Paul Sand, who carried out many of the necessary computer calculations, and Don Gunter, whose constant barrage of questions led to the clarification of many problems.

Caltech's Solar and Galactic Cosmic Ray Experiment aboard OGO-6 was the result of the joint efforts of the personnel of the Space Radiation Laboratory, the Central Engineering Services, the Analog Technology Corporation, TRW Systems, Inc., and the OGO Project Office of the National Aeronautics and Space Administration. Among the Caltech staff, William E. Althouse must be mentioned as that indispensable person who really understands the OGO-6 experiment electronics. Thanks also to Ellen Aguilar and Florence Pickett for their help with the data handling and analysis.

Valuable support for my graduate work at Caltech was provided by an N.D.E.A. Fellowship and a NASA Traineeship. The research work presented here was supported in part by the National Aeronautics and Space Administration under Contract No. NAS5-9312 and Grant Nos. NGR-05-002-160 and NGL-05-002-007.

I am especially grateful to my wife Kathy, whose nimble fingers at the keyboard of the Selectric transformed my scribblings into the pages which follow.

ABSTRACT

A new analytic solution has been obtained to the complete Fokker-Planck equation for solar flare particle propagation including the effects of convection, energy-change, corotation, and diffusion with κ_r = constant and $\kappa_\theta \propto r^2$. It is assumed that the particles are injected impulsively at a single point in space, and that a boundary exists beyond which the particles are free to escape. Several solar flare particle events have been observed with the Caltech Solar and Galactic Cosmic Ray Experiment aboard OGO-6. Detailed comparisons of the predictions of the new solution with these observations of 1-70 MeV protons show that the model adequately describes both the rise and decay times, indicating that κ_r = constant is a better description of conditions inside 1 AU than is $\kappa_r \propto r$. With an outer boundary at 2.7 AU, a solar wind velocity of 400 km/sec, and a radial diffusion coefficient $\kappa_r \simeq$ 2-8 x 10^{20} cm^2/sec, the model gives reasonable fits to the time-profile of 1-10 MeV protons from "classical" flare-associated events. It is not necessary to invoke a scatter-free region near the sun in order to reproduce the fast rise times observed for directly-connected events. The new solution also yields a time-evolution for the vector anisotropy which agrees well with previously reported observations.

In addition, the new solution predicts that, during the decay phase, a typical convex spectral feature initially at energy T_o will move to lower energies at an exponential rate given by $T_{KINK} = T_o \exp(-t/\tau_{KINK})$. Assuming adiabatic deceleration and a boundary at

2.7 AU, the solution yields $\tau_{KINK} \simeq 100h$, which is faster than the measured ~200h time constant and slower than the adiabatic rate of ~78h at 1 AU. Two possible explanations are that the boundary is at ~5 AU or that some other energy-change process is operative.

TABLE OF CONTENTS

LIST OF FIGURES

LIST OF TABLES

I. INTRODUCTION

The study of solar cosmic rays includes several separate areas of interest: the means by which solar particles are accelerated and injected into interplanetary space, the transport and storage of these particles in the solar system, and the problem of particle access to the magnetosphere. The subject of this dissertation, the propagation of solar flare protons, is part of the second of these topics. In particular, near-earth observations of solar flare proton fluxes will be used to develop a more complete representation of the physical processes governing energetic particle transport.

The basic principles underlying the propagation of cosmic rays in the solar system are at the present time fairly well established[1]. The picture of the interplanetary medium with a spiral magnetic field imbedded in an outward-flowing solar wind plasma has won general acceptance[2], and the first observational verification of the diffusion-approximation to cosmic ray motion was made by Meyer, Parker, and Simpson in 1956[3]. More recently, Parker added terms for particle convection and energy-change in the solar wind to the equation for particle diffusion[4]. This Fokker-Planck equation is now widely-used as a description of particle transport in the solar system. In addition, a relationship between the observed fluctuations in the magnetic field and the magnitude of the diffusion tensor has been developed by Jokipii[5,6,7] and others[8,9], and has provided an independent means of estimating the rate of particle diffusion.

Many solutions to the Fokker-Planck equation have been developed in an effort to explain the particle fluxes observed subsequent to solar flare injection. The models proposed have become more and more refined, and analytic solutions now exist which include impulsive injection, anisotropic diffusion (due to the presence of the average magnetic field), convection, and energy-change[10,11,12,13,14]. Despite these developments, none of these solutions have successfully explained all of the observed features of solar flare events. Several important questions remain unanswered: the exact nature of the diffusion tensor and especially its dependence on radial distance and particle energy; the method of particle injection and the possibility of storage near the sun; the possible existence of a scatter-free region extending outward some distance from the sun; the way in which the particles become distributed in solar longitude; and whether or not an outer boundary to the diffusing region exists beyond which particles are free to escape.

The work presented here is a continuation of the process of comparing theoretical solutions with spacecraft observations. Several solar flare particle events have been observed with the Caltech Solar and Galactic Cosmic Ray Experiment aboard NASA's OGO-6 spacecraft. In addition, a new analytic solution has been obtained to the complete Fokker-Planck equation including the effects of convection, energy-change, solar rotation, and anisotropic diffusion using a radial diffusion coefficient independent of distance. The predictions of this new solution have been compared with the observed time-profile of

1-70 MeV protons, with previous measurements by McCracken et al.[15] of the anisotropy in the particle flux, and also with OGO-6 observations of the time-evolution of a feature in the proton energy spectrum. These comparisons show that the model is capable of explaining both the rise and decay phases of "classical" solar flare proton events, and allow one to draw definite conclusions concerning the diffusion tensor, the free-escape boundary, the possibility of a near-sun scatter-free region, and the nature of the energy-change effect.

II. INSTRUMENT

A. General Description

Experiment F-20 aboard NASA's OGO-6 spacecraft is a solar and galactic cosmic ray experiment consisting of 3 separate charged-particle telescopes which share a common electronics package. The device was designed and constructed at Caltech. A complete description of the experiment with particular emphasis on the electronics has been published previously[16].

Although this dissertation is concerned only with the data from the ΔE-Range Telescope portion of the F-20 experiment, some description of the other parts of the instrument are included here for completeness.

The separate charged particle measurements made by the three telescopes are described in Table II-1. By combining measurements of energy loss rate, total energy, range, and velocity, the instrument can separate charges up to Z = 8 and can make accurate measurements of particle incident kinetic energy in the following ranges:

electrons: 200 keV to ~100 MeV

protons and alphas: ~1 MeV/nucleon - 1 GeV/nucleon

lithium-oxygen nuclei: 350 MeV/nucleon - 1 GeV/nucleon.

The incident energy upper limit can be extended by using the geomagnetic field as a particle spectrometer.

Since the experiment uses only 72 bits out of the total 1152 bit OGO-6 main commutator data sequence, cosmic ray data from only one of the three telescopes can be accumulated during each sequence. The electronics package includes a logic and priority subsystem that determines

Table II-1

OGO-6 Experiment F-20 Particle Telescopes

Telescope	Physical Characteristics	Type of Measurement	$A\Omega$ ($cm^2 sr$)	Electron Sensitivity Threshold	Sensitivity to Nuclei	
					Charge Z	Energy* (MeV/nucleon)
ΔE-Range	7 solid state detectors 5 absorbers active collimation with anti-coincidence cup	triple dE/dx, total E, range	0.2 - 1.6	$\gtrsim$200 keV	Z = 1,2	1 - ~300
ΔE - Čerenkov	2 solid state detectors quartz window PM Tube Čerenkov detector active collimation with anti-coincidence cup	double dE/dx, velocity	~2.8	$\gtrsim$3 MeV	Z = 1-8	350 - 1000
Flare	2 solid state detectors 2 absorbers passive collimation with copper shield	double dE/dx, total E, range	~0.02	$\gtrsim$1 MeV	Z = 1,2	18 - 500

*These are the energy intervals in which a measurement of the differential flux can be made.

the manner in which telescopes share the analog-processing and telemetry systems. A set of 7 separate ground-based commands can be given to alter this logic and priority structure. These commands allow the experimenter to disable individual detectors in the event of failure, or if necessary, to completely shut down any of the three telescopes. In addition to the individual telescope event data, the telemetry sequence includes samples of 20 different single detector and coincidence counting rates, and information on ground command status and telescope temperatures.

B. The ΔE-Range Telescope

Since this dissertation involves only low energy proton data from the ΔE-Range Telescope, particular emphasis will be placed on this part of the experiment.

1. Physical Description

A scale cross-section drawing of the telescope is shown in Figure II-1. The device consists of a stack of 7 totally-depleted silicon solid-state detectors and 5 absorbers, with active collimation provided by a cylindrical plastic scintillator cup viewed by a photomultiplier tube. The entrance aperture is covered by a sheet of 3/4 mil aluminized mylar to provide a light shield for the solid state detector stack. An exit aperture at the bottom of the anti-coincidence scintillator cup permits the measurement of the penetrating particle flux.

A list of the relevant stack dimensions and characteristics is provided in Table II-2. Since the investigation discussed here is

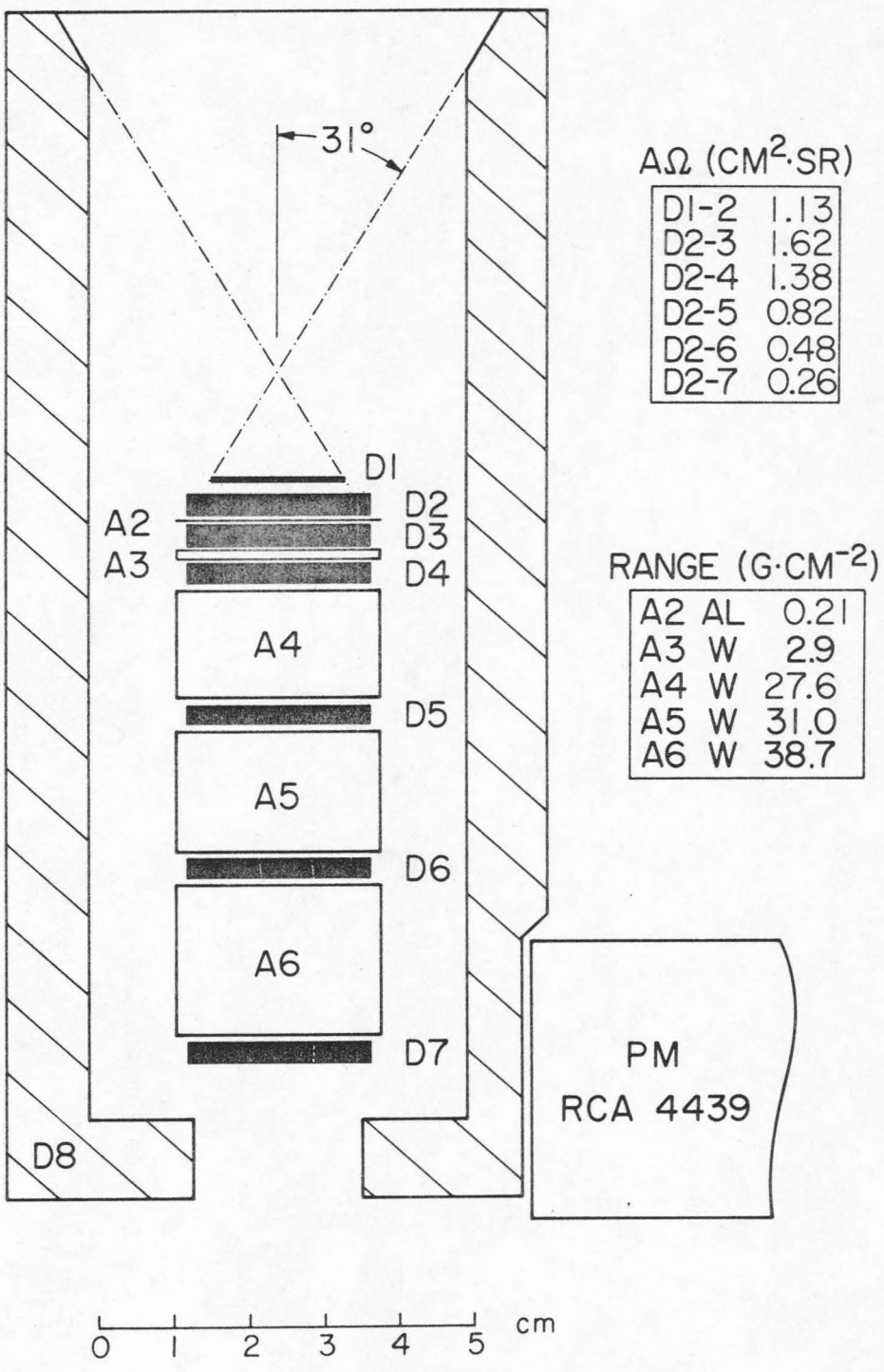

Figure II-1: Scale cross-section drawing of the ΔE-Range Telescope. The AΩ values have ~6% uncertainty due to the uncertainty in the size of the detector sensitive areas. The absorber thickness values are accurate to ±3%. The values listed here were reported in a previous Ph.D. thesis (17).

Table II-2

The ΔE-Range Telescope Stack*

Detector/ Absorber	Material	Thickness mg/cm^2 (±3%)	Sensitive Area cm^2 (±6%)	Discriminator Threshold MeV (±.005 MeV)	Noise MeV (±.002MeV)	Proton Incident Energy Threshold MeV (±3%)
Window	Mylar	2.3	--	--	--	--
D1	Silicon	22.1	2.01	.398	.038	1.17
D2	Silicon	233	3.80	.147	.020	3.3
A2	Aluminum	206	--	--	--	--
D3	Silicon	227	4.08	.153	.021	17.9
A3	Tungsten	2940	--	--	--	--
D4	Silicon	227	3.87	.149	.020	45.2
A4	Tungsten	27570	--	--	--	--
D5	Silicon	236	4.01	.142	.022	152
A5	Tungsten	30980	--	--	--	--
D6	Silicon	227	4.08	.141	.023	230
A6	Tungsten	38730	--	--	--	--
D7	Silicon	236	4.08	.148	.022	309

*The values listed here were reported in a previous Ph.D. thesis[17].

concerned with protons below 150 MeV indicent energy, only detectors D1 through D4 will be discussed in detail. Particle energy-loss can be measured in detectors D1, D2, and D3 using three separate pulse-height analyzers, while triggers in detectors D4 through D7 are used to indicate particle range. When the experiment is in the normal operating command mode, either a $D1\overline{D8}$* or a $D2D3\overline{D8}$ trigger will initiate pulse-height analysis. The D8 anti-coincidence shield not only provides collimation for the telescope, but also rejects undesirable interaction and shower-type events which scatter particles into the scintillator. For protons below 45 MeV incident energy, a triple energy-loss measurement is recorded in D1, D2, and D3. When any of the "range detectors" D4 through D7 are triggered, this range information replaces the D1 pulse height in the readout sequence.

Because of its high ~400 keV discriminator threshold and small depletion depth, detector D1 has less than 1% electron detection efficiency for any incident electron energy[18,19]. The problem of separating low energy electrons from nuclei is thus easily solved even for particles which stop in D1.

2. Detectors

The seven solid-state detectors used in the range stack are all totally-depleted silicon surface-barrier type devices manufactured especially for Caltech by ORTEC (Oak Ridge Technical Enterprises Corp.).

---

*The notation $D1\overline{D8}$ is used to indicate a D1 trigger in the absence of a D8 trigger. D8 is thus in "anti-coincidence." In the same way, $D2D3\overline{D8}$ means a D2-D3 coincidence in combination with a D8 anti-coincidence.

With the exception of D1, they have a nominal 1000 μm depletion depth and 4.0 cm^2 sensitive area. Surface-barrier detectors were used because they have low noise and high reliability in a variety of environments, and because they have high resistance to radiation damage from energetic particles. In the case of D1 and D2, surface barriers were particularly desirable because they can be manufactured with very thin dead regions which allows an accurate measurement of particle total energy.

The detectors used in the experiment flight unit were carefully selected on the basis of thickness, sensitive area, bias voltage needed for total depletion, noise at full bias, and performance in a thermal-vacuum environment. Since such devices cannot withstand any physical contact from micrometers, fingers, etc., all physical measurements were made in a "remote" fashion using energetic particles. The sensitive area and total thickness were determined by irradiating each detector with a well-collimated monoenergetic electron beam from a magnetic β-ray spectrometer. More exact thickness measurements were made for D1, D2 and D3 when the completed flight unit was exposed to 1 - 23 MeV protons from Caltech's Tandem Van de Graaff accelerator. Determinations of dead layer thickness and proper operating bias voltage were made by exposing each detector surface to ThB(Pb^{212}) alpha particles. The most important test consisted of a two-week thermal-vacuum exposure for each detector at full bias voltage. During the two weeks the detector noise and leakage current were recorded frequently; an environment of $<10^{-6}$ torr and $+40^{o}C$ was maintained.

Each detector in the operating experiment has a pulse-height discriminator threshold associated with it that has been carefully adjusted to reject detector noise but include all appropriate particle pulses (see Table II-2). This threshold, which is clearly a function of both detector thickness and noise level, was set (for all detectors except D1) so that 99% of all minimum-ionizing particles cause a trigger.

3. Anti-coincidence Shield

The anti-coincidence cup consists of a cylinder of NE 102 plastic scintillator material viewed by a RCA 4439 photomultiplier tube. The PM tube was tested using a Cs^{137} source in combination with a NaI crystal to determine the optimum operating bias voltage. The discriminator was set using ground level muons incident on the assembled D8 scintillator so that at least 99% of these minimum ionizing particles cause a D8 trigger. Although this D8 threshold corresponds to only ~400 keV energy loss in the scintillator, the presence of an aluminum housing which surrounds the scintillator raises the D8 incident energy threshold to ~9 MeV for protons and 0.6 MeV for electrons. Thus the anti-coincidence cup acts as a mechanical collimator at low energies.

4. Electronics

The electronics package, which has been described in detail elsewhere[16], consists of the following separate subsystems:

1) ΔE-Range telescope electronics
2) Čerenkov telescope electronics
3) Flare telescope electronics

4) Analog signal processor

5) Coincidence and priority logic

6) Rate accumulators

7) Data storage, formatting, readout, and spacecraft interface

8) Power supply

A block diagram of the electronics relevant to the ΔE-Range Telescope is shown in Figure II-2. Pulses produced in each detector are passed through a charge-sensitive preamplifier, a shaping amplifier, and finally to a pulse-height discriminator. If the pulse is above the discriminator threshold, a logic pulse is generated which is passed to the coincidence and priority logic subsystem, which in turn decides whether the event should be blessed with analysis by the analog processor. If the decision is yes, then the logic subsystem opens the linear gates and the analog signals are digitized by the three 256-channel pulse height analyzers. The logic also passes the appropriate single detector and coincidence rates to the rate accumulator subsystem. The pulse-height data, range detector information, and rates are all read out once during each 143 msec interval during normal spacecraft operation.

Fourteen single detector rates and six coincidence rates are accumulated. Since only two rates are sampled during a given readout interval, a commutation sequence is employed to determine how the available telemetry is shared by the rate scalers. The rates pertinent to the range telescope are listed in Table II-3.

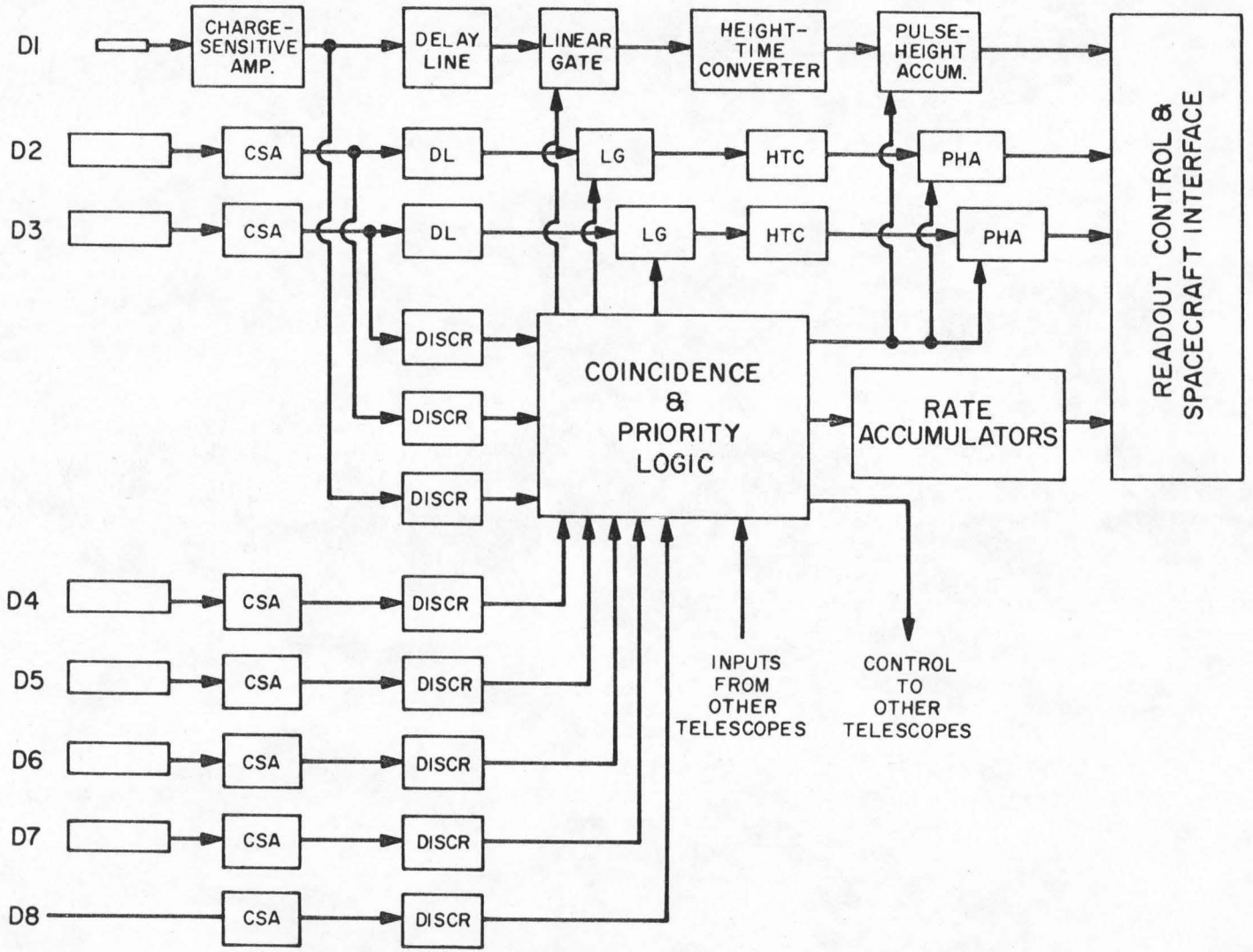

Figure II-2: ΔE-Range Telescope Electronics Block Diagram

Table II-3

ΔE-Range Telescope Detector Rates

Rate	Accumulation Period*	Elapsed time between readouts*	Contributing Particles	$A\Omega(cm^2 sr)$ ($\pm$6%)
$D1\overline{D8}$	430.9 msec	432 msec	protons ~1 to ~20 MeV	1.1
$D2\overline{D8}$	430.9 msec	432 msec	protons $\gtrsim$ 3 MeV electrons $\gtrsim$ 0.2 MeV	1.8
$D1D2\overline{D8}$	430.9 msec	6912 msec	protons ~3 to ~20 MeV	1.1
$D2D3\overline{D8}$	430.9 msec	432 msec	protons $\gtrsim$ 18 MeV electrons $\gtrsim$ 1.1 MeV	1.6

*assuming normal spacecraft readout rate of 8000 bits/sec

As mentioned previously, all three telescopes compete for the use of the analog-processor and telemetry. During normal command-mode operation, the Flare telescope has highest priority, while the Range and Čerenkov telescopes compete on an equal basis at a lower priority level. Thus the Flare telescope, which is a miniature version of the Range telescope with passive instead of active collimation, begins to dominate the analysis as the particle flux reaches the saturation levels for the Range and Čerenkov telescopes. This priority system can be altered easily by means of the seven separate ground commands available. Table II-4 lists the ground based command combinations which are pertinent to the operation of the Range telescope, and shows how these commands affect the logic and priority structure.

5. Electronics Calibration

The basic principle behind the use of solid-state detectors is that the charge pulse produced at the detector terminals is proportional to the energy deposited in the active detector volume by the charged particle. In order to convert digital pulse height data into particle energy loss information, one must know the values of the thresholds of all the PHA channels in units of MeV of particle energy loss.

The calibration of the pulse-height analyzers was carried out as a two-step process. First the voltage pulses from a Berkeley Tail Pulse Generator were applied across a separate test capacitor at the input of each charge-sensitive preamplifier. By varying the height of this voltage test pulse and observing the pulse height analyzer output,

Table II-4

Ground-based Commands for the ΔE-Range Telescope

Command Number	Command Name	Triggering Logic for Analog Processor	Comment
C7	System Reset	$D1\overline{D8}$ or $D2D3\overline{D8}$	Normal mode
C4	D1 disable	$D2D3\overline{D8}$	Given if D1 fails
C5	D3 enable	$D1\overline{D8}$ or $D3\overline{D8}$	Given if D2 fails
C6	D2 enable	$D1\overline{D8}$ or $D2\overline{D8}$	Given if D3 fails or for electron data accumulation
C4C5	--	$D3\overline{D8}$	Only $D3\overline{D8}$ triggers analysis
C5C6 or C4C5C6	--	--	Range telescope shut-down

the threshold value of each analyzer channel was determined in units of pulser mV. In a similar way the discriminator threshold in pulser mV was determined for each detector.

The second step involved the conversion of pulser mV to energy loss in keV, which is equivalent to determining the value of the individual test capacitors. This was achieved by irradiating each detector with ThB alpha particles (with energies of 6.045, 6.083, and 8.776 MeV), and comparing these particle-produced pulses with those of the test pulser. The PHA and discriminator thresholds were thus determined to an accuracy $\lesssim 1\%$ for temperatures between $-5^{\circ}C$ and $+40^{\circ}C$. Typical analyzer channel widths are ~50 keV, yielding a saturation value of ~13 MeV for each of the 256-channel analyzers.

Tests of the logic and priority structure, command modes, and rate scalers were also made using the ground support equipment. A more detailed description of all the electronics test procedures has been given in a previous Ph.D. thesis[17].

C. Spacecraft

1. The Satellite Orbit

The OGO-6 spacecraft is the last in a series of Orbiting Geophysical Observatories flown by NASA. It was launched on June 5, 1969 into a polar orbit described by the following parameters:

perigee	397 km
apogee	1098 km
inclination	82°
period	99.8 minutes

Caltech's experiment F-20, which is one of 26 independent experiments aboard the satellite, is mounted on the -Z door so that the telescope entrance apertures always face away from the earth.

The satellite orbit can be pictured as nearly fixed in space with the earth rotating beneath. The earth's rotational axis is tilted 8^{o} out of the plane of the spacecraft orbit, so that the satellite never reaches a *geographic* latitude greater than 82^{o} N or S. When the satellite crosses the geographic equator from south to north, this is taken conventionally as the beginning of a new revolution. Each of the ~14 revolutions per day are numbered consecutively throughout the life of the satellite.

Since low energy cosmic ray particles have access to the earth's magnetosphere only in the vicinity of the north and south magnetic poles[20], the location of the satellite orbit in the polar regions is of particular interest. Figure II-3 shows a series of orbits over the south geographic pole spanning a full day in universal time.

2. Invariant Latitude and Magnetic Local Time

Since it is the geomagnetic field that defines the cosmic ray access regions, a coordinate system aligned with the magnetic dipole axis of the earth is commonly used to define the spacecraft location. One approach is to merely set up a spherical polar coordinate system centered on the dipole axis, and to then measure the satellite position in terms of *dipole latitude* and *dipole longitude*. Because the earth's field is distorted from a true dipole both by the presence of higher order moments in the source and by the external influence of the solar

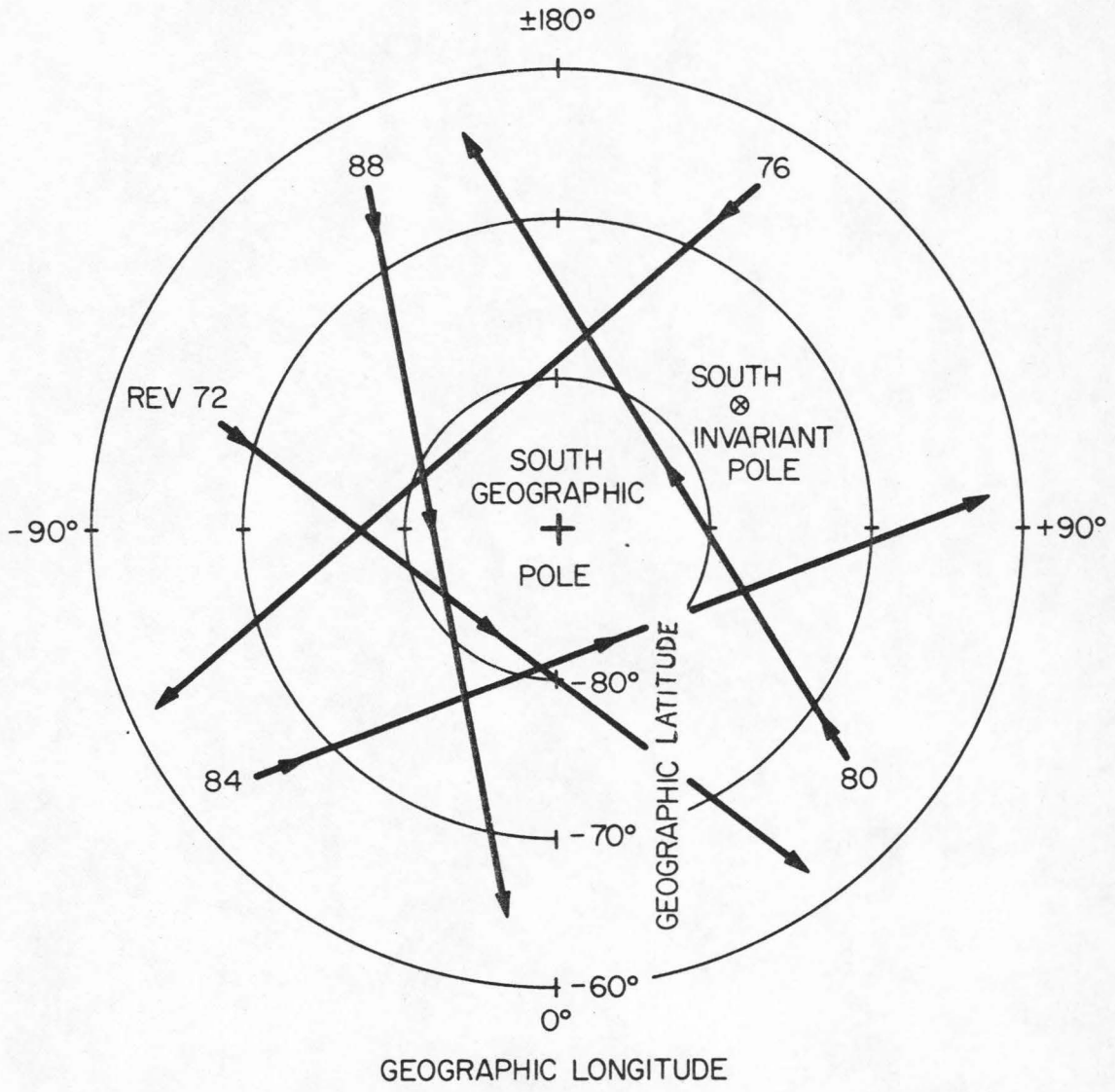

Figure II-3: Typical orbital trajectories for OGO-6 across the south pole in geocentric coordinates. The south invariant pole is the point at which $\Lambda = 90^{o}$.

wind, a non-spherical coordinate system using *invariant latitude* Λ, and *magnetic local time* MLT, has been found to be more appropriate[21, 22]. These quantities are defined as follows:

$$\text{MLT} = \begin{pmatrix}\text{dipole longitude}\\ \text{of spacecraft in}\\ \text{hours}\end{pmatrix} - \begin{pmatrix}\text{dipole longitude}\\ \text{of earth-sun line}\\ \text{in hours}\end{pmatrix} + 12 \text{ hours}$$

$$\Lambda = \begin{pmatrix}\text{dipole latitude adjusted for}\\ \text{distortions of the geomagnetic}\\ \text{field from a true dipole}\end{pmatrix}$$

The value of the invariant latitude Λ for a deformed geomagnetic line of force is defined to be the same as the dipole latitude of the equivalent undistorted "dipole" line of force. Note that any distortion of the field lines in the azimuthal direction is neglected by the MLT parameter. When the spacecraft is in the magnetic meridian plane that contains the earth-sun line, it is at MLT = 1200 hours.

Figure II-4 shows the orbits of the previous figure plotted in the Λ - MLT coordinate frame. Since the rotational and magnetic poles differ in latitude by ~11.5°, the orbit covers most values of Λ during a 24-hour period. Note that the *direction* in which the spacecraft crosses the Λ - MLT plane is roughly constant with time. This coverage region rotates slowly at the rate of ~1.8°/day, and the spacecraft thus covers the entire Λ - MLT plane once every 100 days.

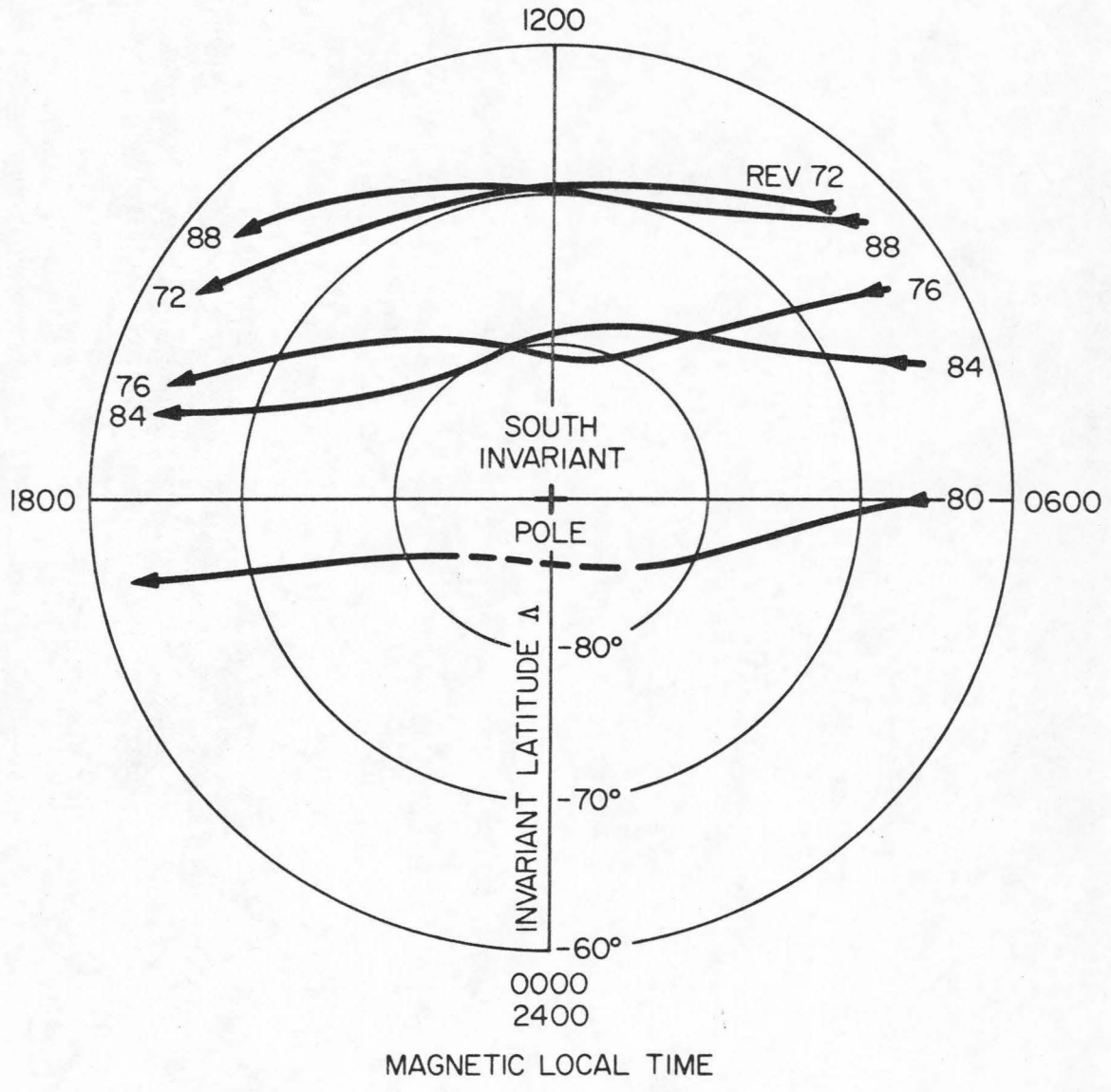

Figure II-4: Typical orbital trajectories for OGO-6 across the south pole in Λ-MLT coordinates. The dashed line indicates where interpolation was necessary to determine the trajectory.

III. DATA ANALYSIS

This section describes the manner in which the raw data produced by the F-20 Experiment are converted to useful information about the intensity and composition of the cosmic ray particles in the vicinity of the OGO-6 spacecraft.

A. Proton Response of the ΔE-Range Telescope

Using the results of the electronics calibration of the analog-processors, one can convert a digital pulse height into a value for the particle energy-loss in the detector depletion region. Given a double or triple energy-loss measurement for a single particle event, the problem remains to determine the particle charge Z and incident kinetic energy E. The following is a discussion of how this problem is solved for D1 through D4 proton events in the Range Telescope.

1. Accelerator Calibration

A straightforward way to determine the response of a cosmic ray telescope to low energy protons is to simply expose the device to a monoenergetic proton beam and observe the response directly. Such an experiment has in fact been performed on the assembled F-20 flight unit using Caltech's Tandem Van de Graaff accelerator. Although the primary proton beam of the Caltech accelerator is limited to 12 MeV energy, 23 MeV protons can be produced by means of the $B^{10}(He^3,p)\ C^{12}$ reaction. A magnetic spectrometer was used to select the desired beam energy and also to limit the energy spread to $\Delta E/E \simeq 1\%$. The Ground

Support Equipment was used to simulate the experiment-spacecraft interface and to write the digital data on magnetic tape.

After some analysis, the incident proton energies needed to penetrate to the top of D1, D2, A2, D3, and A3 (see Figure II-1) were determined precisely. This information, in combination with the range-energy tables for protons in mylar, silicon, aluminum, and tungsten[23], yielded an accurate thickness measurement for the Mylar window and for detectors D1, D2, and D3. Analysis of the pulse-height data from the accelerator runs also determined the most-probable pulse height combinations in D1, D2, and D3 for various incident proton energies. A detailed description of the Tandem Van de Graaff calibration has been given by S. Murray[17].

2. Proton Energy-Loss Calculation

A calculation of the instrument response to protons can be made independent of an actual accelerator calibration by using the thickness values for the various layers in the telescope and the range-energy tables[23]. In particular, the average energy loss $\langle \Delta E \rangle$ in a given detector can be calculated as a function of incident energy E. These calculated proton and alpha particle energy loss curves for D1, D2, and D3 are shown in Figure III-1. Note that the D1 - D2 energy-loss combination uniquely determines the particle species and energy from 3 to ~40 MeV/nucleon, while the D2 - D3 combination covers the region above ~18 MeV/nucleon incident energy.

If these calculated curves for the most probable proton energy-loss are combined with the electronics calibrations of the pulse-height

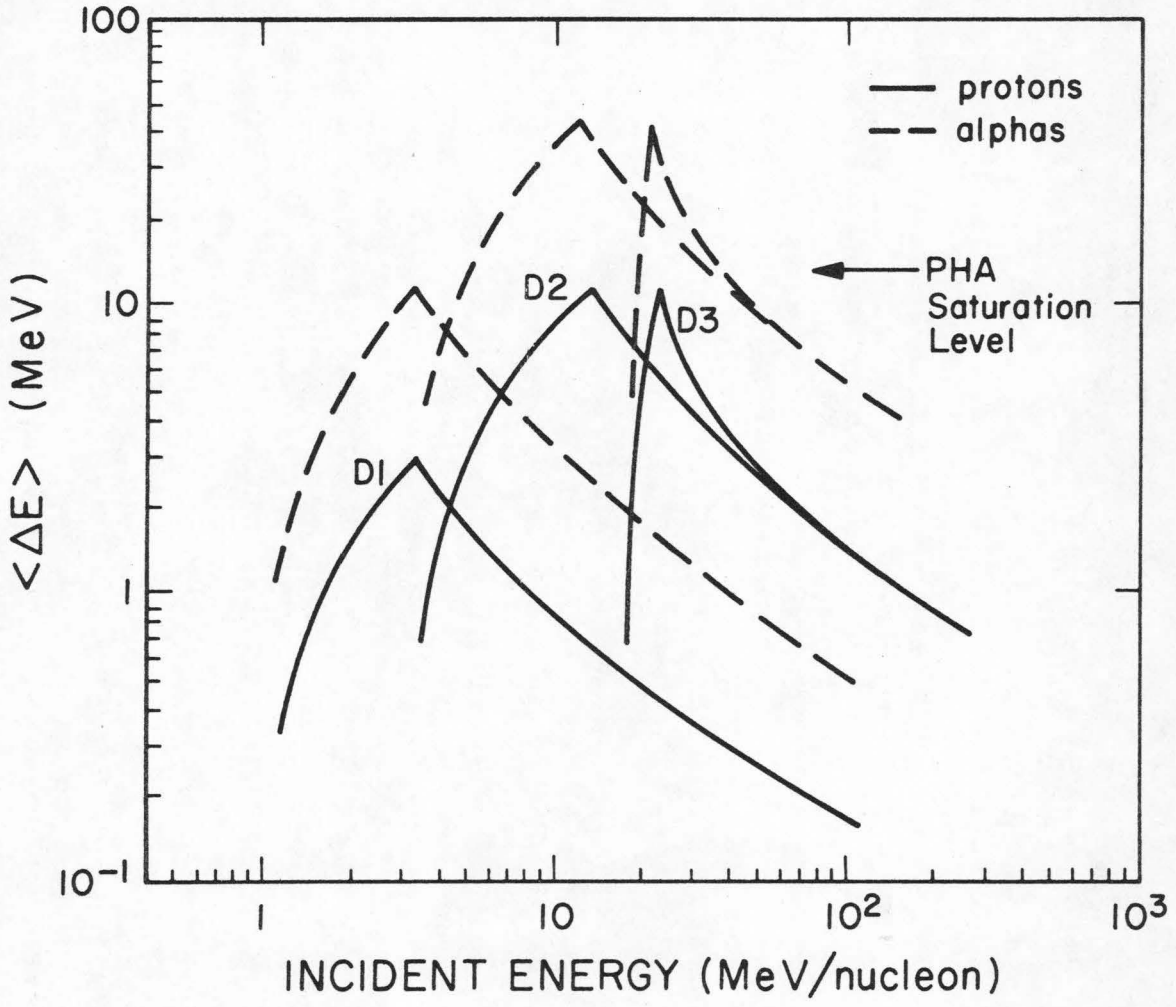

Figure III-1: Calculated average energy loss <ΔE> in various Range Telescope detectors as a function of incident kinetic energy. The calculation is based on the Janni range-energy tables.

analyzers, then estimates can be made of the expected pulse height channel combinations in D1, D2, and D3 for a given proton incident energy. These calculated digital pulse height values for D1 vs. D2 are shown in Figure III-2. The locations of the most-probable pulse heights from the accelerator calibration runs are plotted for comparison. The agreement is very good, indicating that the energy-loss tables can be used to extrapolate beyond the 23 MeV limit of the Tandem Van de Graaff runs. A similar plot for D2 vs. D3 pulse height is shown in Figure III-3. The agreement between the energy-loss calculations and the accelerator runs is again good, and the calculated values are shown extended to 150 MeV incident proton energy.

3. Pulse Height Data Reduction

The comparison between calculation and experiment just described represents a consistency check between the values for the detector and absorber thicknesses, the energy-loss thresholds of the pulse-height channels, the range-energy tables, and the actual instrument response to protons. This indicates that the telescope proton response is well-understood, and that a given D1-D2-D3 event can now be easily associated with a specific particle species and incident energy.

The dashed lines in Figures III-2 and III-3 are proton regions or bands which have been determined empirically to include essentially all of the proton pulse-height events. Figures III-4 and III-5 show 2-dimensional printouts of actual satellite pulse-height data accumulated during a 10-minute interval on 3 November 1969. The same proton bands have been superimposed, and they do indeed surround the events

Figure III-2

Proton response plotted on the 2-dimensional D1 vs. D2 pulse-height plane. The numbers denote incident proton kinetic energy in MeV. The crosses are the most-probable D1-D2 pulse-height pairs derived from the results of the Tandem Van de Graaff accelerator calibration. The dots are the results of the average energy-loss calculation based on the Janni range-energy tables and on the best estimates for the Range Telescope detector and absorber thicknesses. The dashed line defines a proton "band" which includes essentially all valid proton events.

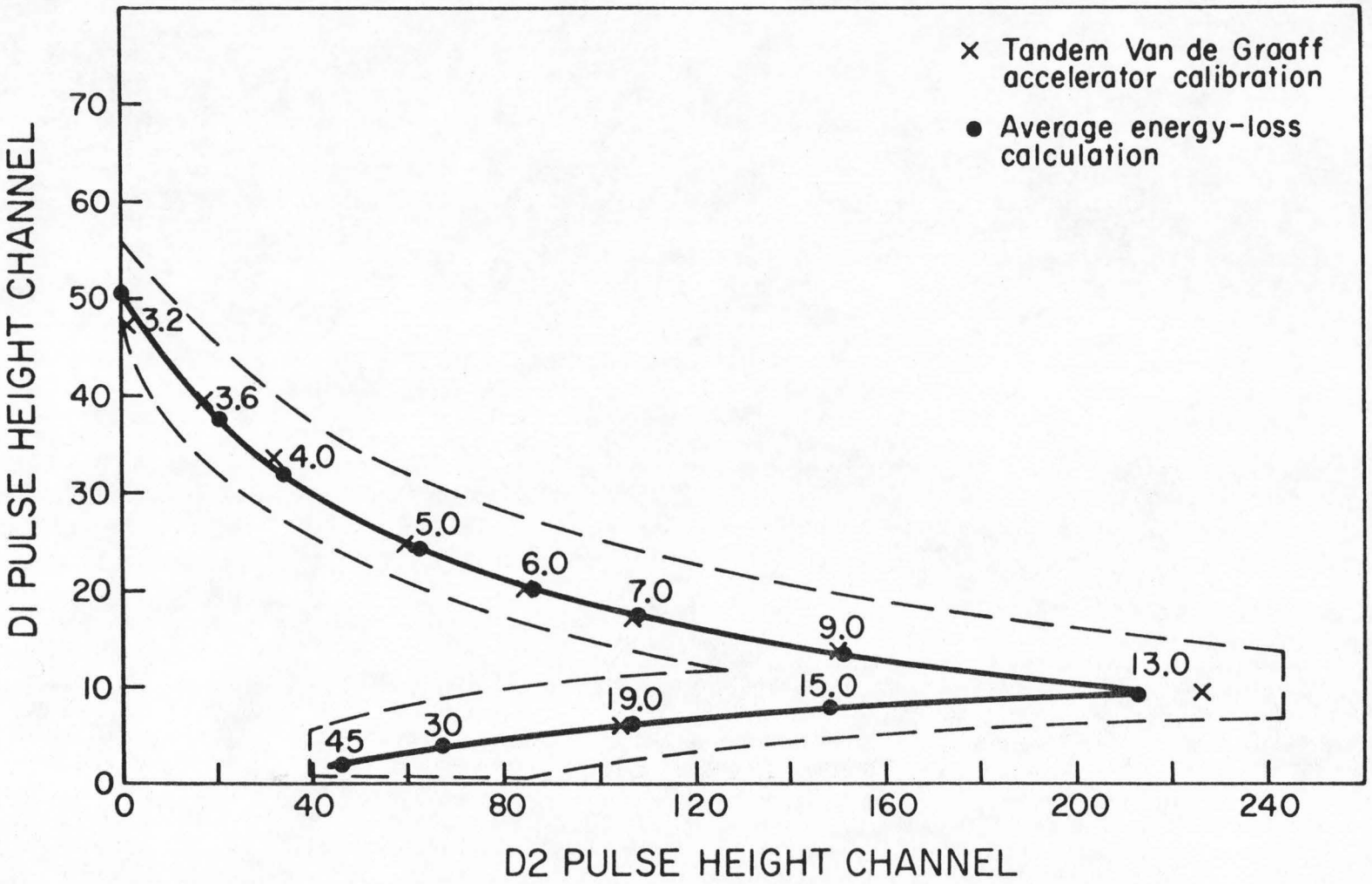
× Tandem Van de Graaff accelerator calibration
● Average energy-loss calculation
D1 PULSE HEIGHT CHANNEL
D2 PULSE HEIGHT CHANNEL
0
10
20
30
40
50
60
70
0
40
80
120
160
200
240
3.2
3.6
4.0
5.0
6.0
7.0
9.0
13.0
15.0
19.0
30
45

Figure III-3

Proton response plotted on the 2-dimensional D2 vs. D3 pulse-height plane. The numbers denote incident proton kinetic energy in MeV. The crosses are the most-probable D2-D3 pulse height pairs derived from the results of the Tandem Van de Graaff accelerator calibration. The dots are the results of the average energy-loss calculation based on the Janni range-energy tables and on the best estimates for the Range Telescope detector and absorber thicknesses. The dashed line defines a proton "band" which includes essentially all valid proton events.

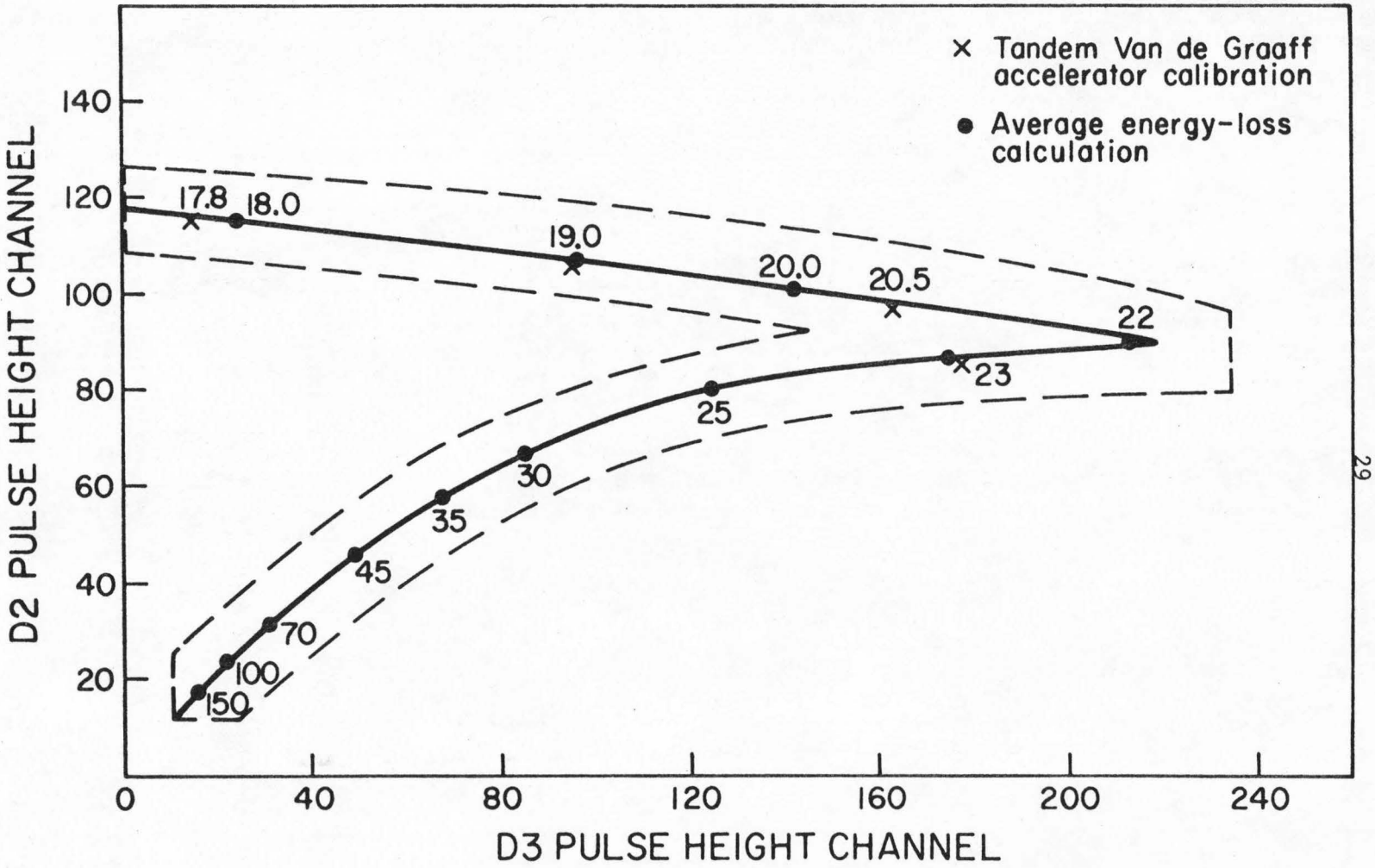
× Tandem Van de Graaff accelerator calibration
● Average energy-loss calculation
D2 PULSE HEIGHT CHANNEL
D3 PULSE HEIGHT CHANNEL
140
120
100
80
60
40
20
0
40
80
120
160
200
240
17.8
18.0
19.0
20.0
20.5
22
23
25
30
35
45
70
100
150

Figure III-4

The D1 vs. D2 pulse height array observed during a polar pass on 3 November 1969. The numbers indicate the total number of events which occurred with a particular D1-D2 pulse height combination. The PHA channel numbers are pseudo-logarithmic (256 actual channels have been compressed into 60). The boundary of the proton band and the calculated locus for α-particles have been superimposed. The exact nature of the pulse-height scales and event number code is explained in reference 17.

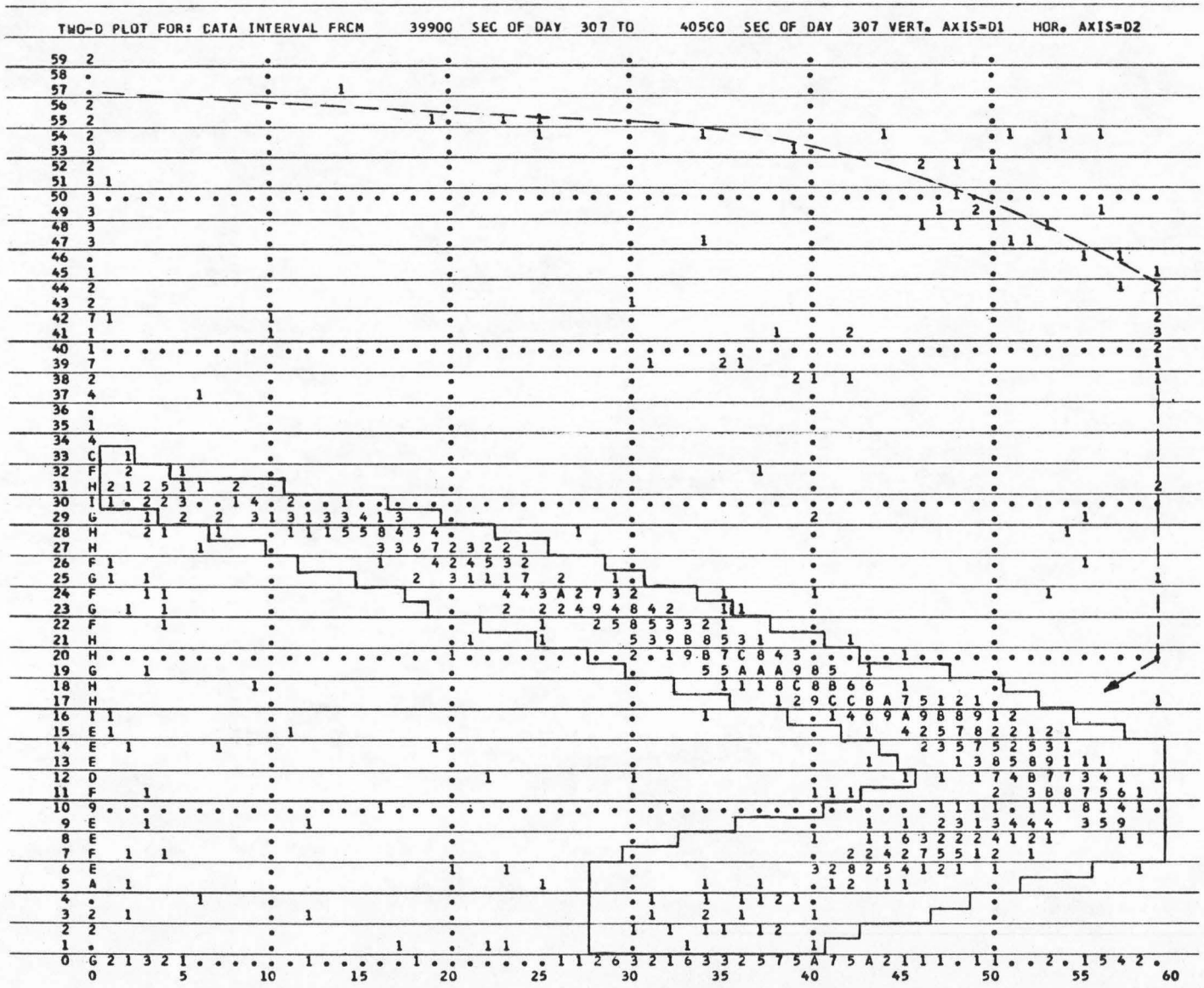
TWO-D PLOT FOR: DATA INTERVAL FROM 39900 SEC OF DAY 307 TO 40500 SEC OF DAY 307 VERT. AXIS=D1 HOR. AXIS=D2
0 5 10 15 20 25 30 35 40 45 50 55 60

Figure III-5

The D2 vs. D3 pulse height array observed during a polar pass on 3 November 1969. The numbers indicate the total number of events which occurred with a particular D2-D3 pulse height combination. The PHA channel numbers are pseudo-logarithmic (256 actual channels have been compressed into 60). The boundary of the proton band has been superimposed for comparison. The exact nature of the pulse-height scales and event number code is explained in reference 17.

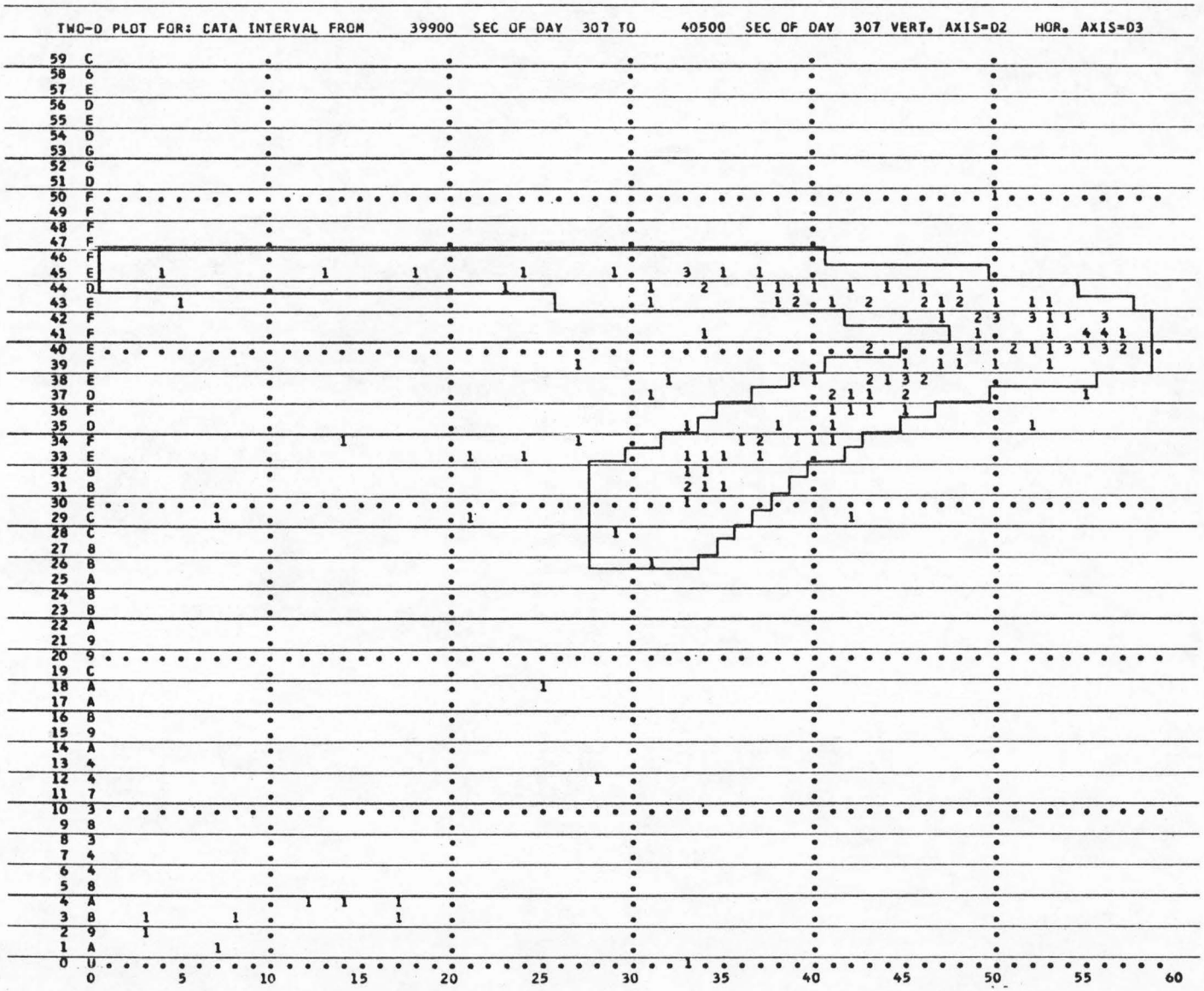
TWO-D PLOT FOR: DATA INTERVAL FROM 39900 SEC OF DAY 307 TO 40500 SEC OF DAY 307 VERT. AXIS=D2 HOR. AXIS=D3
0 5 10 15 20 25 30 35 40 45 50 55 60

of interest. The events which are not within the boundaries of these bands are either electrons, alphas, or in a few cases, protons which have deposited anomalously small amounts of energy in at least one of the detectors.

Using the relation between pulse-height response and incident energy displayed in Figures III-2 and III-3, these bands were divided into bins which correspond to different proton incident energy intervals. Specifically, the D1-D2-D3 pulse height "space" was divided into 37 proton incident energy bins by slicing the proton bands along calculated lines of constant incident energy (see Table III-1). At incident energies below ~3 MeV, protons stop in D1 and no 2-dimensional pulse-height information is available to cleanly separate protons from other charged particles. Since D1 is insensitive to electrons, the only threatening contaminants to the D1 proton analysis are low energy alpha particles. This alpha contamination can easily be estimated and can usually be neglected. Thus, below 3-MeV, the proton analysis consists of a one-to-one map between groups of D1 pulse-height channels and proton incident energy intervals.

The physics of the data reduction is contained in the proton pulse-height bins and the incident energy intervals assigned to them. Given such a set of bins, the rest of the analysis consists of deciding whether each pulse-height event lies in the proton band, and if so, in which bin. The proton differential flux dJ/dE can then be determined as follows:

TABLE III-1

Proton Pulse-Height Analysis Bins for the

ΔE-Range Telescope

Bin No.	Incident Energy		Type of Analysis
	E_{min}	E_{max}	
1	1.17	1.27	
2	1.27	1.37	
3	1.37	1.49	
4	1.49	1.61	
5	1.61	1.73	
6	1.73	1.87	
7	1.87	2.00	D1 Singles
8	2.00	2.14	$A\Omega = 1.13\ cm^2 sr \pm 6\%$
9	2.14	2.28	
10	2.28	2.42	
11	2.42	2.56	
12	2.56	2.70	
13	2.70	2.85	
14	2.85	2.99	
15	2.99	3.14	
16	3.14	3.30	D1 - D2
17	3.30	3.60	$A\Omega = 1.13\ cm^2 sr \pm 6\%$
18	3.60	4.00	

TABLE III-1 (Cont.)

Bin No.	Incident Energy		Type of Analysis
	E_{min}	E_{max}	
19	4.00	4.50	
20	4.50	5.00	
21	5.00	6.00	
22	6.00	7.00	D1 - D2 cont.
23	7.00	9.00	$A\Omega = 1.13\ cm^2 sr \pm 6\%$
24	9.00	15.00	
25	15.00	20.00	
26	20.00	30.00	
27	30.00	45.00	
28	20.00	25.00	
29	17.90	20.00	
30	20.00	25.00	
31	25.00	35.00	D2 - D3 -- no D4
32	35.00	45.00	$A\Omega = 1.59\ cm^2 sr \pm 6\%$
37	20.00	45.00	
33	45.00	70.00	
34	70.00	100.00	D2D3 with D4
35	100.00	150.00	$A\Omega = 1.2\ cm^2 sr \pm 6\%$
36	45.00	150.00	

$EMIN_i$, $EMAX_i$ = incident energy limits to pulse-height bin i

S_i = number of pulse-height events in bin i in given time interval

N = normalizer between pulse-height data and actual particle rates

$$= \frac{(D1\overline{D8} \text{ counting rate in counts/sec})}{(\text{total no. of } D1\overline{D8} \text{ pulse-height events})}$$

$A\Omega_i$ = geometrical factor in cm^2sr assigned to bin i

$\frac{dJ_i}{dE}$ = proton differential flux at bin i in $(cm^2 \text{sec sr MeV})^{-1}$ during time interval

$$= \frac{S_i \, N}{A\Omega_i \, (EMAX_i - EMIN_i)}$$

The normalizer N must be used instead of the actual accumulation time because there are frequently many more valid events than can be analyzed and readout.

B. Bulk Data Processing

The OGO-6 spacecraft has orbited the earth in a fully-operational state for 15 months (from 5 June 1969 to 29 August 1970). During this period, the satellite completed 6500 orbits, and Caltech's experiment F-20 accumulated approximately 2×10^{10} bits of digital cosmic ray data. With such a huge data set, it is virtually impossible to completely process all of the data in a reasonable amount of time. Consequently, a quick-processing scheme has been devised which allows

one to scan the data and select time periods of particular interest for more detailed analysis. The overall data processing plan for the Range Telescope is described in Figure III-6.

1. Tape Merging

The raw spacecraft data are received from Goddard Space Flight Center in the form of Attitude-Orbit Tapes, which describe the satellite location and orientation at 1-minute intervals, and Experimenter Tapes, which contain the decommutated data from Caltech's Experiment F-20. The first step in the data reduction process is to combine the cosmic ray data with the relevant attitude-orbit information and write the result on a single "merged" tape via a program named MERGE (see Figure III-6). These merged tapes are the basic input for all subsequent steps in the data analysis.

2. Polar Rate Averages

Since the work discussed in this thesis is concerned with the intensity of *interplanetary* cosmic rays, the data of interest can be accumulated only in the polar regions (see Section II-C). Although the question of particle access to the magnetosphere is a very complicated and still unsolved problem[24], there does exist a given region in Λ-MLT space at each pole where the flux is independent of spatial position and identical to the interplanetary flux in the vicinity of the earth[20]. This region is roughly defined by $|\Lambda| \geq 72^{\circ}$, even though the exact boundary location depends on MLT, particle rigidity, and on the configuration of the geomagnetic and interplanetary fields.

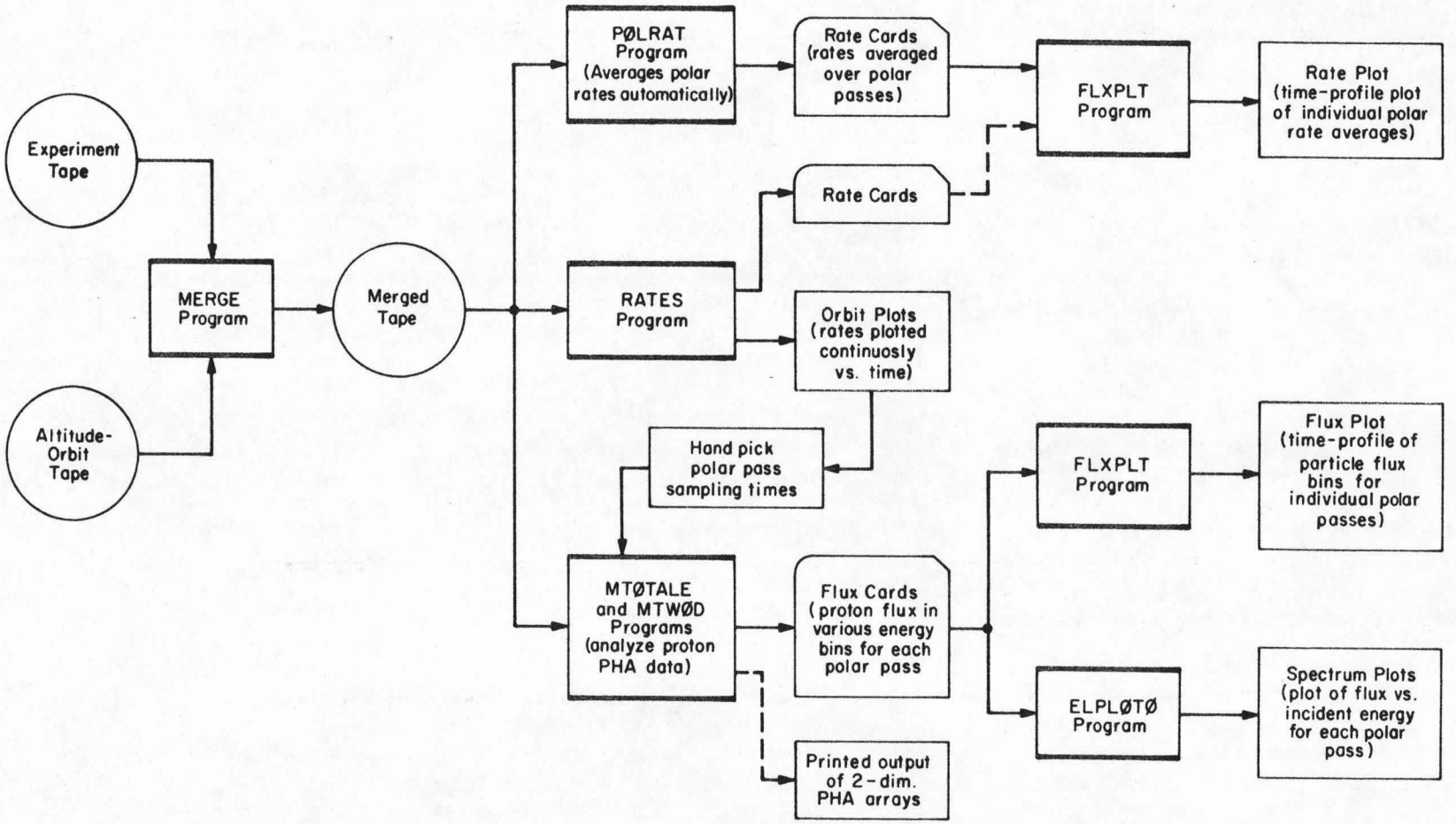

Figure III-6: Flow chart of the Range Telescope data processing.

The program PØLRAT is used to process the merged tapes and sample the cosmic ray data automatically whenever $|\Lambda| > 72^{o}$. The appropriate range telescope coincidence and single detector counting rates are averaged over these polar "cuts" and the results are punched on cards. A routine called FLXPLT is then used to plot these individual polar rate averages vs. time. Figure III-7 is an example of a typical computer-generated "rate plot" which enables one to decide whether the data should be subjected to more intensive (and more expensive) analysis.

3. Orbit Plots

In order to analyze the data in a given time period in more detail, the proton polar access regions must be defined more precisely. A program named RATES is used to generate continuous plots of the key detector counting rates as a function of time for each satellite orbit. Such an "orbit plot" (see Figure III-8) makes the proton polar access regions obvious and allows one to easily hand-pick time "cuts" for further analysis. The dashed lines on Figure III-8 indicate the proton polar cuts chosen for this particular orbit.

The orbit plot shown in Figure III-8 is in fact a streamlined version which includes only the most important Range Telescope coincidence rates. The write-up for the RATES program[17] describes how more complete orbit plots including some of the pulse-height data and all of the 20 experiment counting rates can be generated.

Figure III-7

A computer-generated "rate plot" produced by program FLXPLT. The $D1\overline{D8}$ and $D2D3\overline{D8}$ rates (labeled D1ND8 and D2D3ND8), averaged over individual polar cuts, are plotted vs. time over an 11-day interval.

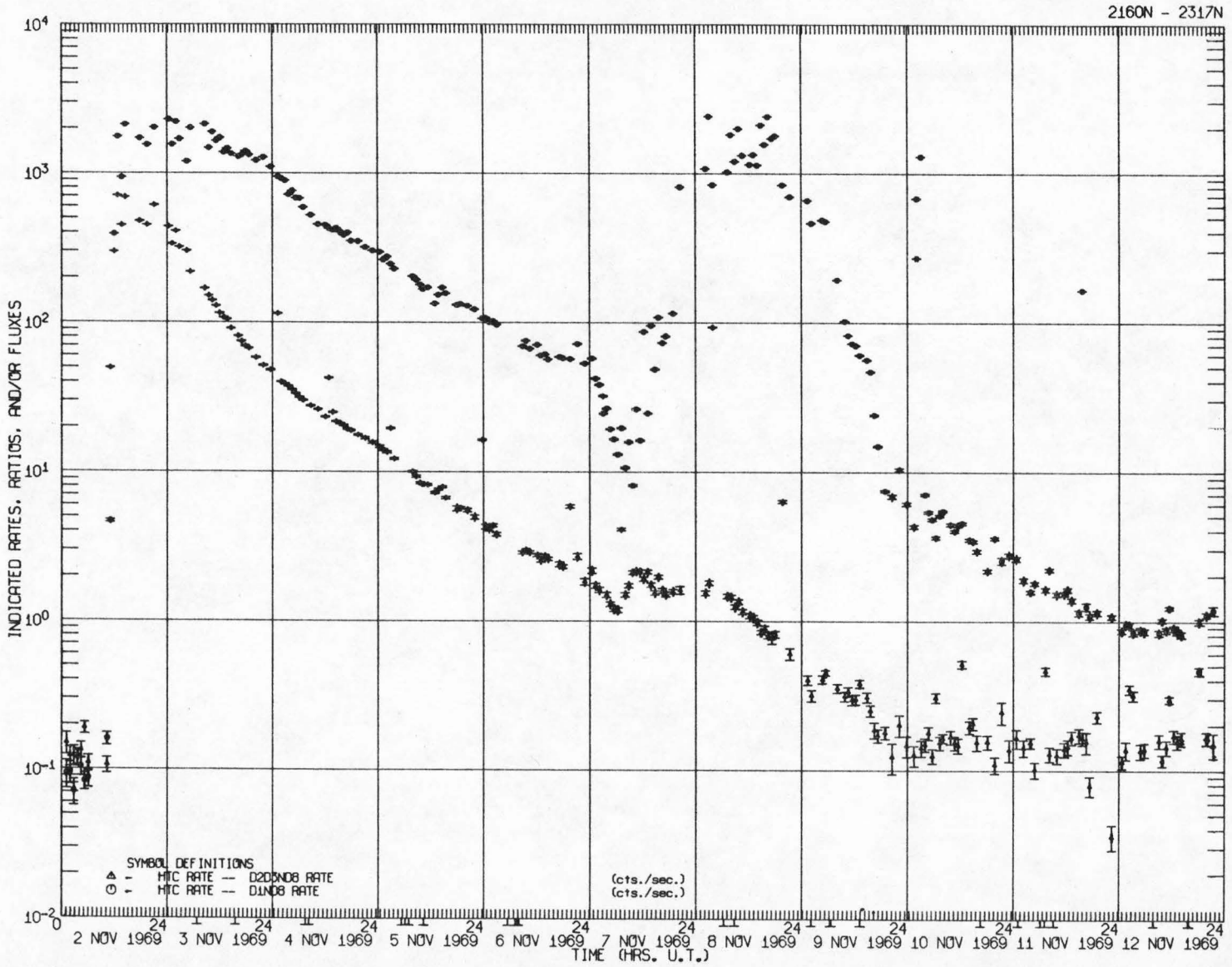
2160N - 2317N
INDICATED RATES, RATIOS, AND/OR FLUXES
10^4
10^3
10^2
10^1
10^0
10^{-1}
10^{-2}
SYMBOL DEFINITIONS
△ - HTC RATE -- D2D3ND8 RATE
⊙ - HTC RATE -- D1ND8 RATE
(cts./sec.)
(cts./sec.)
0
24
2 NOV 1969
3 NOV 1969
4 NOV 1969
5 NOV 1969
6 NOV 1969
7 NOV 1969
8 NOV 1969
9 NOV 1969
10 NOV 1969
11 NOV 1969
12 NOV 1969
TIME (HRS. U.T.)

Figure III-8

A computer-generated "orbit plot" produced by the program RATES. The D1$\overline{D8}$, D2$\overline{D8}$, and D2D3$\overline{D8}$ coincidence rates (labeled D18, D28, and D238) are plotted continuously vs. time for one full spacecraft orbit. Magnetic Local Time and Invariant Latitude are also included. The proton access regions are clearly evident, and the hand-picked cuts have been marked with dashed lines. Each tickmark along the Y-axis represents one decade in counting rate. Changes in the D2$\overline{D8}$ counting rate during the proton polar cuts are due to electrons.

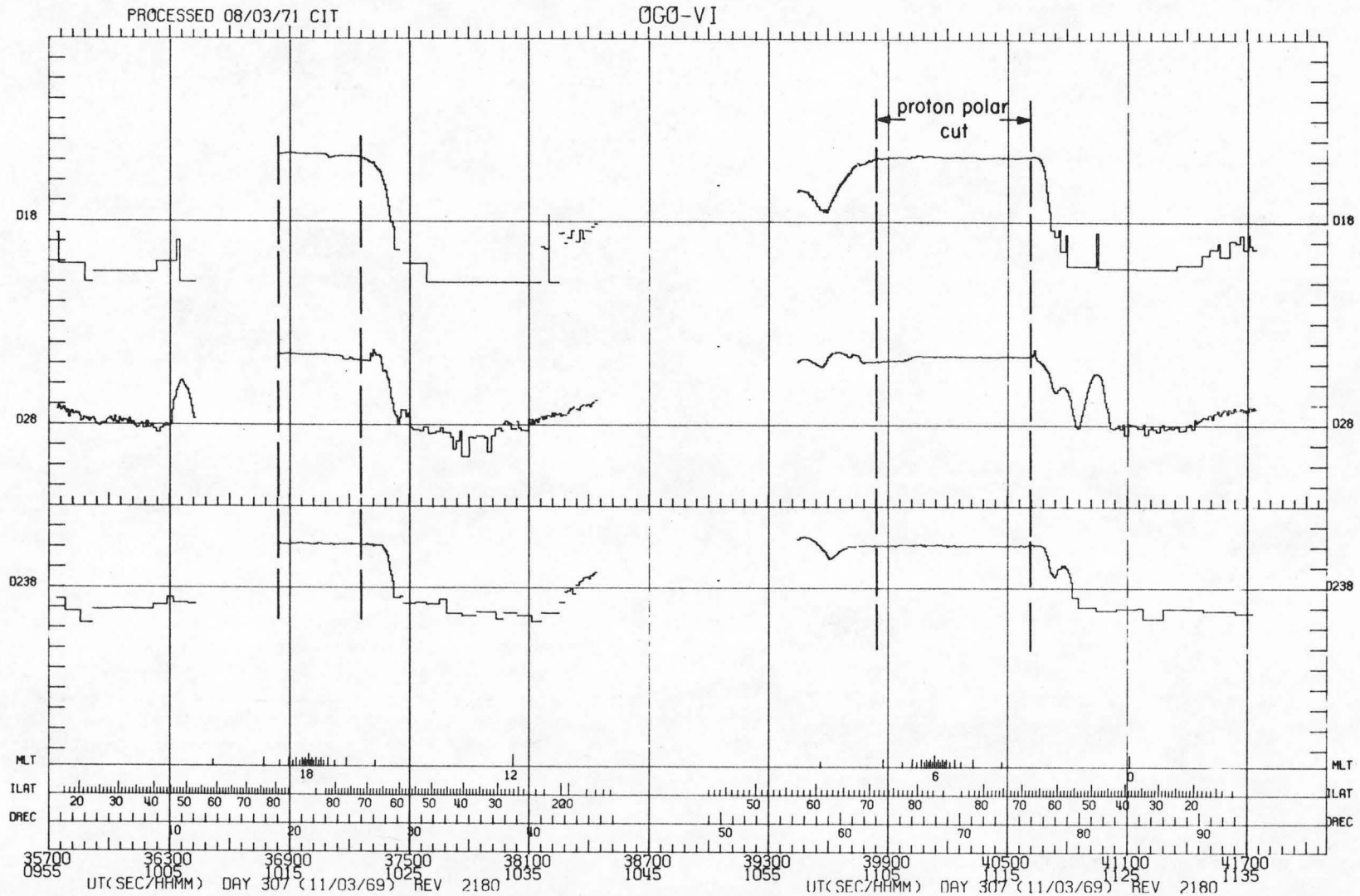
PROCESSED 08/03/71 CIT
0GØ-VI
proton polar cut
D18
D28
D238
MLT
ILAT
DREC
35700
0955
36300
1005
36900
1015
37500
1025
38100
1035
38700
1045
39300
1055
39900
1105
40500
1115
41100
1125
41700
1135
UT(SEC/HHMM) DAY 307 (11/03/69) REV 2180
UT(SEC/HHMM) DAY 307 (11/03/69) REV 2180

4. Calculation of Proton Flux

The time cuts chosen from the orbit plots are used as inputs to the programs MTØTALE and/or MTWØD which process the pulse-height data on the merged tapes during the time intervals specified. (See Figure III-6.) Printed output of the 2-dimensional pulse-height analyzer arrays can be produced (Figures III-4 and III-5 are examples). The proton differential fluxes in each of the 37 bins are calculated and punched on cards. These cards are in turn used as an input to FLXPLT, which produces plots of the flux time-profiles analogous to the rate profiles of Figure III-7. Alternatively, the flux bins can be plotted together for each polar cut to form an instantaneous proton differential energy spectrum as in Figure III-9.

This completes the description of how the instrument and spacecraft function, and in particular how the Range Telescope responds to the low energy cosmic ray protons which are the topic of this dissertation. A brief account has been given of the manner in which the tremendous bulk of satellite data is scanned, sampled, and converted to useful information. The information desired is of course the interplanetary proton flux as a function of energy and time.

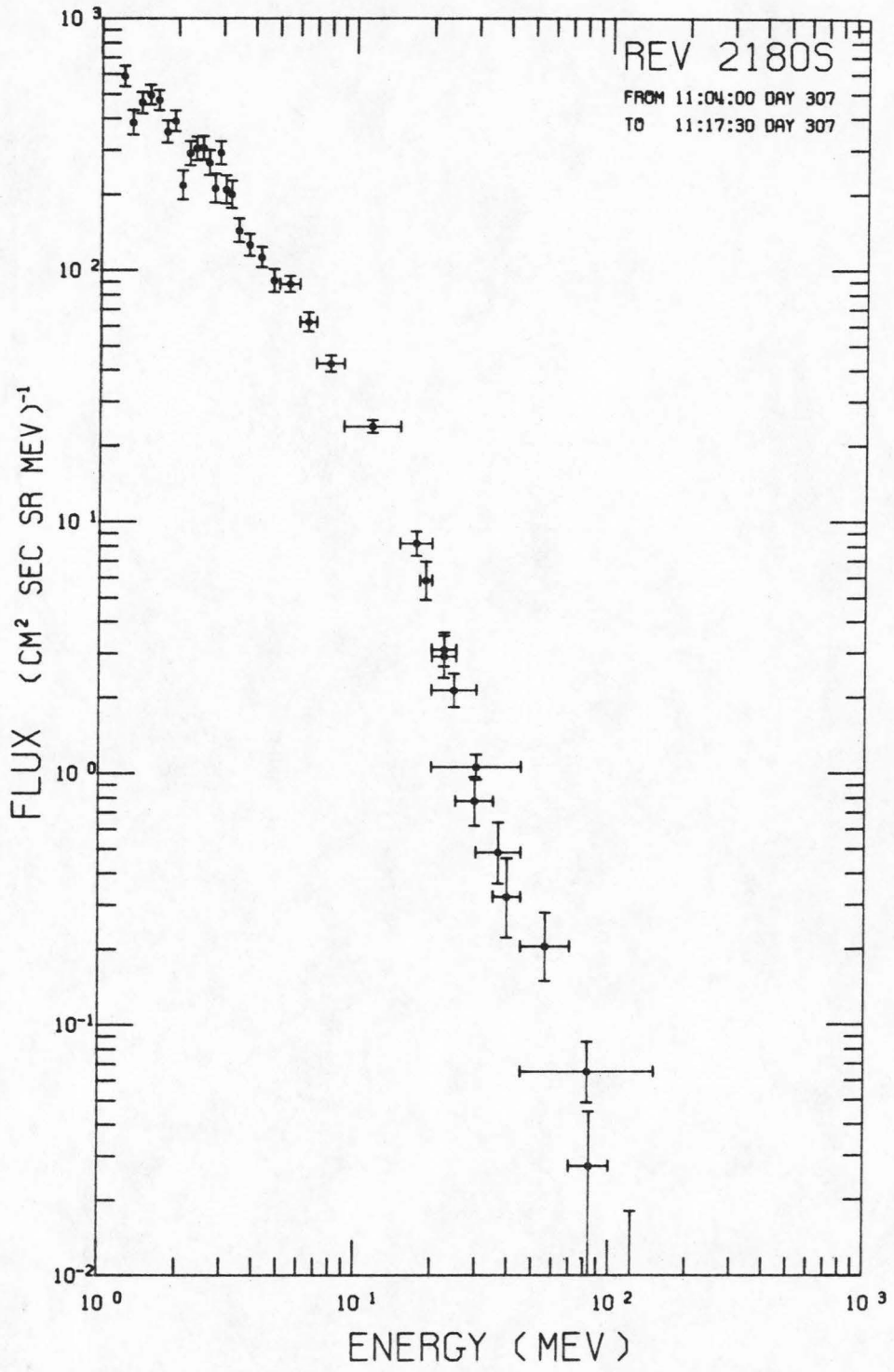

Figure III-9: A computer-generated plot of the flux calculated for each of the 37 pulse-height bins vs. incident energy for a single polar pass. The plot thus represents an instantaneous sample of the proton differential energy spectrum.

IV. OBSERVATIONS

Solar cosmic ray phenomena as observed near the earth can be divided into the following four distinct types[25]:

a) Flare-associated events -- associated with optical flares, x-ray and microwave emission. Electrons and nucleons observed at the earth generally display a rapid (<2 day) intensity increase followed by a slower decay phase.

b) Recurrent events -- particle increases which sometimes appear on the next rotation* after a flare-associated event. These events display roughly the same time history as the original flare and apparently originate from the same active region.

c) Energetic particles associated with an active center -- increases which display no velocity dispersion and are not associated with solar flare activity. They are thought to be particles emitted continuously from an active region but confined to a given region of interplanetary space. The time-profile of the event, which persists from 3 - 14 days, is thus produced by the "co-rotation" of this region past the earth. These events display steep proton energy spectra and are often anti-correlated with the MeV electron intensity.

d) Energetic storm particle events -- large intensity increases of low energy protons and electrons associated with (and believed to be accelerated by) strong interplanetary shock waves.

---

*The surface of the sun revolves at a rate which depends on solar latitude (the period is ~27 days at the equator).

This dissertation is concerned only with flare-associated events, and specifically with the means by which these flare particles, which are assumed to be injected impulsively on the sun at the location of the optical flare, propagate through interplanetary space to the earth. The details of the actual flare event on the solar surface are of interest here only when they affect the subsequent particle propagation and the intensity observations at the earth. This section discusses the method by which flare-associated events are identified, and summarizes the OGO-6 proton intensity observations of four such events which are discussed in Section V.

A. Event Identification

The typical solar flare proton behavior in the vicinity of the earth can be described as a rapid rise in intensity, followed by a smooth turnover and an approximately exponential decay phase with $\tau_{dec} \simeq 5 - 30$ hours[25,26]. However, such "typical" flare time-profiles are rarely observed, and in many cases it is difficult to separate flare events from the other three types of solar phenomena. In order to yield useful clues about the nature of particle propagation in interplanetary space, the following information must be determined about an individual flare event:

a) The event identification must be unambiguous -- that is, it must be possible to associate the intensity observations at earth on a one-to-one basis with a *single* optical flare event on the sun. The particle injection time ($\pm$ a few hours) and the point of injection on the sun (in solar latitude and longitude) can easily be determined once

the optical counterpart of the cosmic ray event has been identified. Multiple flare events, which occur frequently, are deemed unsuitable for more detailed analysis.

b) It must be determined that no co-rotating features (i.e., recurrent events or active center events) or interplanetary magnetic field boundaries have rotated by the earth during the flare observation period. Such occurrences complicate the situation immensely and make detailed analysis very difficult.

c) The average value of the solar wind velocity in the vicinity of the earth must be determined. This is a parameter which affects the particle propagation and thus is needed for complete analysis of the event.

The method by which particle events can be accurately identified is provided by the solar geophysical data published by ESSA (now NOAA)[27,28]. The emission of Type IV radio bursts and hard x-rays are generally accepted as indicators of solar particle acceleration and injection[26, 29]. Although an intense optical flare is not necessarily a good candidate for a particle event, Type IV radio and/or x-ray emission simultaneous with an optical flare of reasonable size (importance ≥ 1) preceding the particle increase by only a few hours is taken to be a good event identification. Co-rotating features, magnetic field boundary crossings, and shock wave events can usually be identified and eliminated because they are often associated with disturbances of the geomagnetic field (sudden commencements and sudden impulses) and with sudden large changes in the solar wind plasma velocity.

B. OGO-6 Solar Flare Observations

For the period from 7 June 1969 to 11 February 1970, the Caltech Solar and Galactic Cosmic Ray Experiment aboard OGO-6 operated normally and recorded 250 days of nearly uninterrupted cosmic ray data. On February 11, 1970, the C4 ground command was given because of a noisy D1 detector[30], making subsequent Range Telescope data nearly useless for the purposes of this detailed investigation. These 9 months of data, which were carefully scanned for solar flare events, are summarized in Appendix A. Table IV-1 lists the 12 flare-associated events of significant magnitude that occurred during this period. Of these 12, only 7 could be clearly associated with an optical flare, and 3 of these were either multiple events or were complicated by magnetic disturbances.

Figure IV-1 shows the intensity vs. time profile at several energies for each of the four remaining events. Each intensity point represents an individual polar pass analyzed in the manner described in Section III. The ESSA data for optical flares, x-ray flares, Type-IV radio emission, sudden commencements, sudden impulses, and solar wind velocity have been included. Table IV-2 summarizes the optical identification which has been assumed for each of these events.

The 7 June 69 event suffers from some ambiguity as to optical flare identification, although this produces only an uncertainty as to the exact injection time. The precursor to this event, which is quite evident in Figure IV-1-a, may be due to the earlier flare at 0018 - 0130 UT on the same day. The decay phase of this event has been studied in some detail elsewhere[17,31].

TABLE IV-1

Flare-Associated Particle Events Observed by

OGO-6 Between 7 June 1969 and 11 February 1970

Date	Approximate UT of Particle Increase ± 4 hours	Optical Flare Identification	Comment
7 June 69	1700	yes	OK
25 Sept	1100	yes	Multiple Flare
27 Sept	2200	yes	Magnetic Storm
14 Oct	0000 - 0800	?	Possible Multiple Flare
2 Nov	1000	yes	OK - Magnetic Storm beginning on Nov. 7
24 Nov	1200	yes	Multiple Flare
18 Dec	1800	no	No Identification
19 Dec	2400	no	No Identification
30 Dec	2400	yes	OK
28 Jan 70	1600	?	Multiple Flares
29 Jan	1200	no	
31 Jan	2000	yes	OK

Figure IV-1

Time histories of four selected solar flare particle events.

The following quantities are plotted vs. universal time:

Polar averages of the proton differential flux as observed by experiment F-20 aboard OGO-6 for various incident energy bins.

Optical Flares of significant magnitude -- the importance is included.

X-ray Flares -- observations from Explorers 33 and 35 at 2 - 12Å.

Type-IV Radio Emission -- reported as "Solar Radio Spectral Observations" by ESSA.

Sudden Commencements and Sudden Impulses -- disturbances of the geomagnetic field often related to fluctuating conditions in interplanetary space.

Solar Wind Velocity -- near-earth observations on Vela 3 and 5, and less relevant observations from Pioneer VI and VII. The Pioneer spacecraft are typically separated from the earth by ~100° in heliocentric longitude.

With the exception of the proton intensity, all of the data were taken from the ESSA Bulletins[27], and further information can be found in the descriptive text provided by ESSA[28].

Graph a -- The 7 June 1969 Event

Graph b -- The 2 November 1969 Event

Graph c -- The 30 December 1969 Event

Graph d -- The 31 January 1970 Event

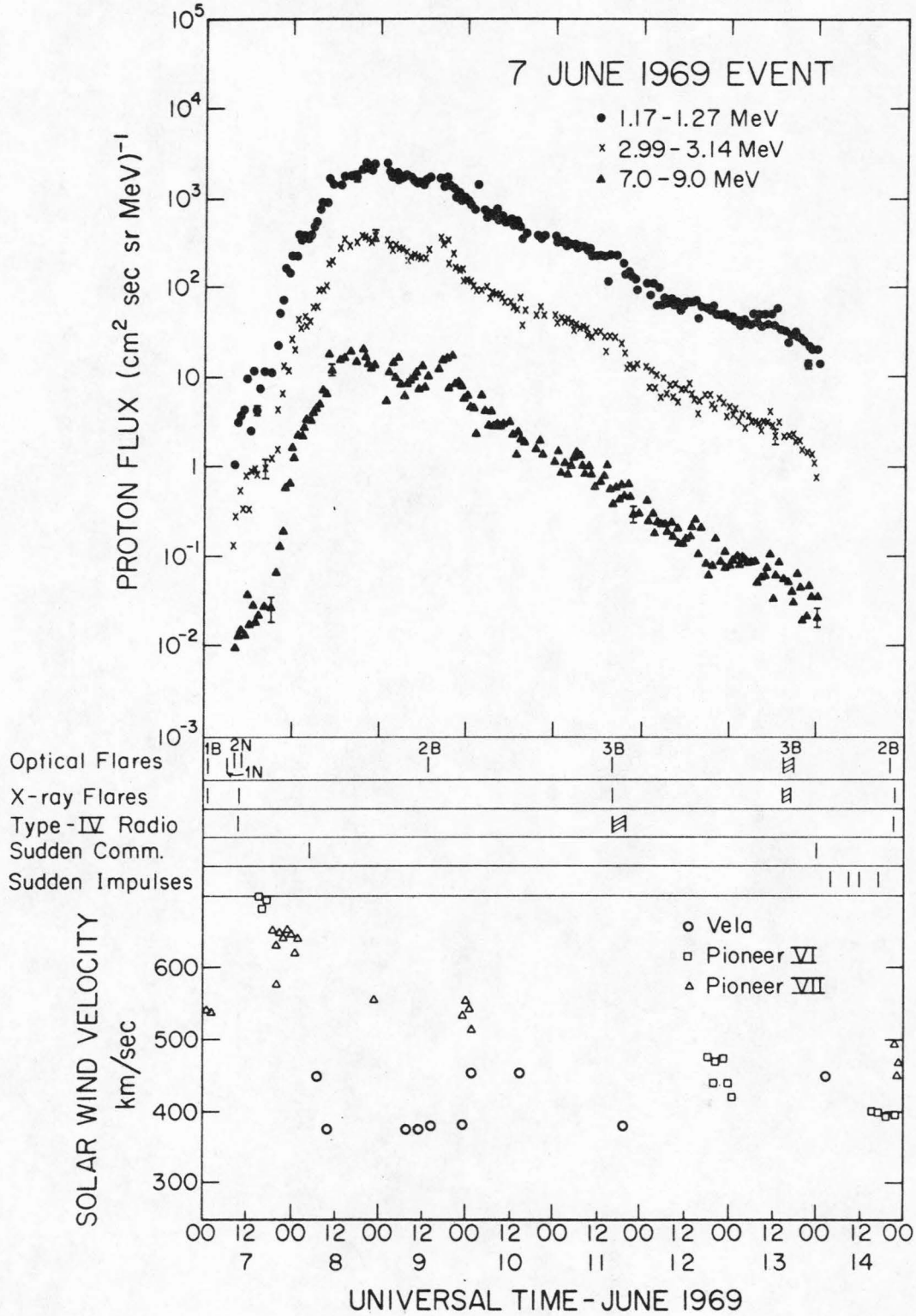
7 JUNE 1969 EVENT
• 1.17 - 1.27 MeV
× 2.99 - 3.14 MeV
▲ 7.0 - 9.0 MeV
PROTON FLUX (cm² sec sr MeV)⁻¹
10⁵
10⁴
10³
10²
10
1
10⁻¹
10⁻²
10⁻³
Optical Flares
X-ray Flares
Type - IV Radio
Sudden Comm.
Sudden Impulses
1B
2N
1N
2B
3B
3B
2B
SOLAR WIND VELOCITY km/sec
600
500
400
300
o Vela
□ Pioneer VI
△ Pioneer VII
00 12 00 12 00 12 00 12 00 12 00 12 00 12 00 12 00
7 8 9 10 11 12 13 14
UNIVERSAL TIME - JUNE 1969

Figure IV-1-a

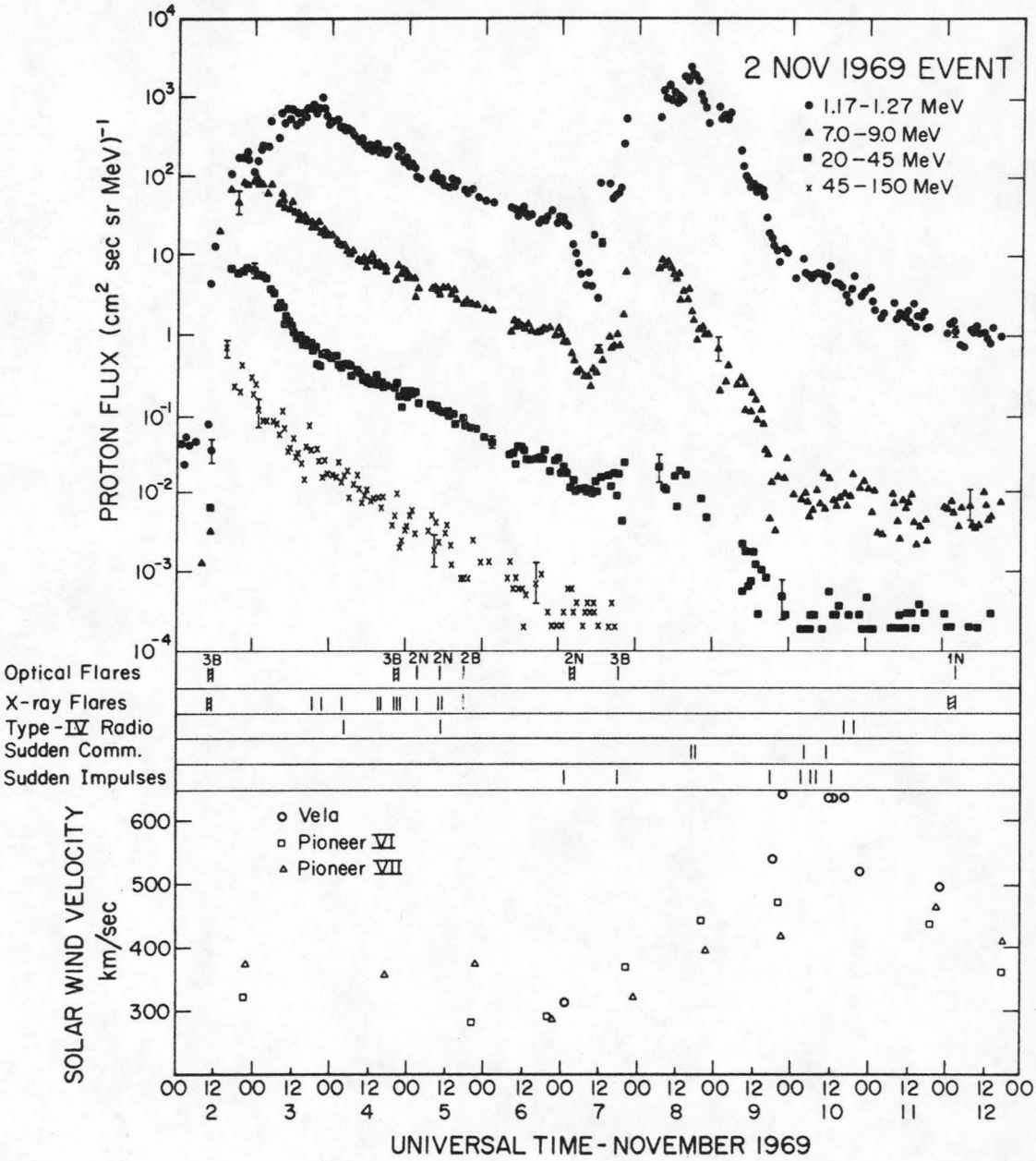
2 NOV 1969 EVENT
1.17-1.27 MeV
7.0-9.0 MeV
20-45 MeV
45-150 MeV
PROTON FLUX (cm² sec sr MeV)⁻¹
Optical Flares
X-ray Flares
Type-IV Radio
Sudden Comm.
Sudden Impulses
SOLAR WIND VELOCITY km/sec
Vela
Pioneer VI
Pioneer VII
UNIVERSAL TIME - NOVEMBER 1969

Figure IV-1-b

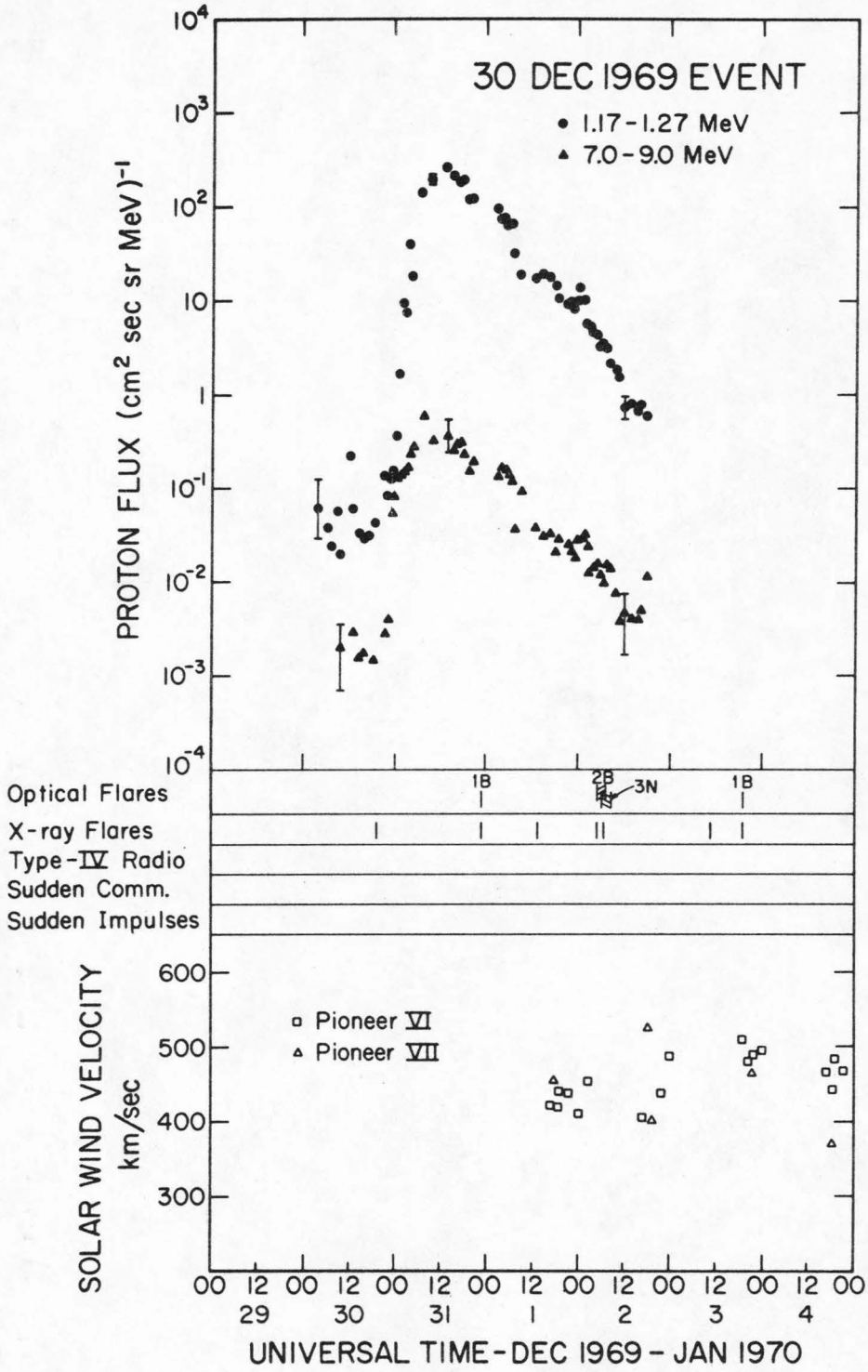
30 DEC 1969 EVENT
• 1.17 - 1.27 MeV
▲ 7.0 - 9.0 MeV
PROTON FLUX (cm² sec sr MeV)⁻¹
10⁴
10³
10²
10
1
10⁻¹
10⁻²
10⁻³
10⁻⁴
Optical Flares
X-ray Flares
Type-IV Radio
Sudden Comm.
Sudden Impulses
1B
2B
3N
1B
SOLAR WIND VELOCITY km/sec
600
500
400
300
□ Pioneer VI
△ Pioneer VII
00 12 00 12 00 12 00 12 00 12 00 12 00 12 00 12 00
29 30 31 1 2 3 4
UNIVERSAL TIME - DEC 1969 - JAN 1970

Figure IV-1-c

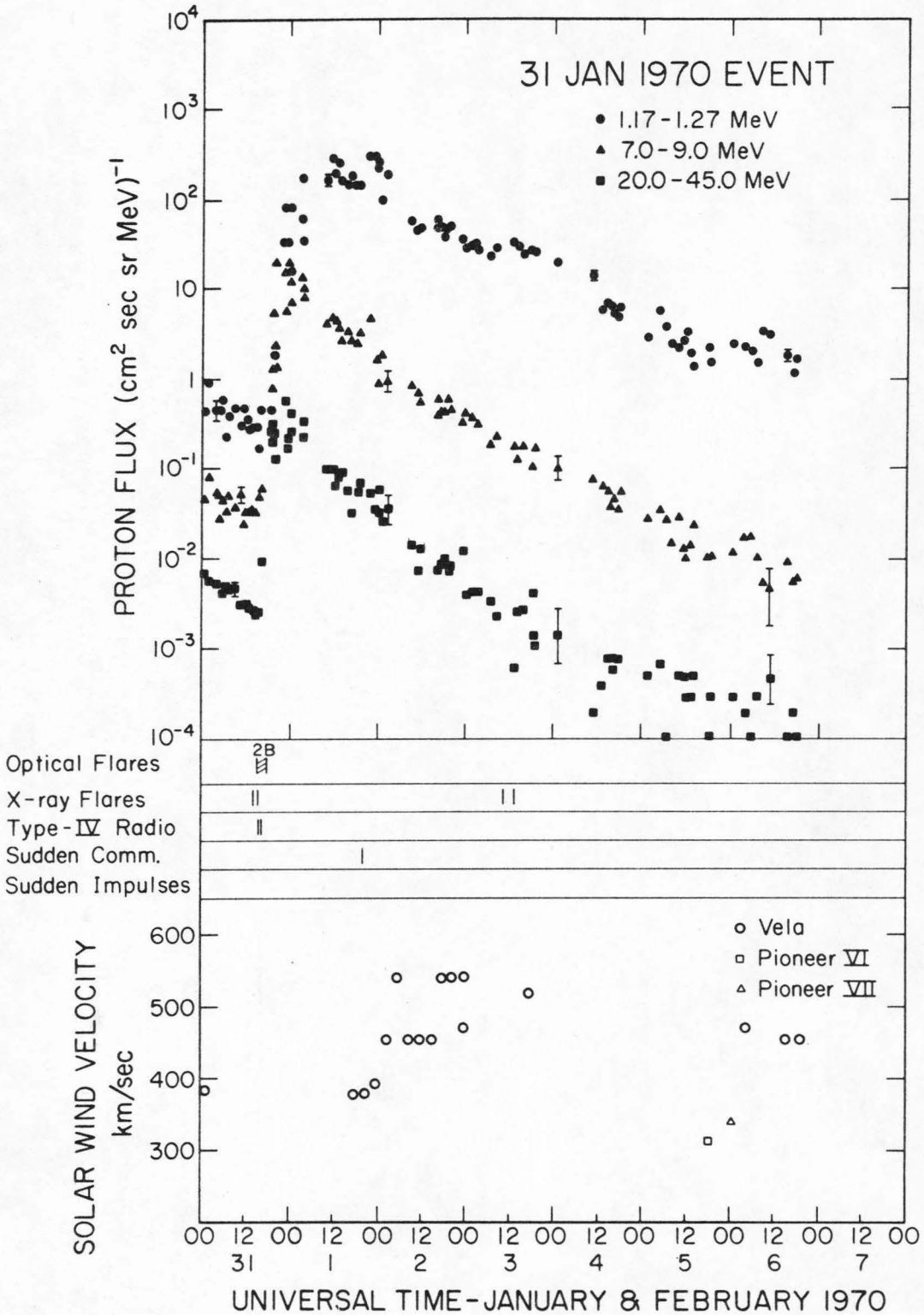
31 JAN 1970 EVENT
1.17-1.27 MeV
7.0-9.0 MeV
20.0-45.0 MeV
PROTON FLUX (cm² sec sr MeV)⁻¹
Optical Flares
X-ray Flares
Type-IV Radio
Sudden Comm.
Sudden Impulses
2B
SOLAR WIND VELOCITY km/sec
Vela
Pioneer VI
Pioneer VII
UNIVERSAL TIME-JANUARY & FEBRUARY 1970

Figure IV-1-d

TABLE IV-2

Summary of the Flare Events Selected for Analysis

Date	Optical Flare*			UT of X-ray Flares*	UT of Type-IV Radio*	Assumed UT of Particle Injection	Assumed Ave. Solar Wind Velocity†† km/sec
	Importance	Solar Coordinates	UT				
7 June 69	2N	E45-S15	0630-0730 0806-0820 0930-1100	? -1000	0953-0959	0800 ± 0200	400 ± 50
2 Nov 69	3B	W90-N15	0939-1130	0945-1059	---	1000 ± 0100	325 ± 70
30 Dec 69	?†	W85-S15†	1900-2000†	1903-1933	---	1930 ± 0030	450 ± 70
31 Jan 70	2B	W62-S22	1508-1535	1507-1544	1536-1614	1530 ± 0100	400 ± 100

*from the ESSA Bulletins (27)

†Since the optical flare data did not exist in the ESSA Bulletins, the optical identification was made directly by the author from solar photographs taken by Harold Zirin of Caltech.

††Although the errors listed here are reasonable estimates of the uncertainty in the solar wind velocity, these errors were not used in any of the subsequent analysis.

The 2 November 1969 event was one of the largest during Solar Cycle 20[32], and has been described in a special ESSA report[33]. The second particle increase beginning on November 7 is probably not a flare-associated event at all, since it is accompanied by a magnetic storm and by changes in the solar wind velocity.

Although the 30 December 1969 event has the symmetric rise and decay that frequently characterize a co-rotating feature, the geomagnetic disturbances and solar wind fluctuations which usually indicate a non-flare event are missing. An x-ray flare occurred at 1903 - 1933 UT, about 2 hours before the particle increase at earth, but there was no flare patrol at this time and thus no optical flare was reported. However, a search through the solar photographs taken by Professor Harold Zirin of Caltech yielded a positive optical event identification. Zirin's solar telescope had recorded a west limb flare event, complete with a prominence, between ~1900 and ~2000 UT on December 30, 1969.

The 31 January 1970 event is the last in a series of 3 flare events in a 4-day period, but the intensity-time profile is unaffected by the previous events (see Appendix A). The D1 detector noise problem, mentioned previously, was present during this event and affected the data coverage to some extent.

The time evolution of the differential proton energy spectrum during the decay phase is shown in Figure IV-2 for each of the four events. Note that, with the exception of the 30 December event, the spectra decay without any significant change in "shape" over a period of at least 48 hours. The change in slope at ~3 MeV evident in the

Figure IV-2

Samples of the proton differential energy spectrum during the decay phase of four selected solar flare particle events. The observations were made by Caltech's Solar and Galactic Cosmic Ray Experiment aboard OGO-6 and thus represent the near-earth particle flux. In each case, two spectra separated in time are included to demonstrate the time evolution of the proton flux. With the exception of the 30 Dec 1969 event, the spectra decay without significant change in shape over a 2-day period.

Graph a -- The 7 June 1969 Event

Graph b -- The 2 November 1969 Event

Graph c -- The 30 December 1969 Event

Graph d -- The 31 January 1970 Event

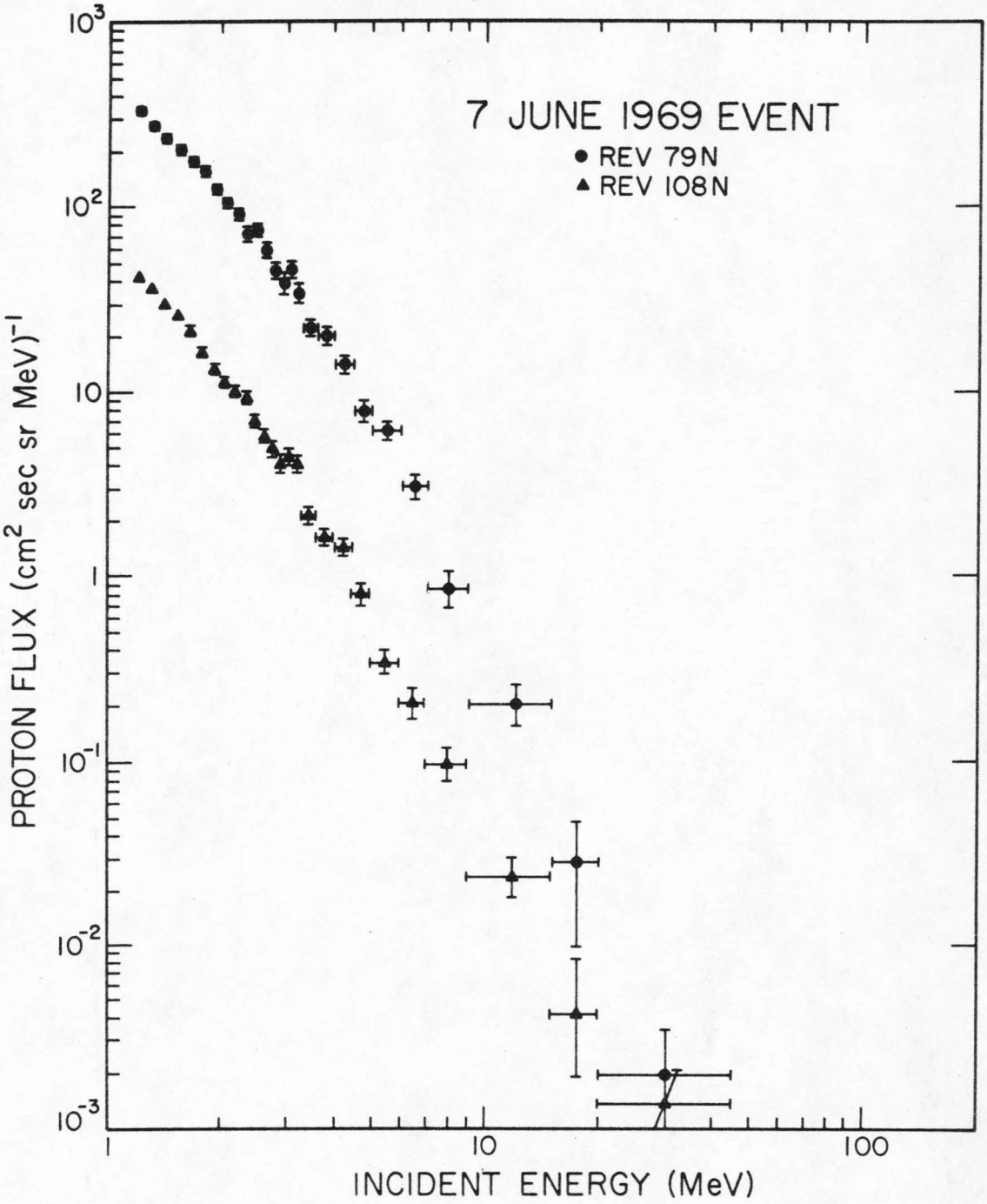
7 JUNE 1969 EVENT
● REV 79N
▲ REV 108N
PROTON FLUX (cm² sec sr MeV)⁻¹
INCIDENT ENERGY (MeV)
10³
10²
10
1
10⁻¹
10⁻²
10⁻³
1
10
100

Figure IV-2-a

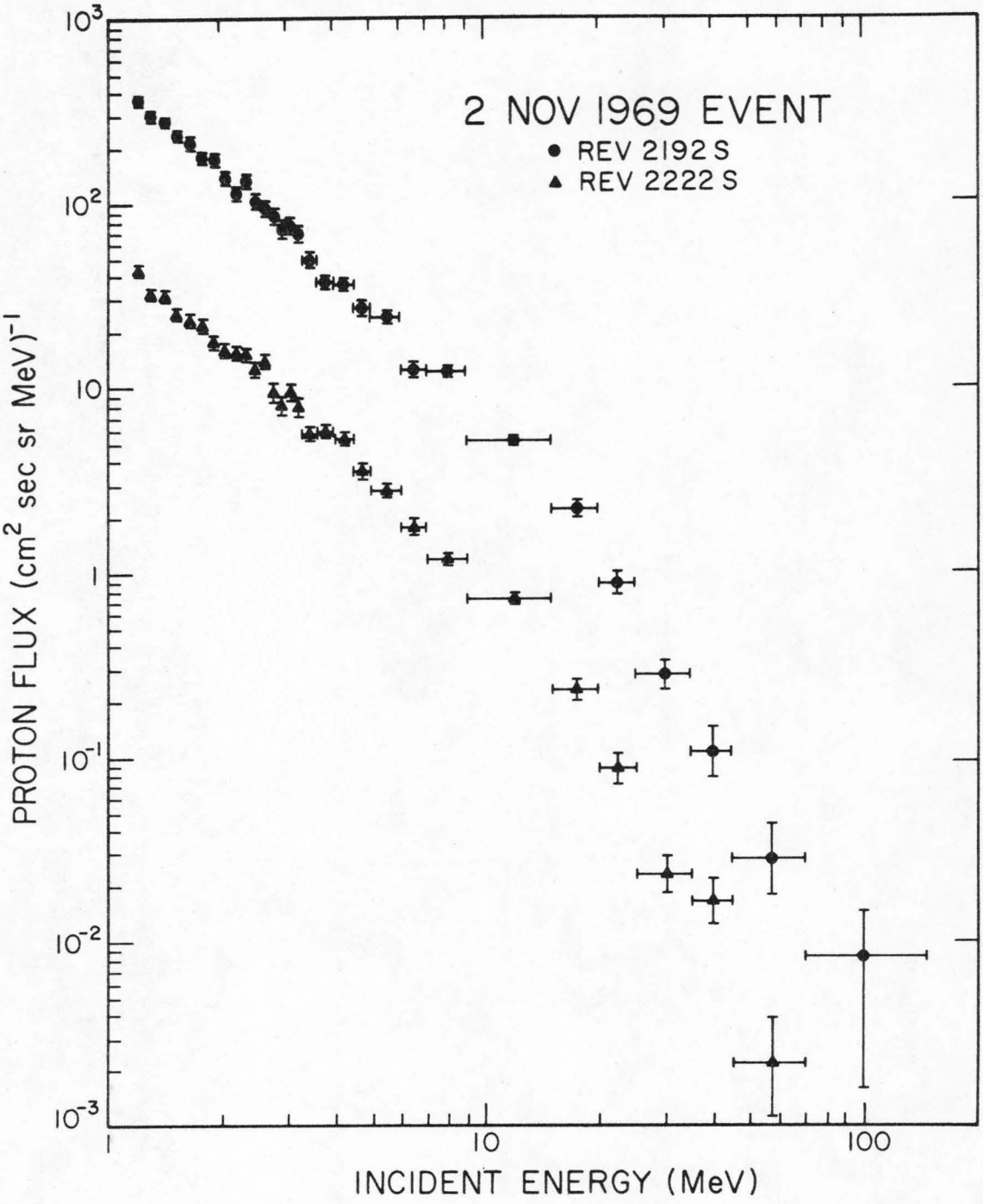
2 NOV 1969 EVENT
REV 2192 S
REV 2222 S
PROTON FLUX (cm² sec sr MeV)⁻¹
INCIDENT ENERGY (MeV)
10³
10²
10
1
10⁻¹
10⁻²
10⁻³
1
10
100

Figure IV-2-b

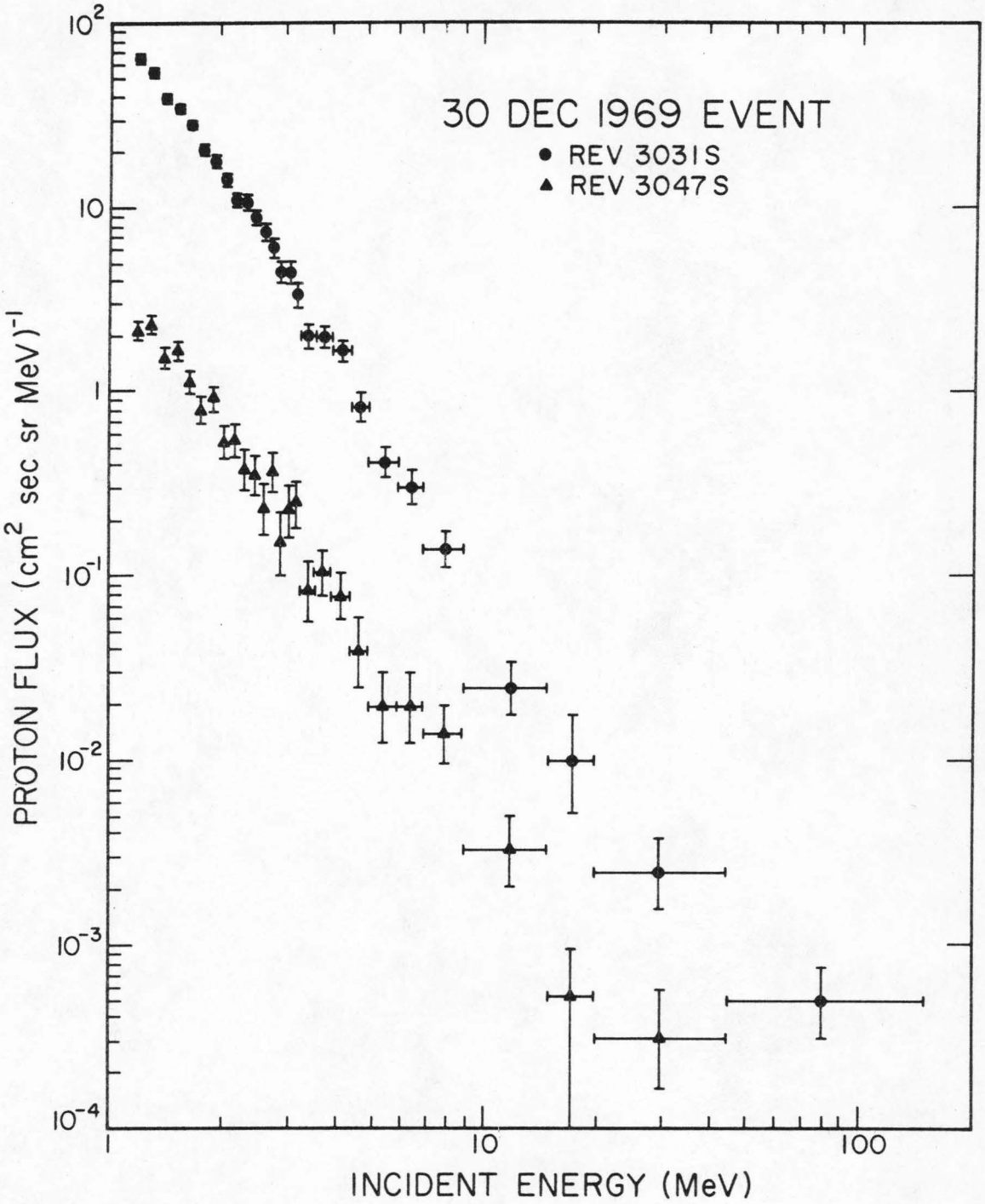
30 DEC 1969 EVENT
● REV 3031S
▲ REV 3047S
PROTON FLUX (cm² sec sr MeV)⁻¹
INCIDENT ENERGY (MeV)
10²
10
1
10⁻¹
10⁻²
10⁻³
10⁻⁴
1
10
100

Figure IV-2-c

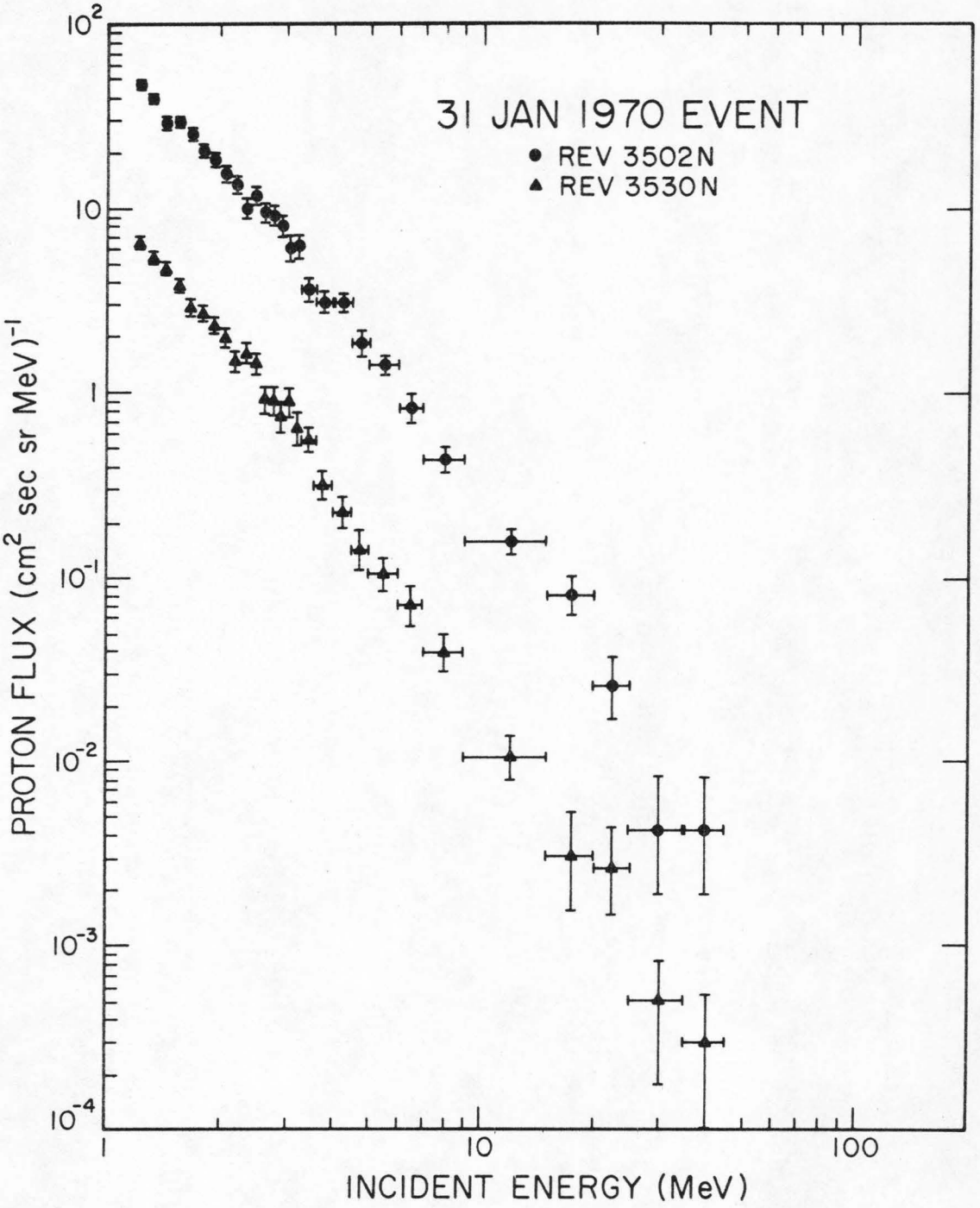
31 JAN 1970 EVENT
REV 3502N
REV 3530N
PROTON FLUX (cm² sec sr MeV)⁻¹
INCIDENT ENERGY (MeV)
10²
10
1
10⁻¹
10⁻²
10⁻³
10⁻⁴
1
10
100

Figure IV-2-d

7 June 69 and 31 January 70 spectra are of particular interest because they allow one to determine whether any energy-change processes are occurring as part of the solar particle transport[31].

In summary, the analysis of about 9 months of OGO-6 cosmic ray data has yielded four solar flare proton events which are uncomplicated and which can be easily associated with an optical flare on the sun. The relevant information about these events consists of the time and position of particle injection at the sun, the interplanetary conditions at the time (such as the solar wind velocity), and the proton intensity vs. time profile for various incident energy bins as observed at earth. This information, which is the result of standard analysis procedures, holds some clues to the physics of the propagation of solar flare particles and to the nature of interplanetary space. These clues are the subject of the next section.

V. DISCUSSION

A. Introduction

In almost every case, attempts to explain the propagation of energetic solar flare particles through interplanetary space have been based on the pioneering work of E. N. Parker. Parker correctly described the general features of interplanetary space[34, 35] (i.e., a spiral magnetic field imbedded in an outward-flowing solar wind), and also explained the propagation of energetic particles through this medium in terms of the Fokker-Planck equation[4]. The equation can be written:

$$\frac{\partial n}{\partial t} + \vec{\nabla} \cdot \left\{ \vec{V} \left[n - \frac{1}{3} \frac{\partial}{\partial T} (\alpha T n) \right] - \underline{\underline{\kappa}} \cdot \vec{\nabla} n \right\} = - \frac{V}{3} \frac{\partial}{\partial r} \frac{\partial}{\partial T} (\alpha T n) \tag{5-1}$$

where n is the particle density, r the radial distance from the sun, $\vec{V}$ the solar wind velocity, T the particle kinetic energy, $\alpha(T) = (T + 2m_o c^2)/(T + m_o c^2)$, and $\underline{\underline{\kappa}}$ the diffusion tensor describing the random walk of the particles in the interplanetary plasma. This equation, which involves the particle density in a stationary frame of reference, includes the effects of particle diffusion, outward convection by the solar wind, and adiabatic cooling due to the solar wind expansion.

The Fokker-Planck equation has won general acceptance, and many solutions to it have been produced both for the steady-state case (to describe galactic particle propagation into the solar system as well

as steady-state solar emission), and for the time-dependent case[3, 10,11,12,13,14,36,37] (to describe solar flare cosmic ray injection and transport). Because the equation is difficult to solve, every successful analytic solution has associated with it a set of simplifying assumptions and boundary conditions which make the equation soluble but at the same time critically affect the behavior of the solution. Current discussions about the theory of solar flare particle events are thus more often concerned with the validity of the assumptions used to produce a given solution, than with the physics contained in the differential equation itself.

The following is a partial list of unsolved problems concerning the theory of solar flare particle events:

1) The Diffusion Tensor -- Although it is generally assumed that $\underline{\underline{\kappa}}$ can be separated into components $\kappa_{\parallel}$ and $\kappa_{\perp}$ parallel and perpendicular to the spiral interplanetary field[1], very little is known about the dependence of $\underline{\underline{\kappa}}$ on distance from the sun and on particle energy, especially at low energies. The most widely-used estimates of the dependence of κ on particle energy T and radial distance r have been based on measurements of the power spectrum of the fluctuations in the interplanetary field between 1 and 1.5 AU[1,8,9,38,39].

2) Azimuthal Propagation -- Spacecraft observations of a longitudinal gradient in the solar flare particle density persisting for many days have been reported[15,26,40,41] and indicate that, in at least some cases, very little perpendicular particle

diffusion occurs in interplanetary space. The idea has thus developed that $\kappa_\perp << \kappa_\parallel$ and that flare particles are distributed in solar longitude early in the event by some transport process occurring near the sun, rather than by diffusion "across" the field lines in interplanetary space[42]. However, this idea has not been developed to the point where it can explain the observed dependence of intensity rise time on parent flare position[10].

3) An Outer Boundary to the Diffusing Region -- In order to explain the often-observed exponential decay of flare events, a perfectly-absorbing outer boundary to the diffusing region at r = L has been introduced in some models[3,10,12]. The position and even the existence of this boundary remain points of controversy[13].

4) Scatter-free Propagation Near the Sun -- The general question of the boundary conditions in existence near the sun is still unanswered. In particular, it has been suggested[43] that the rapid arrival and subsequent slow decay of the particles observed at earth can be explained in terms of a "scatter-free" region extending from the sun outward to some distance r < 1 AU.

5) The Energy-Change Process -- Recently the first experimental evidence for the adiabatic cooling effect (predicted by the Fokker-Planck equation) was reported[31], and the notion that a particle acceleration process may be competing with this adiabatic deceleration was also introduced[44]. This "energy-change problem," which has received a good deal of attention lately[45,46,47,48], is still unsolved.

6) Particle Anisotropy -- The anisotropy in the flux of ~10 MeV protons has been observed to change magnitude and direction during a flare event[15,26,40,49,50]. A completely successful solar flare model must explain these anisotropy observations in at least a qualitative fashion.

The most important solar flare models that have been developed to date are summarized in Table V-1. The ADB solution of Burlaga[10] appears to explain the behavior of ≳100 MeV protons fairly well. However, no *analytic* solution exists which can fit *both* the rise and decay observations for low energy protons (~1-10 MeV) while including the effects of convection and energy-change which have been demonstrated to be significant at low energies[11,12].

In the discussion which follows, a new analytic solution will be developed which includes a boundary to the diffusing region at r = L, assumes instantaneous particle injection at one point, uses κ_r = constant*, and includes the effects of convection and energy-change. It will be demonstrated that this solution agrees well with near-earth observations of low energy solar flare protons using reasonable values of κ_r and L without the assumption of a scatter-free region near the sun. The predictions of the model will also be compared with the existing data concerning energy-change processes.

The new solution presented is really concerned with the *radial* transport of solar cosmic rays, which can be separated from the problem

*κ_r is identical to $\kappa_{\parallel}$ if one assumes a radial magnetic field.

TABLE V-1

Some Analytic Solutions to the Fokker-Planck Equation for Solar Flare Particle Propagation

Author	Diffusion Tensor	Outer Boundary?	Convection and Energy-Change Effects Included	Comments
Krimigis[36] 1965	isotropic diffusion $\kappa \propto r^{\beta}$	no	no	nonexponential decay, inapplicable at low energies
Burlaga[10] 1967	anisotropic diffusion† $\kappa_\theta \propto r^2$ κ_r = constant	yes	no	rapid rise* and exponential decay, but inapplicable at low energies
Fisk and Axford[11] 1968	isotropic diffusion $\kappa = \kappa_o r$	no	yes	slow rise* and nonexponential decay
Forman[12] 1971	anisotropic diffusion† $\kappa_\theta \propto r^2$ $\kappa_r = \kappa_o r$	yes	yes	exponential decay but slow rise*
Ng and Gleeson[13,14] 1971	quasi-radial diffusion along spiral field $\kappa_\perp = 0$ $\kappa_\parallel = \kappa_o r/\cos^2\psi$	no	yes	behavior probably similar to solution of Fisk and Axford
The New Solution[37]	anisotropic diffusion† $\kappa_\theta \propto r^2$ κ_r = constant	yes	yes	can fit <u>both</u>* rise and decay times while including convection and adiabatic dec.

*As expected, a solution using $\kappa_r = \kappa_o r$ predicts an intensity rise time at 1 AU which is much longer than the 5-10 hrs. frequently observed. However, κ_r = constant can result in much faster rise times.

†Here $\underline{\underline{\kappa}}$ is diagonal in a reference frame aligned with the radial direction, and is characterized by κ_r and $\kappa_\theta = \kappa_\phi$. If one assumes a radial magnetic field, then $\kappa_r = \kappa_\parallel$ and $\kappa_\theta = \kappa_\perp$.

of *azimuthal* propagation. Evidently this "perpendicular" particle transport cannot be explained with only the simple interplanetary diffusion process used in the discussion which follows. Nevertheless, a brief description of this "longitudinal distribution" problem will be given, even though the real answer must be left to those with access to multiple spacecraft measurements.

The predictions of the model will also be compared with observations of the vector particle anisotropy at 1 AU. It will be shown that the new solution is capable of explaining most of the features of these anisotropy measurements.

B. Background

A short description will now be given of the present state of knowledge concerning the interplanetary medium, the manner in which solar cosmic rays propagate through this medium, and the sorts of particle observations that result from solar-flare type injection.

1. The Interplanetary Medium

Unlike the problems of particle propagation, the features of interplanetary space are now fairly well understood, particularly in the vicinity of the earth. Several coherent summaries of the characteristics of the interplanetary medium as related to solar cosmic rays have been given[1,26,29].

Interplanetary space consists primarily of a highly conductive but nearly electrically neutral plasma which is an extension of the solar corona and is moving radially outward in all directions. This "solar

wind," which "blows" at a velocity of 300 - 500 km/sec at 1 AU, dominates the interplanetary medium out to at least 5 AU and probably to 20 - 100 AU. The plasma, which is composed of roughly equal numbers of protons and electrons, has a temperature of ~2 x 10^6 ^oK at the corona. Near the earth, the plasma has cooled to ~10^4 to 10^5 ^oK and has a density of ~3 - 10 protons/cm^3.

Imbedded in the plasma is a magnetic field which originates in the solar photosphere. This B-field is rigidly coupled to the plasma due to the high conductivity, and consequently the field lines are drawn outward by the force of the solar wind. Because the photosphere, where the solar field originates, rotates with a period of ~27 days (at the equator), the interplanetary field is rotated into a spiral. Assuming a constant solar wind velocity V, the average field is well approximated by an Archimedian spiral[4]

$$r = \frac{V(\phi - \phi_o)}{\Omega \sin \theta} \qquad (5\text{-}2)$$

where (r,θ,ϕ) are spherical polar coordinates centered at the sun and Ω = 2.7 x 10^{-6} radians/sec is the angular velocity of solar rotation. The ambient field thus makes an angle $\psi(r) = \tan^{-1}(\Omega r/V)$ with respect to the radius vector. For $V \simeq 400$ km/sec and $r = 1$ AU, $\psi = 48^o$. The field intensity falls off roughly as r^{-2} due to the solar wind expansion, and has a value of ~5 x 10^{-5} gauss at 1 AU.

Superimposed on this large-scale field are small-scale fluctuations in the field direction and intensity which produce deviations from the average configuration. These irregularities act as scattering

centers for the energetic particles and lead to the notion of cosmic ray "diffusion." In addition, the solar wind plasma is permeated with various "transient phenomena" -- discontinuities, shock waves, and hydromagnetic waves -- which contribute to the fluctuations in the medium.

Measurements of the average direction of the magnetic field vector over many solar rotations have shown that the ecliptic plane is divided into fairly stable "sectors" of alternating field direction[51]. These sectors, which require several days each to rotate past the earth, appear to be correlated with geomagnetic storm activity. The sector boundaries may very well act as barriers to energetic particle propagation.

The solar wind interacts in a complex way with the quasi-dipole geomagnetic field, creating a bow shock and magnetosphere. The boundary between the geomagnetic and interplanetary fields is a separate branch of geophysics in itself, and is of importance here only as it affects the OGO-6 particle observations (see Section III-B).

2. The Fokker-Planck Equation and Particle Diffusion

The details of cosmic ray transport depend on both the large scale and small scale features of the interplanetary field. If the small scale fluctuations were not present, the energetic particles would be confined to gyrate about individual field lines like beads sliding along wires. However, the field irregularities or "kinks" act as resonant scattering centers whenever the scale-length of the irregularity is of the same order as the particle gyro-radius. The scattered

particles thus random walk in both pitch angle and position, and the propagation can be approximated by a diffusion tensor $\underline{\underline{\kappa}}$. In a reference frame with the z-axis along the average field direction,

$$\kappa_{ij} = \begin{pmatrix} \kappa_\perp & -\kappa_d & 0 \\ \kappa_d & \kappa_\perp & 0 \\ 0 & 0 & \kappa_\parallel \end{pmatrix} \qquad (5\text{-}3)$$

where $\kappa_\parallel$ characterizes the particle diffusion along the field lines, $\kappa_\perp$ across the field lines, and κ_d includes the effects of curvature and gradient drifts[1]. The diffusion is anisotropic because of the average magnetic field structure present.

The picture is further complicated because the scattering centers are imbedded in the moving solar wind plasma. Since the field irregularities are convected outward by the solar wind, there is a net outward particle transport or convection separate from the particle diffusion process. In addition, the solar wind is continually expanding to fill interplanetary space ($\vec{\nabla} \cdot \vec{V} \neq 0$), and the field irregularities are thus on the average moving away from each other. This expansion produces an adiabatic cooling or deceleration of the cosmic rays at the rate[4]

$$\frac{dT}{dt} = -\frac{1}{3}\,\alpha(T)\,T\,(\vec{\nabla} \cdot \vec{V}) \qquad (5\text{-}4)$$

There is some question as to whether this is the only important energy-change process at work in interplanetary space[31,44].

All of these particle propagation effects can be combined into a single differential equation for the time rate of change of the particle density:

$$\frac{\partial n}{\partial t} = \vec{\nabla} \cdot (\underline{\underline{\kappa}} \cdot \vec{\nabla} n) - \vec{\nabla} \cdot (n\vec{V}) + \frac{1}{3}\vec{\nabla} \cdot \vec{V} \left[\frac{\partial}{\partial T} (\alpha(T)Tn)\right] \quad (5\text{-}5)$$

The right-hand side of this form for the Fokker-Planck equation includes terms for particle diffusion, convection, and adiabatic deceleration. This equation gives an adequate description of energetic particle transport as long as the pitch angle scattering can be characterized by a diffusion tensor. The Fokker-Planck equation is not valid whenever a large pitch angle anisotropy is present,[1] and other approaches must be used[52,53].

Although the validity of the Fokker-Planck equation is generally accepted, the exact nature of the diffusion tensor $\underline{\underline{\kappa}}$ is still undefined, largely because of the lack of adequate space-probe observations. The only real agreement seems to be that the antisymmetric terms can in most cases be ignored ($\kappa_d \simeq 0$) and that $\kappa_{\parallel}$ and $\kappa_{\perp}$ probably depend on both particle energy T and heliocentric distance r.

Jokipii[1] has shown that the diffusion coefficient $\underline{\underline{\kappa}}(T)$ can be related to the power spectrum of the fluctuations in the magnetic field. Using Mariner IV magnetic field observations, Jokipii[1,54,55], and Jokipii and Coleman[38] have obtained the following values for $\kappa_{\parallel}$ at r = 1 AU as a function of particle rigidity R (in GV) and velocity $\beta = \frac{v}{c}$:

$$\kappa_{\parallel} \approx \begin{cases} (5 \times 10^{21})\ \beta\sqrt{R}\ \text{cm}^2/\text{sec} & 0.1 \lesssim R \lesssim 1\ \text{GV} \\ (1.5 \times 10^{21})\beta\ R^2\ \text{cm}^2/\text{sec} & R \gtrsim 1\ \text{GV} \end{cases} \qquad (5\text{-}6)$$

For rigidities below 1 GV, $\kappa_{\perp}$ is dominated by the random walk of the field lines rather than by actual particle scattering, and Jokipii[1, 55] derives

$$\kappa_{\perp} \approx 7.5 \times 10^{20}\beta\ \text{cm}^2/\text{sec for}\ \ R \lesssim 1\ \text{GV} \qquad (5\text{-}7)$$

In a recent paper, Jokipii[56] has demonstrated that his pitch-angle scattering approach, once thought to break down for $R \lesssim 0.1$ GV, can be safely extended to much lower rigidities.

Figure V-1 compares the semi-empirical values for $\kappa_{\parallel}$ and $\kappa_{\perp}$ just discussed with values of κ derived from measurements during the rise of solar flare events, assuming isotropic diffusion[26]. It should be emphasized that the Jokipii and Coleman values for κ are based on a small sample of magnetic field measurements made in 1964 and therefore must be taken only as estimates. The figure makes it obvious that very little is known about κ below ~10 MeV.

The dependence of $\underline{\underline{\kappa}}$ on r is even more of a mystery. Although Mariner IV observations indicate that $\kappa_{\parallel}$ is constant between 1.0 and 1.5 AU,[38] nothing is known about the important r-dependence of $\kappa_{\parallel}$ near the sun. Although experimental measurements for $\kappa_{\perp}$ are largely lacking, some simple theoretical arguments based on the random walk of the

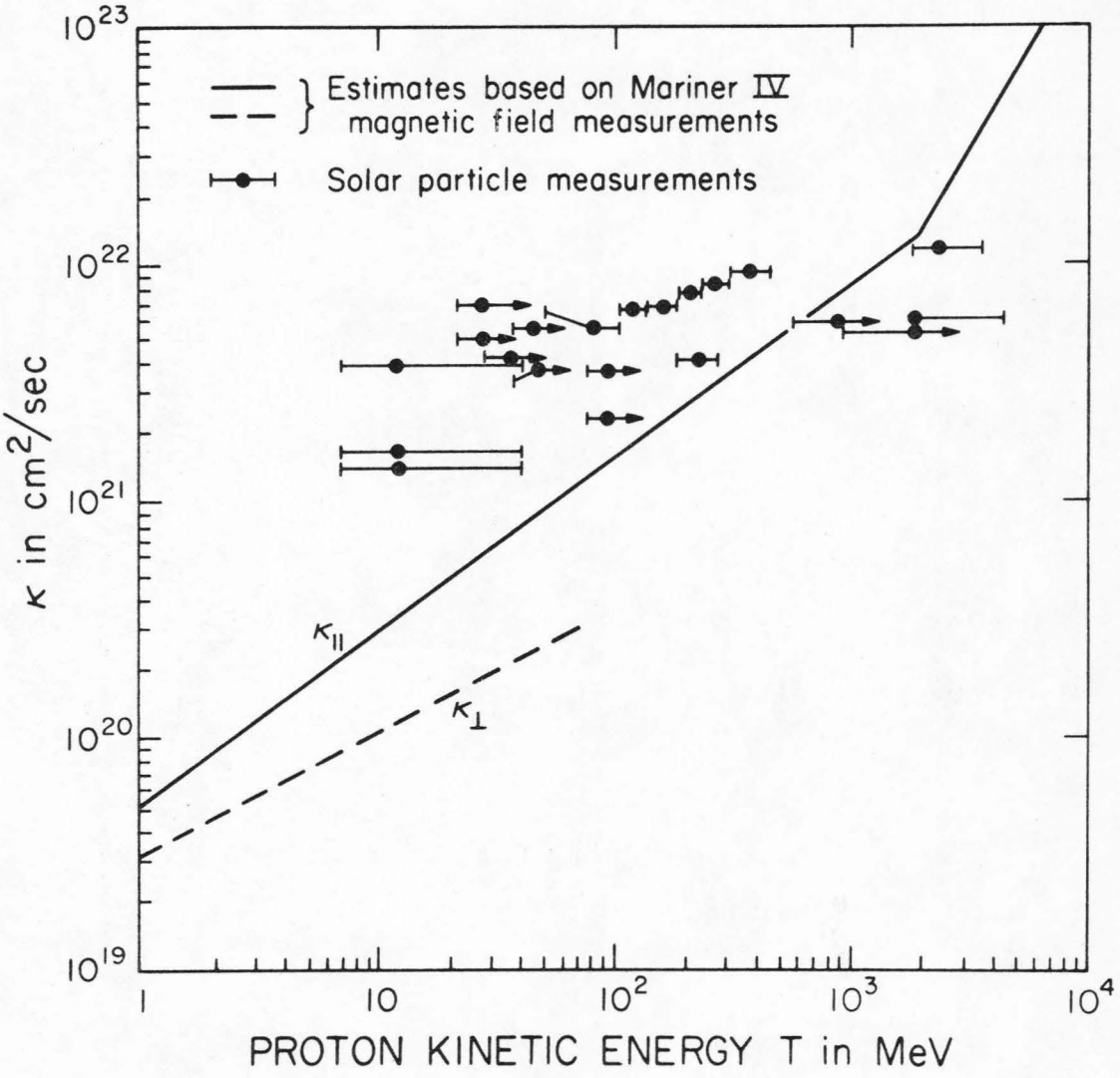

Figure V-1: The diffusion coefficient κ is plotted vs. proton kinetic energy T. The lines represent the best estimates for $\kappa_{\parallel}$ and $\kappa_{\perp}$ of Jokipii[1,54,55,56] and Jokipii and Coleman[38] based on the power spectrum of fluctuations in the magnetic field. The points are the results of solar particle measurements summarized by McCracken and Rao[26].

field lines, indicate that $\kappa_\perp$ should vary as r^2. In addition, the assumption of an r^2 dependence for $\kappa_\perp$ makes the equation easily soluble. As mentioned previously, it is possible that the azimuthal particle transport is dominated by a separate near-sun diffusion region and that perpendicular diffusion in interplanetary space is relatively unimportant.

Since the Fokker-Planck equation can be solved much more easily if any of the terms can be neglected, it is of interest to calculate the relative magnitudes of the various terms. Using the value of κ at 1 MeV from Figure V-1, a solar wind velocity V = 400 km/sec, and assuming that the scale length ℓ for changes in the density is about 1 AU, the diffusive term becomes:

$$\vec{\nabla} \cdot (\underline{\underline{\kappa}} \cdot \vec{\nabla} n) \approx \frac{\kappa n}{\ell^2} = n \frac{(6 \times 10^{19} \text{ cm}^2/\text{sec})}{(1.5 \times 10^{13} \text{ cm})^2} \simeq n(3 \times 10^{-7} \text{sec}^{-1})$$

For comparison, the convection term is roughly

$$\vec{\nabla} \cdot n\vec{V} \approx \frac{Vn}{\ell} = n \frac{(4 \times 10^{7} \text{ cm/sec})}{(1.5 \times 10^{13} \text{cm})} \simeq n(3 \times 10^{-6} \text{sec}^{-1})$$

This crude calculation indicates that "solar wind" effects are very important when the diffusion coefficient is small. It is thus a violation of the basic physics of the Fokker-Planck equation to ignore the terms for convection and adiabatic deceleration at low proton energies.

3. Solar Flare Particle Events

McCracken and Rao[26] have classified solar flare particle events as either *prompt*, occurring within hours of the parent flare, or *delayed*, occurring $\gtrsim$ 24 hours after the parent flare or even without an obvious optical flare association. In fact, it is no longer believed that flare particles are always injected impulsively at the sun[29] -- proton precursors have been observed, and many flare particle events have been explained in terms of particle storage and/or continual production at the sun. Nevertheless, a large fraction of the so-called "prompt" events appear to be consistent with impulsive injection and can be clearly associated with a parent optical flare. The four event observations presented in Section IV fall into this group, and it is this class of particle events which is the subject of this dissertation.

Solar flare particle events have been observed at 1 AU for many years, and as a result, the behavior of the "typical" event has been fairly well defined[25,26,29]. The following are a few of the commonly observed characteristics of prompt solar flare events which any solar flare model must attempt to explain:

a) The intensity vs. time profile for most prompt events is characterized by a rapid increase to maximum intensity followed by a decay phase which at late times is approximately exponential. The time-to-maximum T_m is typically 5 - 35 hours, and the exponential decay time constant $\tau \approx 8$ - 27 hours.

b) The shape of the profile, especially during the rise,

depends strongly on the distance in heliocentric longitude between the flare and the foot of the line of force connected to the observer. (The foot of the line of force passing through the earth is typically at 60°W solar longitude). T_m is greater for east-limb events because the longitudinal separation ϕ is greater (compare the 7 June 69 event of Figure IV-2 with the events of 2 Nov 69 and 31 Jan 70). Burlaga[10] has shown that T_m varies roughly as ϕ^2. McCracken[57] has pointed out that particles from west-limb flares are more frequently detected than those from east-limb events, even though the parent optical flares occur in the east and west with equal probability.

c) A well-defined velocity dispersion is seen, especially for west-limb events. As expected, the high energy or faster particles arrive first.

d) The low energy (~1 MeV) protons last longer (decay more slowly) and exhibit more intensity variation than the higher energy protons.

e) The typical vector anisotropy observation is characterized by a strong anisotropy from ~45°W early in the event which later decreases to a smaller equilibrium value directed from ~45°E at late times[15]. McCracken[57] reports that the anisotropy measured using neutron monitor data is strongest for west limb events.

This completes the discussion of what is known about solar flare particle propagation through interplanetary space and should set the

stage for the following attempt to describe this propagation.

C. Solving the Fokker-Planck Equation for Solar Flare Particle Injection

1. Some Boundary Conditions and Simplifying Assumptions

The following is a list of assumptions, conventions and boundary conditions which will be applied to the Fokker-Planck equation:

a) The particle density n depends only on spatial position (r, θ, ϕ), time t, and particle kinetic energy T.

b) All parameters except for the particle density n are assumed to be independent of energy T. One can set $\alpha(T) = 2$ for protons below ~100 MeV.

c) The solar wind velocity $\vec{V}$ is radial and independent of (r, θ, ϕ) and t.

d) No attempt is made to describe transient phenomena such as solar wind fluctuations, shock waves, and hydromagnetic waves.

e) The particles are impulsively injected at $r = r_s$ at time $t = 0$. Specifically,

$$n(r, \theta, \phi, t = 0) = \frac{\delta(r - r_s)}{r^2} f(\theta, \phi) \qquad (5\text{-}8)$$

f) It is required that the density n remain finite as $r \to 0$.

g) A perfectly absorbing boundary exists at $r = L$ such that $n(L, \theta, \phi, t) = 0$.

h) The diffusion tensor will be taken to be diagonal in a frame of reference (r, θ, ϕ) aligned with the radial direction.

Specifically, $\underline{\underline{\kappa}}$ will be defined by $\kappa_\theta = \kappa_\phi = \kappa_1 r^2$ and $\kappa_r = \kappa$ = constant, both independent of energy T.

These assumptions are intended to facilitate a solution to the equation without compromising any of the important physics involved. The most serious simplifications are that $\underline{\underline{\kappa}}$ is independent of energy T and aligned with the radial direction. It will be shown that the energy-dependence can be approximated by breaking the energy domain into separate intervals within which κ is independent of T, as long as the intervals are large with respect to the ~30% energy-change which has been observed to occur during a typical ~3 day decay period[31].

Some additional comment should be made about the assumed diagonal form for the diffusion tensor:

$$\kappa_{ij} = \begin{pmatrix} \kappa_r & 0 & 0 \\ 0 & \kappa_\theta & 0 \\ 0 & 0 & \kappa_\phi \end{pmatrix}$$

This is *not* identical to the assumption of a radial magnetic field. However, the simplest and most widely-used interpretation of this assumption is to equate it with the neglect of the spiral field. Then $\kappa_r = \kappa_\parallel$, $\kappa_\theta = \kappa_\phi = \kappa_\perp$, and one must make an additional distinction between actual radial distances in interplanetary space and the radius variable r, which now represents a path length measured along a spiral field line. This interpretation, which sacrifices surprisingly little of the physics involved, will be adopted in this discussion until a treatment of the anisotropy is attempted.

The boundary condition at the sun would seem to be more appropriately described by either a perfectly absorbing or perfectly reflecting boundary at $r = r_s$ (instead of at the origin). However, a recent paper by Englade[58] indicates that the type of solar boundary condition assumed has little effect on the time profile observed at 1 AU. Evidently more appropriate inner boundary conditions serve only to make the solution less manageable.

The existence of an outer absorbing boundary is not an accepted point. Several authors have developed solutions using an infinite diffusing region (see Table V-1). In particular, Ng and Gleeson[13] claim that an "approximately" exponential decay can be produced assuming $\kappa_{\parallel} = \kappa_o(1 + r^3)$. However, their $\kappa_{\parallel}$ function appears to be just another way of smoothly introducing a region of free escape where $\kappa \to \infty$ and $n \to 0$. The fact remains that observations of exponential decays are the rule rather than the exception, and a free escape boundary produces such a decay.

The r-dependence for κ_r is a very important assumption, as will be demonstrated later in the discussion.

2. Separation of Variables

We are now in a position to attack the Fokker-Planck equation using the technique of separation of variables. Assuming a radial magnetic field, a diffusion tensor defined by $\kappa_r(r)$ and $\kappa_\theta(r) = \kappa_1 r^2$ both independent of T, and V independent of spatial position, one can rewrite equation (5-5) in spherical polar coordinates as:

$$\frac{\partial n}{\partial t} = \frac{1}{r^2}\frac{\partial}{\partial r} r^2 \kappa_r(r) \frac{\partial n}{\partial r} + \frac{\kappa_1}{\sin\theta} \frac{\partial}{\partial \theta} \left(\sin\theta \frac{\partial n}{\partial \theta}\right)$$

$$+ \frac{\kappa_1}{\sin^2} \frac{\partial^2 n}{\partial \phi^2} - V \frac{\partial n}{\partial r} - \frac{2Vn}{r} \left[1 - \frac{1}{3n} \frac{\partial}{\partial T} (\alpha(T) T n)\right] \tag{5-9}$$

Assuming $n(r, \theta, \phi, t) = R(r, t)\, Q(\theta, \phi, t)\, S(T)$ the equation separates into the following three equations:

$$\frac{\kappa_1}{\sin\theta} \frac{\partial}{\partial \theta} \sin\theta \frac{\partial Q}{\partial \theta} + \frac{\kappa_1}{\sin^2\theta} \frac{\partial^2 Q}{\partial \phi^2} = \frac{\partial Q}{\partial t} \tag{5-10}$$

$$\frac{1}{r^2} \frac{\partial}{\partial r} \left[r^2 \kappa_r(r) \frac{\partial R}{\partial r}\right] - V \frac{\partial R}{\partial r} - \frac{2CV}{r} R = \frac{\partial R}{\partial t} \tag{5-11}$$

$$\frac{\partial}{\partial T} (\alpha T S) = 3S(1 - C) \tag{5-12}$$

Note that it is not necessary to specify the form of $\kappa_r(r)$ to carry out the separation.

3. The Azimuthal Dependence

The azimuthal function $Q(\theta, \phi, t)$, which is the solution to equation (5-10), gives the density distribution in heliocentric latitude and longitude at time t. The solution, which is derived in detail in Appendix B, is identical to the azimuthal function used by Burlaga[10] and Forman[12]:

$$Q(\gamma, t) = \sum_{\ell=0}^{\infty} C_\ell P_\ell (\cos\gamma)\, e^{-\ell(\ell+1)\kappa_1 t} \tag{5-13}$$

where $\cos\gamma = \cos\theta \cos\theta_o + \sin\theta \sin\theta_o \cos(\phi - \phi_o)$ (5-14)

(θ, ϕ) = point of observation

(θ_o, ϕ_o) = center of azimuthal distribution

The C_ℓ are chosen so that $Q(\gamma, t=0)$ matches $f(\theta, \phi)$, the assumed injection profile at the sun. For δ-function injection at $\gamma = 0$, we have $C_\ell = 2\ell + 1$ and

$$Q(\gamma, t) = \sum_{\ell=0}^{\infty} (2\ell + 1) P_\ell (\cos\gamma) e^{-\ell(\ell+1)\kappa_1 t} \quad (5\text{-}15)$$

Burlaga[10] has described the behavior of this $Q(\gamma, t)$ function in some detail.

Feit[59] has shown that for a source uniform over an emission cone of half-angle γ_o:

$$C_\ell = \frac{P_{\ell-1}(\cos\gamma_o) - P_{\ell+1}(\cos\gamma_o)}{1 - \cos\gamma_o} \quad (5\text{-}16)$$

Presumably any symmetric $f(\theta, \phi)$ can be generated using the proper coefficients C_ℓ.

If we choose our coordinate system coincident with the accepted solar spherical coordinates, then our observation point at earth corresponds to $\theta = \frac{\pi}{2}$, $\phi = \frac{\Omega r}{V}$. The angle ϕ, which is 58^o for r = 1 AU and V = 400 km/sec, indicates that the earth is typically connected by the spiral field to a point at ~58°W solar longitude on the sun. We can thus define a new separation angle γ' which is a function of time t and

includes both corotation and the spiral angle:

$$\cos\gamma' = \sin\theta_o \cos(\phi_o(t) - \phi)$$
$$= \cos\lambda_o \cos(\Phi_o - \frac{\Omega r}{V} + \Omega t) \qquad (5\text{-}17)$$

where $\lambda_o = \frac{\pi}{2} - \theta_o$ = solar latitude of optical flare

$\phi_o(t) = \Phi_o + \Omega t$ = the actual time-dependent solar longitude of flare location

and Φ_o = solar longitude of optical flare at t = 0

($\Phi_o > 0$ for W longitude)

It should be mentioned here that the above formulation of the perpendicular transport process is probably far too simple to accurately describe the actual situation. Multiple spacecraft observations of particle fluxes and anisotropies indicate that rapid near-sun diffusion and/or particle injection over a large solar surface area should be invoked[15, 26, 40, 41]. Despite this evidence, the simple point-injection and 2-dimensional interplanetary diffusion process described by equation 5-15 will be employed in the discussion which follows. The shortcomings of this simple $Q(\gamma,t)$ function, which will be discussed carefully, do not in any way affect the validity of the new solution for *radial* particle transport.

4. The Energy Dependence

Equation 5-12 for S(T) can be reduced to the following form:

$$\alpha(T)T\frac{\partial S}{\partial T} = \left[3 - 3C - \alpha(T) + T\frac{\partial \alpha}{\partial T}\right] S \qquad (5\text{-}18)$$

For $T_{proton} \lesssim 100$ MeV, $\alpha(T) = 2$ and $\frac{\partial \alpha}{\partial T} << 1$, and the energy equation becomes

$$\frac{\partial S}{\partial T} = \left(\frac{1 - 3C}{2T}\right) S \qquad (5\text{-}19)$$

with a solution of the form $S(T) = S_o T^{-\gamma}$

where $\gamma = \frac{3C - 1}{2}$ is the power law index of the density. In principle, any initial spectrum S(T) can be described by this solution by an appropriate super-position of power laws:

$$S(T) = \sum_i A_i \, T^{-\gamma i} \qquad (5\text{-}20)$$

The separation constant C is the Compton-Getting factor[12]

$$C = 1 - \frac{1}{3n} \frac{\partial}{\partial T} \left[\alpha(T) \, Tn\right] \qquad (5\text{-}21)$$

For low energy protons, assuming that adiabatic deceleration is the only energy-change process operative, this becomes $C = \frac{2\gamma + 1}{3}$ (5-22)

The solution can be generalized to describe any combination of energy-change processes by introducing a variable $\tau_E(r) = \tau_o r$, which is the energy-change time constant[17]. The generalized Compton-Getting factor then becomes:

$$C = 1 - \frac{(\gamma - 1)}{2V\tau_o} \qquad (5\text{-}23)$$

which will account for any energy-change process which varies as 1/r. Note that pure adiabatic deceleration corresponds to $\tau_o = \frac{3}{4V}$, and a value of C = 1 corresponds to no energy-change effect at all.

5. The Radial Dependence

Most of the features of a solar flare event observed at 1 AU are due to the "radial" transport involving convection, energy-change, and diffusion parallel to the field lines. For this reason, much effort has been devoted to solving the radial equation (equation 5-11). Even if the perpendicular diffusion is neglected ($\kappa_\theta = 0$), the equation describing the radial propagation remains unchanged.

Burlaga[10], has solved the radial equation by neglecting the terms for convection and energy-change, including a perfectly absorbing boundary at r = L, and assuming $\kappa_r(r) = \kappa$. His differential equation becomes

$$\frac{\partial^2 R}{\partial r^2} + \frac{2}{r}\frac{\partial R}{\partial r} = \frac{1}{\kappa}\frac{\partial R}{\partial t} \qquad (5\text{-}24)$$

He derives the following eigenvalue expansion for the radial dependence:

$$R(r,t) = \frac{A}{r r_s L}\sum_{n=1}^{\infty} \sin\left(\frac{n\pi}{L} r_s\right) \sin\left(\frac{n\pi}{L} r\right) \exp\left(\frac{-n^2\pi^2\kappa t}{L^2}\right) \qquad (5\text{-}25)$$

where the constant A is an arbitrary normalization determined by the number of particles injected. His overall solution which includes the azimuthal distribution, is

$$n(r, \theta, \phi, t) = R(r,t)\, Q(\theta, \phi, t) \qquad (5\text{-}26)$$

Burlaga's solution produces a rapid rise and an exponential decay and thus adequately describes the time profile of high energy ($T \gtrsim 100$ MeV) protons observed at earth. However, this solution is inapplicable to

observations of ~1 MeV protons because it does not include the convection and energy-change terms which become important for small values of κ_r.

Forman[12] has solved the radial equation in the form

$$\frac{\partial^2 R}{\partial r^2} + \left(\frac{3}{r} - \frac{V}{\kappa_o r} \right) \frac{\partial R}{\partial r} - \frac{2CV}{\kappa_o r^2} R = \frac{1}{\kappa_o r} \frac{\partial R}{\partial t} \tag{5-27}$$

including convection, energy-changes, and a boundary, but using $\kappa_r(r) = \kappa_o r$. Her radial solution is

$$R(r,t) = \frac{A}{r_s^2 L} \left(\frac{r}{r_s} \right)^{\frac{V}{2\kappa_o} - 1} \sum_{n=1}^{\infty} \frac{J_\eta(j_{\eta,n} \sqrt{r_s/L})\ J_\eta(j_{\eta,n} \sqrt{r/L})\ \exp(-t/\tau_n)}{\left[J_{\eta+1}(j_{\eta,n}) \right]^2} \tag{5-28}$$

where $J_\eta(x)$ is the Bessel function of order η, and $j_{\eta,n}$ is the n^{th} zero of $J_\eta(x)$. Also

$$\eta = 2 \sqrt{\left(1 - \frac{V}{2\kappa_o} \right)^2 + \frac{2CV}{\kappa_o}} \tag{5-29}$$

and

$$\tau_n = \frac{4L}{\kappa_o (j_{\eta,n})^2} \tag{5-30}$$

As will be demonstrated later, this solution adequately describes the decay phase of flare events, but because of the $\kappa_r = \kappa_o r$ dependence

chosen, predicts a rise time which is slower than the 5-10 hours observed.

D. The New Solution

1. Derivation

It is apparent that a solution to the radial equation (equation 5-11) similar to Forman's but using $\kappa_r(r)$ = constant might yield desirable results. The equation becomes

$$\frac{\partial^2 R}{\partial r^2} + \left(\frac{2}{r} - \frac{V}{\kappa}\right)\frac{\partial R}{\partial r} - \frac{2CV}{\kappa r}R = \frac{1}{\kappa}\frac{\partial R}{\partial t} \qquad (5\text{-}31)$$

A solution has in fact been found using the boundary conditions and assumptions listed in Section V-C-1. The details of the derivation are given in Appendix C.

The new solution, which was recently reported[37], can be written as the following eigenvalue expansion:

$$R(r,t) = A\,\frac{\exp\left[V(r - r_s)/2\kappa\right]}{r\,r_s} \qquad (5\text{-}32)$$

$$\sum_{n=1}^{\infty} \frac{F_o(\beta/2\sqrt{\alpha_n}, \sqrt{\alpha_n}\, r_s)\, F_o(\beta/2\sqrt{\alpha_n}, \sqrt{\alpha_n}\, r)}{N_n} e^{-t/\tau_n}$$

where $F_o(\eta,\rho)$ is the regular Coulomb wave function[60]. The α_n are the eigenvalues defined by the outer boundary condition

$$F_o(\beta/2\sqrt{\alpha_n}, \sqrt{\alpha_n}\, L) = 0 \quad . \qquad (5\text{-}33)$$

The other parameters are defined as follows:

$$\beta = V(2C - 1)/\kappa \tag{5-34}$$

C = Compton-Getting Factor

$$= 1 + (\gamma - 1)/2V\tau_o \tag{5-35}$$

$$\tau_n = 4\kappa/(4\kappa^2\alpha_n + V^2) \tag{5-36}$$

$$N_n = \int_o^L \left[F_o\left(\beta/2\sqrt{\alpha_n}, \sqrt{\alpha_n}\, x\right)\right]^2 dx$$

$$= \left[\frac{x}{2}\left(\frac{\partial F_o}{\partial \rho}\right)^2 - \frac{\beta}{4\alpha_n}\left(\frac{\partial F_o}{\partial \rho}\right)\left(\frac{\partial F_o}{\partial \eta}\right)\right]_{x=L} \tag{5-37}$$

$$\left[\text{here } F_o(\eta,\rho) = F_o\left(\beta/2\sqrt{\alpha_n}, \sqrt{\alpha_n}\, x\right)\right]$$

A = arbitrary normalization

This expansion converges rapidly for $t \gtrsim 5$ hours, $C \lesssim 4$, and $\kappa \gtrsim 10^{20}$ cm^2/sec. The details of calculating the radial solution are discussed in Appendix D.

In the limit as $V \to 0$, we have $\beta \to 0$, $F_o\left(\beta/2\sqrt{\alpha_n}, \sqrt{\alpha_n}x\right) \to \sin(n\pi x/L)$, $\tau_n \to L^2/n^2\pi^2\kappa$, $N_n \to \frac{L}{2}$ and the solution reduces smoothly to Burlaga's solution (equation 5-25) as expected.

The complete solution including the energy-dependence can now be written as:

$$n(r,\theta,\phi,t,T) = Q(\theta,\phi,t) \sum_{i=1}^{\infty} A_i\, T^{-\gamma i}\, R_i(r,t) \tag{5-38}$$

which consists of a sum over different radial functions $R_i(r,t)$ each

corresponding to a different Compton-Getting factor $C_i \equiv 1 + (\gamma_i - 1)/2V\tau_o$. Equation 5-38 is thus the response to impulsive injection of the form

$$n(r,\theta,\phi,t=0,T) = f(\theta,\phi) \frac{\delta(r - r_s)}{r^2} S(T) \qquad (5\text{-}39)$$

$$\text{with} \qquad S(T) = \sum_i A_i T^{-\gamma_i} \quad . \qquad (5\text{-}40)$$

2. Behavior of the Solution

The radial dependence $R(r,t)$, defined by equation 5-32, defines most of the features of the particle time profile. Figure V-2 shows the distribution of particles as a function of radial distance r at various times using reasonable values of the parameters. The peak in the particle distribution, which is initially near the sun due to the δ-function injection, moves outward until the effect of the absorbing boundary is felt and eventually assumes a stable "shape" at late times.

The time-profiles $R(r,t)$ vs. t observed at different radial distances r are shown in Figure V-3. As expected, the time-to-maximum T_m depends on the radial position of the observer because the maximum intensity occurs roughly when the peak in the radial distribution (Figure V-2) moves past the observation point. Note that the T_m observed at 1 AU is < 20 hours. At late times, the intensity decays exponentially with a time constant τ_{DEC} roughly independent of radial position. A glance at equation 5-32 makes it clear that only the first eigenvalue (n=1) survives and that the decay phase is described by the

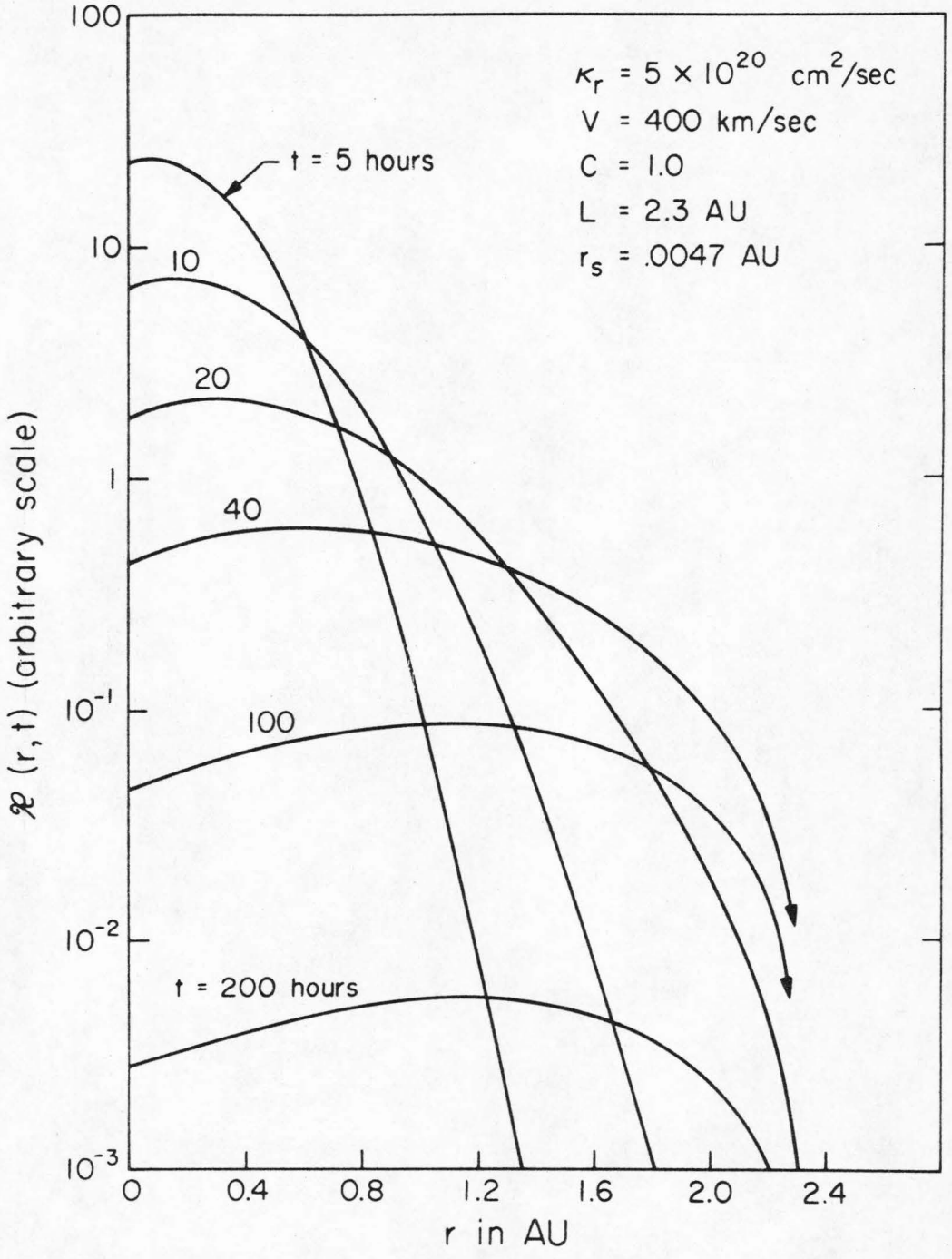

Figure V-2: The new radial solution $R(r,t)$, defined by equation 5-32, is plotted vs. radial distance r for various times after particle injection. Typical values of the parameters were chosen and are indicated on the graph. Note that the distribution, which is initially peaked near the sun due to the δ-function injection, reaches a stable configuration at late times.

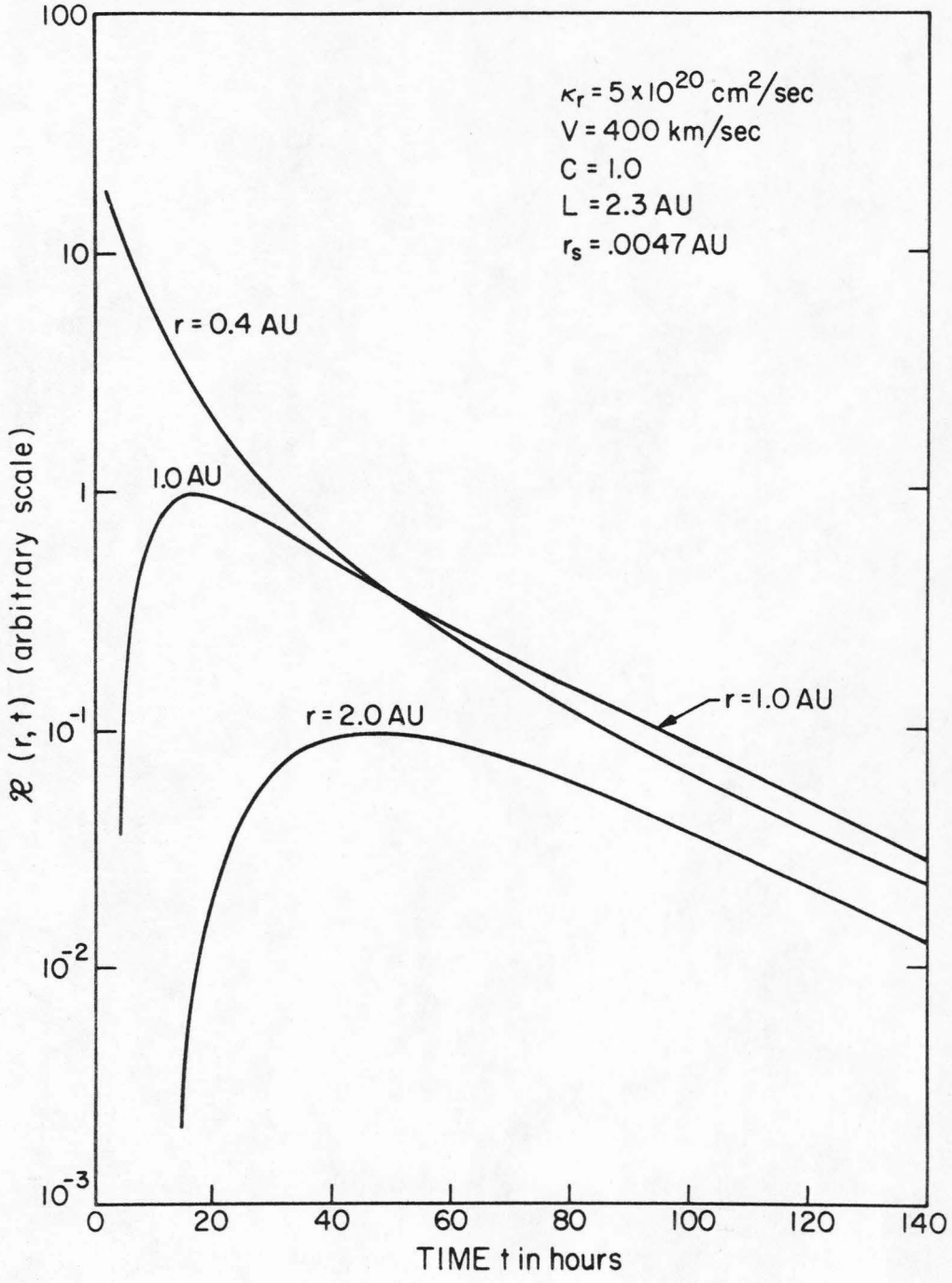

Figure V-3: The intensity R(r,t) predicted by the new solution is plotted vs. time for various observation distances r. Note that although the time-to-maximum depends on radial distance, the time-profile eventually reduces to an exponential decay independent of observer position. The values of the parameters, which are the same as in Figure V-2, are listed on the figure.

following equation:

$$R(r,t) \propto \frac{\exp(Vr/2\kappa)\, F_o(\beta/2\sqrt{\alpha_1}, \sqrt{\alpha_1} r)}{r} e^{-t/\tau_1} \qquad (5\text{-}41)$$

Thus if one is concerned only with the exponential decay phase of an event, the predictions of the new model can be summarized by the single quantity $\tau_{DEC} = \tau_1$, which is independent of position and time and depends only on the boundary location L, the solar wind speed V, the diffusion coefficient κ_r, and the energy-change parameter C.

Figure V-4 shows how τ_{DEC} varies with κ_r, L, V, and C. For small values of κ_r, τ_{DEC} becomes essentially independent of κ_r because the particle transport outward to the boundary is dominated by convection and energy-change processes. For large values of κ_r, the solar wind effects become unimportant, and the decay time constant approaches Burlaga's $(\kappa_r)^{-1}$ dependence.

Increasing the solar wind speed hastens the decay, as expected (Figure V-4a), because the contribution of both convection and energy-change to the decay rate is increased. In the limit $V \to 0$, τ_{DEC} becomes identical to Burlaga's expression (see equation 5-25).

Changing the boundary position L has a marked effect on the decay rate, as shown in Figure V-4b. The decay in the particle intensity is largely produced by the outward transport of the particles to the boundary, where they "escape." A more distant boundary means that the processes of diffusion and convection cannot deliver particles to the boundary at the same rate, and τ_{DEC} must increase accordingly. A close look at the behavior of the complete solution shows that at short

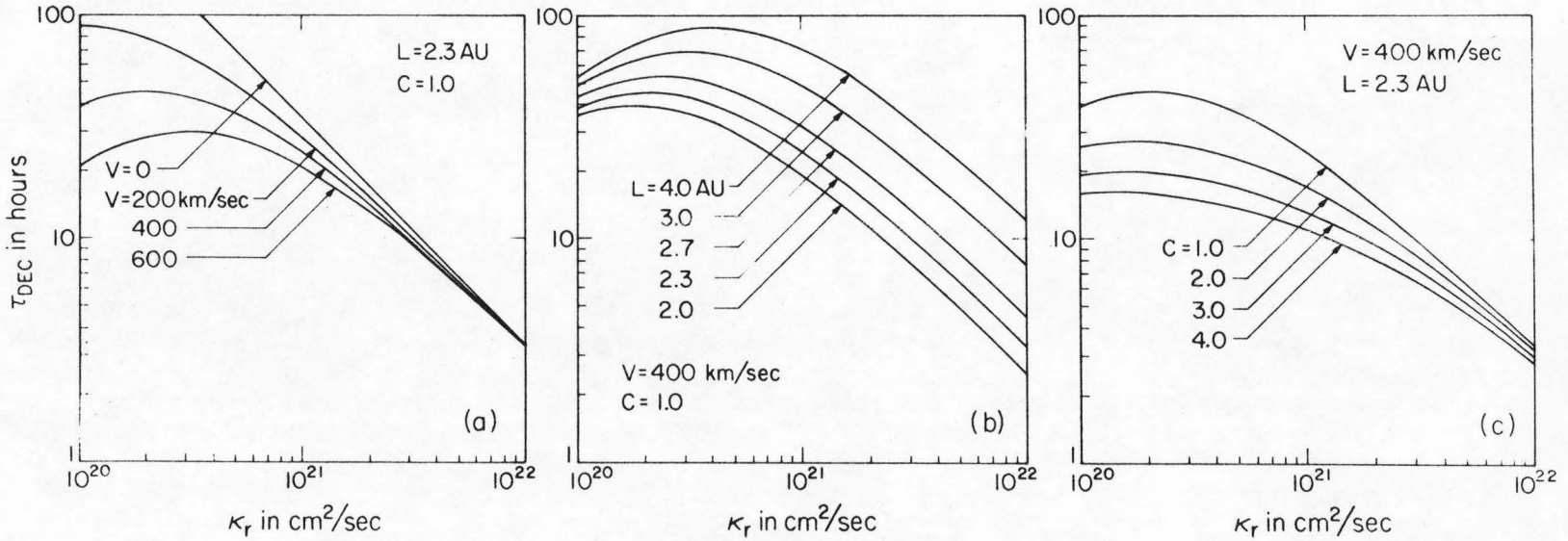

Figure V-4: The exponential decay time constant τ_{DEC} predicted by the new solution is plotted vs. κ_r for a) various values of the solar wind velocity V, b) various values of the boundary position L, and c) different values of the energy-change parameter C.

times, when the particles have not yet reached the boundary, the profile is independent of L.

The Compton-Getting factor C characterizes the extent to which the random walk of the particles in energy-space affects the decay. While a value of C = 1 corresponds to ignoring the energy-change effects completely, a typical value of C = 3 means that at L = 1 AU the intensity is decaying, due to the energy-change process, at a rate that can be estimated from equation 5-5:

$$\tau_{\substack{\text{ENERGY-}\\\text{CHANGE}}} = \frac{-n}{(\partial n/\partial t)} = \left(\frac{r}{2CV}\right) \simeq 17 \text{ hours} \qquad (5\text{-}42)$$

This is of the same order as the actual decay time constant and indicates that the contribution of C to the decay rate is significant -- a conclusion which is substantiated by Figure V-4c.

The relative distribution of particles f(r) in radial distance r at late times is given by

$$f(r) = \exp\left[Vr/2\kappa\right] r^{-1} F_o\left(\beta/2\sqrt{\alpha}_1, \sqrt{\alpha}_1\, r\right) \qquad (5\text{-}43)$$

and depends only on L, C, and the ratio V/κ. This function is shown in Figure V-5 for various typical values of this ratio. The boundary condition f(L) = 0 is quite evident. Again, for $V/\kappa \to 0$, f(r) reduces to Burlaga's $\sin(n\pi r/L)/r$ which is peaked at the origin. As V/κ is increased, the peak in the distribution becomes more pronounced and moves outward due to the increased convective force. The dependence of the position of this peak on V/κ has been discussed by Forman[48].

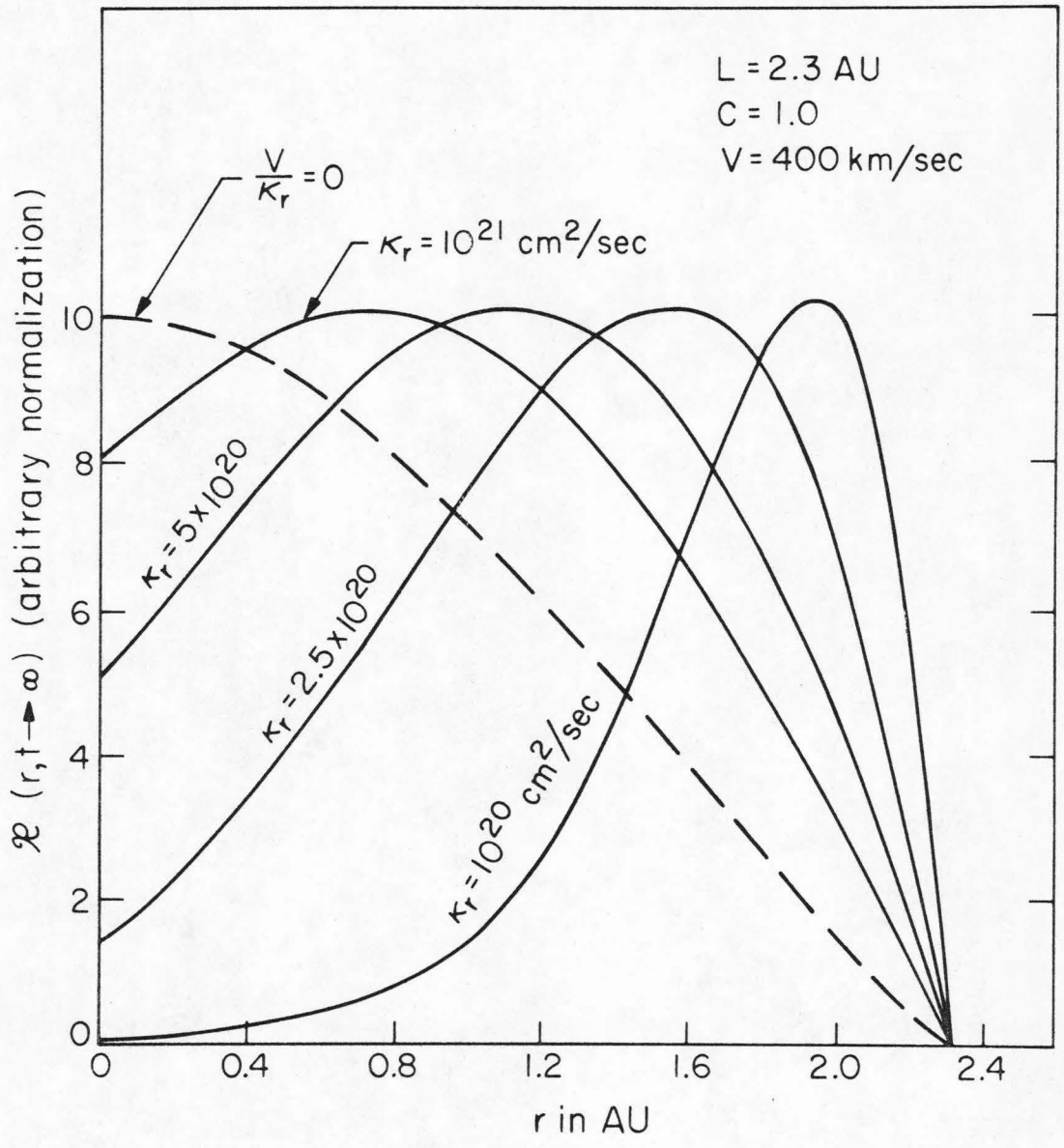

Figure V-5: The radial distribution of particles at late times is plotted vs. r for various values of the ratio V/κ_r.

The transport process occurring at any position r is best described by the particle current $\vec{S}$, which is simply the vector particle flux.

$$\vec{S} = C\vec{V}n - \underline{\underline{\kappa}} \cdot \vec{\nabla}n \qquad (5\text{-}44)$$

For the radial $\vec{B}$-field assumption used so far in this discussion, $\vec{S}$ is radial and can be treated as a scalar composed of two terms

$$S_V = CV\mathcal{R} \qquad (5\text{-}45)$$

and

$$S_\kappa = -\kappa_r \, \partial\mathcal{R}/\partial r \qquad (5\text{-}46)$$

which are the convective and diffusive components of the total particle current. Note the azimuthal part of the solution $Q(\gamma,t)$ has been neglected, and that S_V is proportional to the radial solution $\mathcal{R}(r,t)$, while S_κ is proportional to the slope $\partial\mathcal{R}/\partial r$.

Figure V-6, which shows the decay-phase values of S, S_V, and S_κ as a function of r, makes it clear which transport process is most important at any given radial distance. At the outer boundary, the net particle flux is outward and is due entirely to diffusion. Because the typical particle distribution at late-times is peaked at $r \gtrsim 1$ AU (see Figure V-5), the gradient over much of the distance is positive and the diffusive current S_κ in this region is directed inward. This inward diffusion, which impedes the process of particle escape, exactly balances with outward convective current at the origin to produce $S(r=0) = 0$.

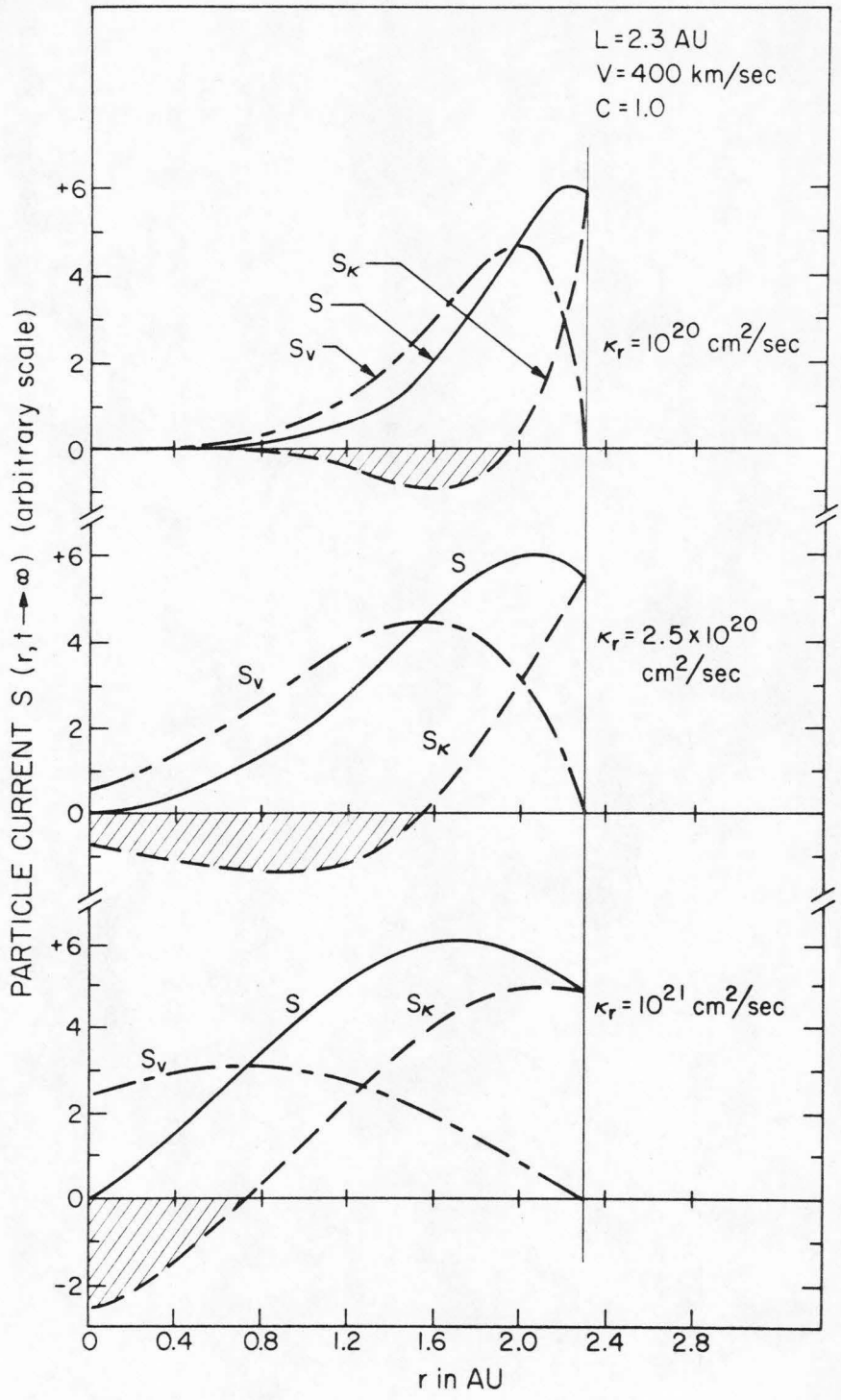

Figure V-6: The particle current S at late times as well as the convective and diffusive components, S_V and S_κ, are plotted vs. r for three values of κ_r. The shaded area emphasizes the region where the diffusive current S_κ is inward.

The decay time constant $\tau_{DEC} = n/(\partial n/\partial t)$ is a measure of the total "stored" particle population relative to the rate at which particles reach the boundary and escape. Figure V-4 shows that a broad maximum in τ_{DEC} vs. κ_r occurs typically for $\kappa_r \approx 2 \times 10^{20}$ cm^2/sec. This maximum in τ_{DEC}, which has been discussed by Forman[48], can be understood qualitatively as the certain combination of parameters which produces the lowest loss rate per unit stored particle.

E. Fits to Data Assuming Pure Adiabatic Deceleration

1. Method of Fitting Actual Data

Attempts were made to fit the flare event time-profiles described in Section IV using the solution of Forman and the new solution. In each case, the following assumptions and parameter values were employed:

a) It was assumed that adiabatic deceleration due to the solar wind expansion was the only energy-change process operative. The Compton-Getting factor C was thus defined in terms of the power law index γ of the particle density as $C = (2\gamma + 1)/3$ (see Section V-C-4).

b) Observations of the intensity within different energy bins were treated separately. The density was assumed to be a power law within each incident energy bin, and a separate value of C was thus assigned to each energy interval by evaluating $\gamma(T) = d(\ln n)/d(\ln T)$ at the center of the interval. The fact that the spectra of Figure IV-2 are stable with time indicates that the "mixing"

between various energy bins is not very pronounced, and that the description of each bin by means of an independent solution to the differential equation is reasonable. In the same way, the energy change rate reported by Murray et al.[31] indicates that the "typical" particle does not lose enough energy to move from one bin to another during the typical observation period.

c) The spiral character of the interplanetary field was partially taken into account by assuming that the observations at earth correspond to r = 1.15 AU, which is the path length along the spiral field for V = 400 km/sec. The spiral field and the corotation effect were also included by using the azimuthal function $Q(\gamma',t)$ defined by equations 5-15 and 5-17. The dependence of the longitude of the directly-connected field line on the solar wind velocity V was included as well. The solar angular velocity was defined as $\Omega = 2.69 \times 10^{-6}$ radians/sec, the value at the solar equator.

d) The particles were assumed to be injected as a δ-function in r, θ, and ϕ. Thus the cone half-angle was $\gamma_o = 0$ in all cases. The coordinates (λ_o,Φ_o) and time of injection for each event were defined precisely in terms of the parent flare identification summarized in Table IV-2. The radial position of injection was assumed to be the surface of the sun $r_s = 0.0047$ AU.

e) The solar wind velocity was set to the best estimate based on the ESSA data (see Section IV).

f) Thus the only free parameters for each fit were the diffusion coefficients κ_r and κ_θ, the boundary position L, and the arbitrary normalization A. An initial choice of L = 2.3 AU was made based on the fits made by Burlaga[10].

Because of the complicated nature of the flare profiles, a least-squares fitting technique could not be easily used. Instead, a simple but tedious optimization with respect to κ_r, κ_θ and A was made by eye for each profile.

2. Forman's Solution

An attempted fit to the 2 November 69 event profile using Forman's solution (equation 5-28) with $\kappa_r(r) = \kappa_o r$ is shown in Figure V-7. With L = 2.3 AU, her solution duplicates the decay profile using reasonable values of κ_r and κ_θ (evaluated at 1 AU), but cannot match the rapid rise observed. Forman has attributed the long rise time predicted by her solution to the simple boundary condition assumed at the origin and to the $\kappa_r \propto r$ dependence used[12]. As will be demonstrated next, the r-dependence assumed for κ_r inside 1 AU has a drastic effect on the time-to-maximum, for an obvious reason: early in the event the particles are peaked near the sun, the propagation is due almost entirely to diffusion, and the rate of particle transport is thus very sensitive to the near-sun value of κ_r. Concerning the boundary condition at the sun, Englade has recently used Burlaga's ADB model to study the effect of different boundary conditions at $r = r_s$[58]. He reports that the type of boundary condition assumed has surprisingly little effect on the profile observed at 1 AU.

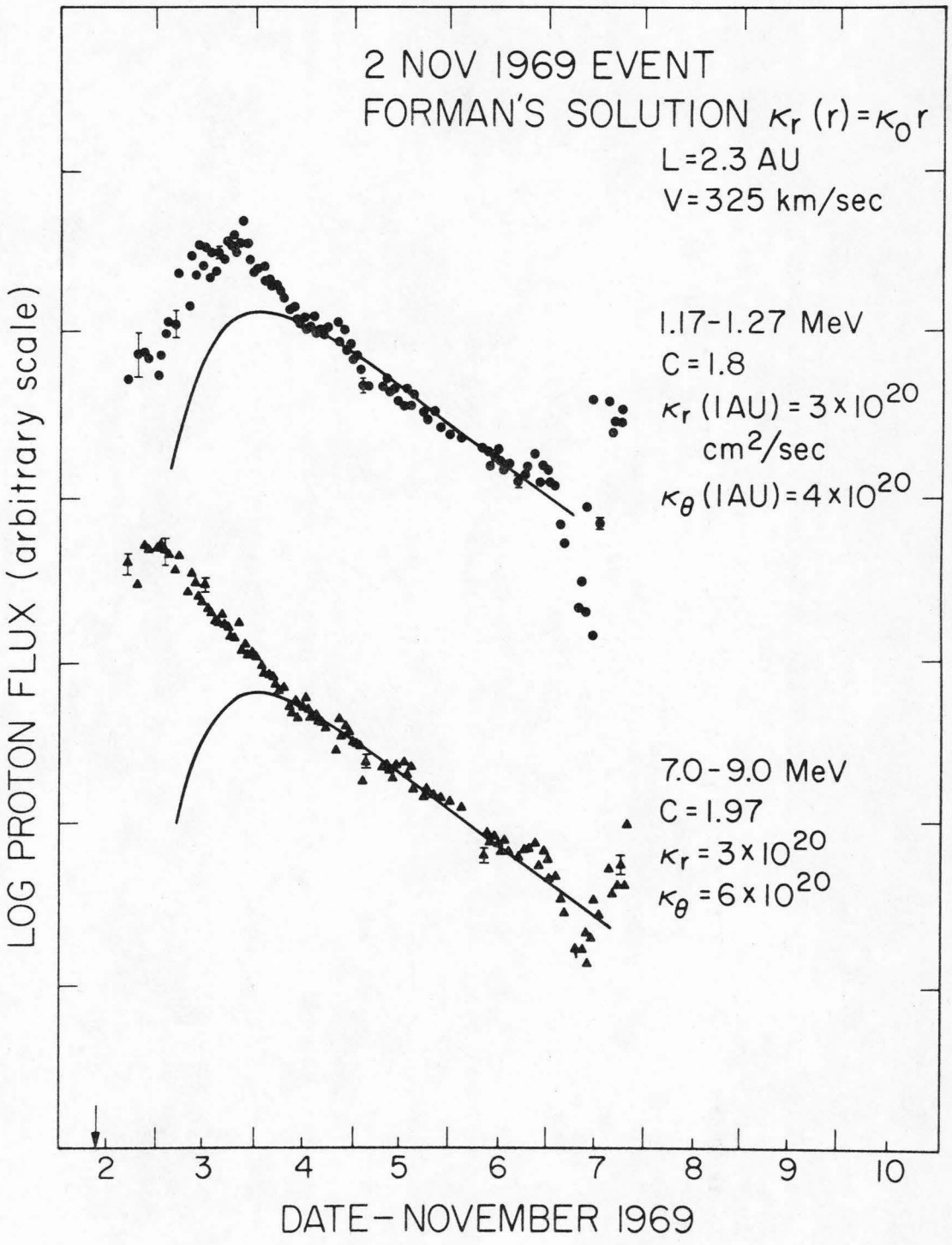

Figure V-7: Fits to the 2 November 1969 event using Forman's solution with L = 2.3 AU.

3. Fits Using the New Solution

The new solution developed in Section V-D can be described as identical to Forman's except that it assumes $\kappa_r(r)$ = constant. A preliminary attempt to fit all four flare events discussed in Section IV using L = 2.3 AU produced the following results:

a) The 30 Dec 69 event appears to belong to a completely different class than the other three events: its decay rate is twice as fast as the usual and is inversely correlated with energy (which is very atypical). Although the time-profile of this event can be fitted using the new solution, it will be omitted from the analysis here on the basis that it is not a flare-associated feature or at least not an example of the "classical" prompt flare event which this discussion is attempting to explain.

b) Some difficulty was encountered in fitting both the rise and decay rates of the 2 Nov and 31 Jan events. It was found that this small problem could be remedied by moving the boundary out to L = 2.7 AU.

Figures V-8 through V-10 show fits to the remaining three "classical" flare events using the new solution with L = 2.7 AU. With the value of L fixed, using only κ_r, κ_θ, and A as free parameters, the predictions of the new solution can be made to agree very well with the observed profiles of all three events at energies from ~1 MeV to ~70 MeV.

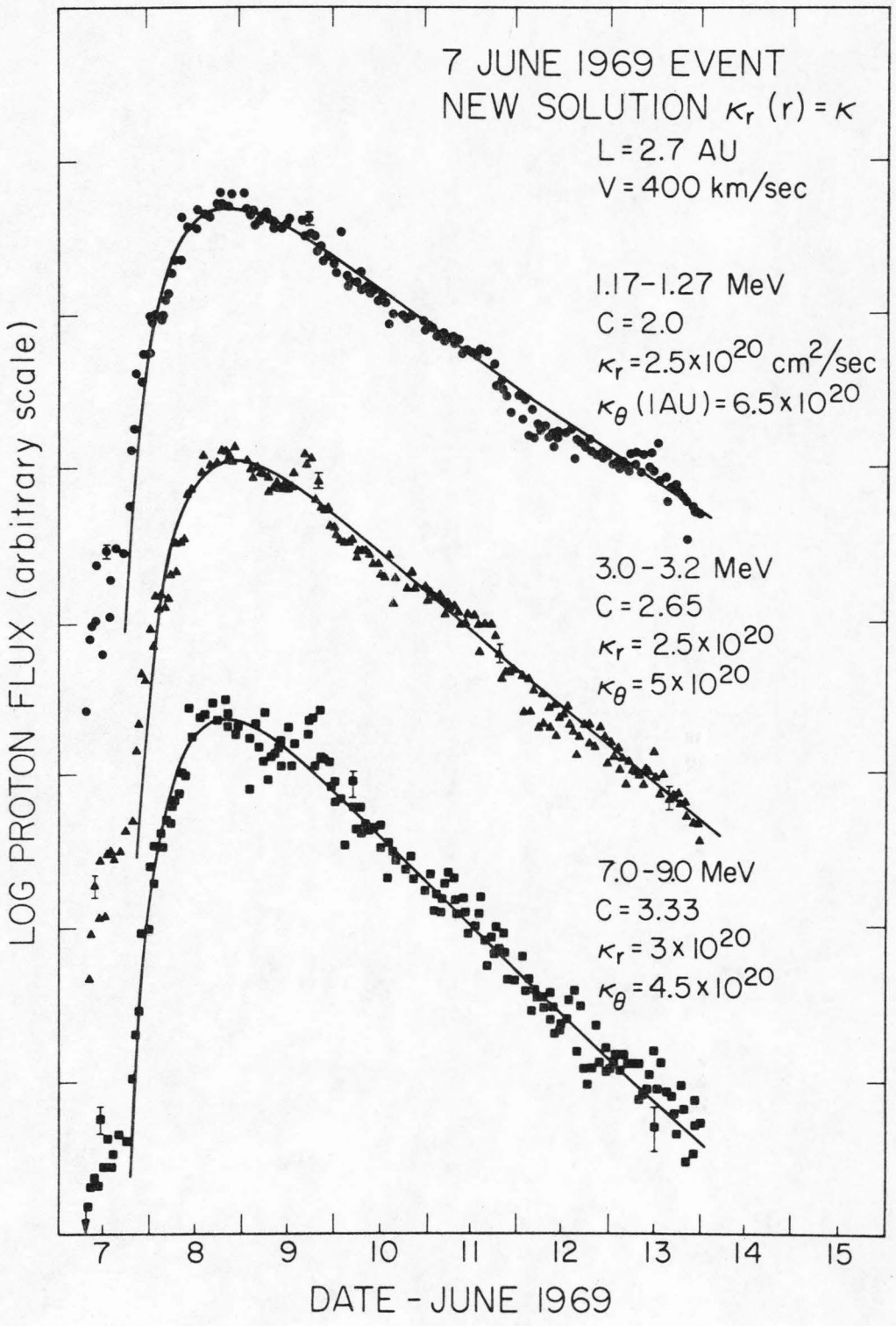

Figure V-8: Fits to the 7 June 1969 event using the new solution with L = 2.7 AU.

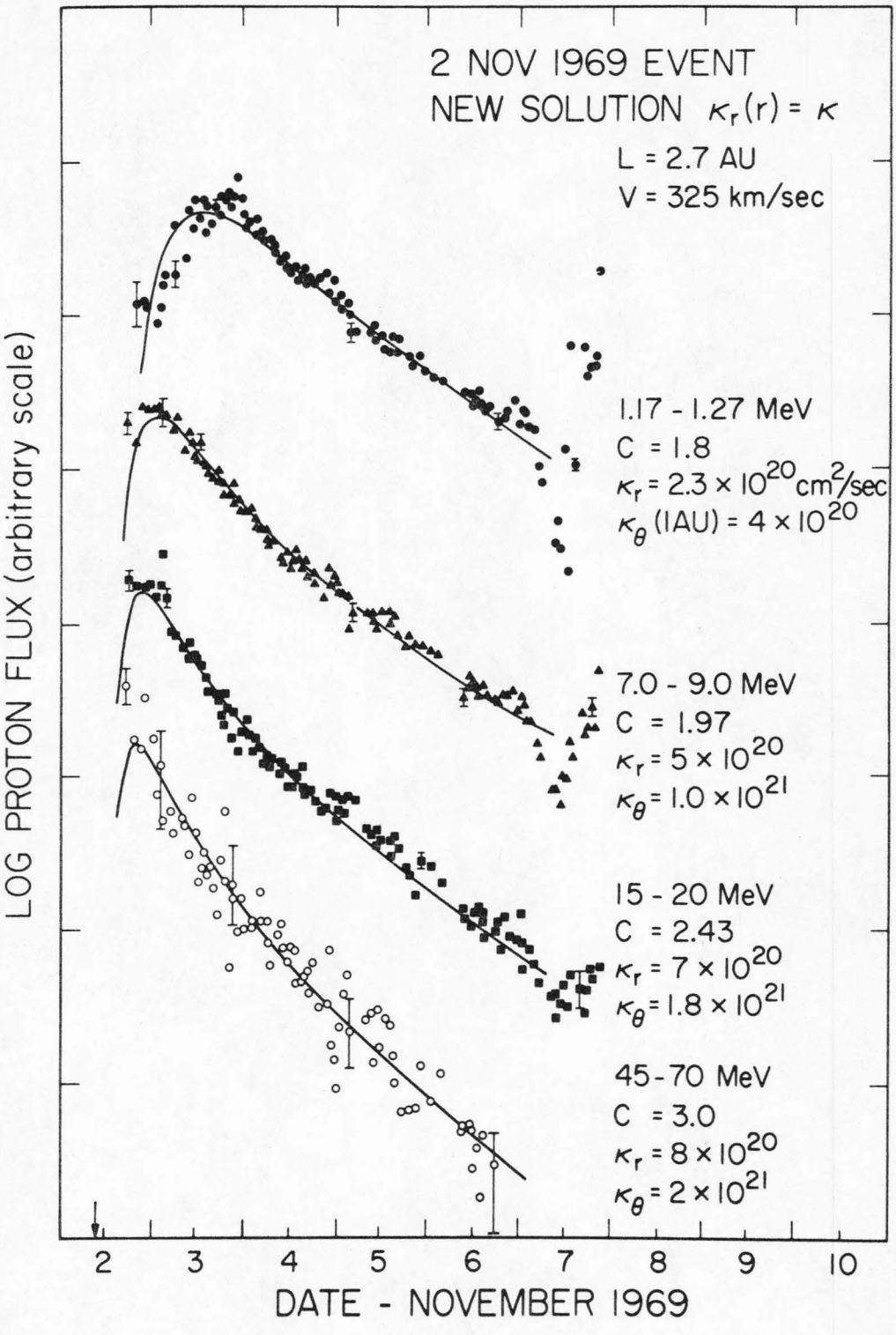

Figure V-9: Fits to the 2 November 1969 event using the new solution with L = 2.7 AU.

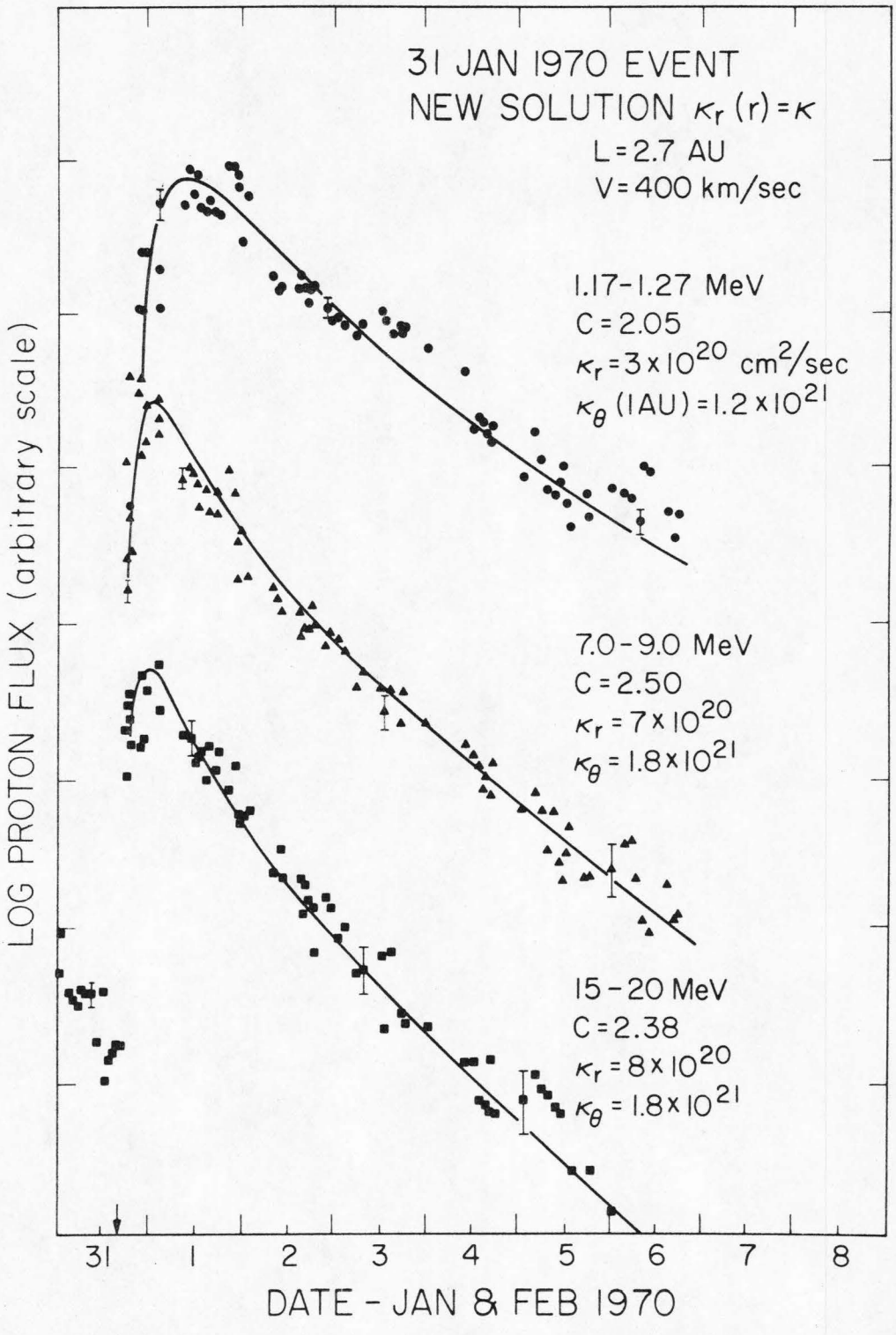

Figure V-10: Fits to the 31 January 1970 event using the new solution with L = 2.7 AU.

4. Evaluation

Figure V-11 summarizes the best-fit values of κ_r for all three flare events determined using the new solution with L = 2.7 AU. It is immediately apparent that the κ_r values agree well with each other and are also at least consistent with the low energy estimate for $\kappa_{\parallel}$ given by Jokipii and Coleman[38] (see Section V-B-2). The consistency between these three events is encouraging, especially since one of them (the 7 June event) was separated by ~100° in solar longitude from the foot of the near-earth field line, while the other two (2 Nov and 31 Jan) were "west-limb" or "directly-connected" events. It should be emphasized that the absolute values of κ_r needed to achieve reasonable fits depend on the boundary position L chosen. Thus the agreement within a factor of 3 with Jokipii's numbers is really better than could be expected. Note that the dependence of these κ_r values on energy T is not very strong below ~10 MeV, indicating that the built-in assumption that κ_r is independent of T is a reasonable approximation.

The value L = 2.7 AU should by no means be taken as a location for an actual physical shock transition in the solar wind. The repeated observation of exponential decay profiles seems to indicate that some kind of free escape region exists, but a sharp boundary is not necessary. Specifically, while the success of the new solution at explaining both the rise and decay times indicates that $\kappa_r(r)$ = constant is a better estimate of the r-dependence of κ_r inside 1 AU than is $\kappa_r(r) = \kappa_o r$, the results reported here yield no evidence that κ_r is constant

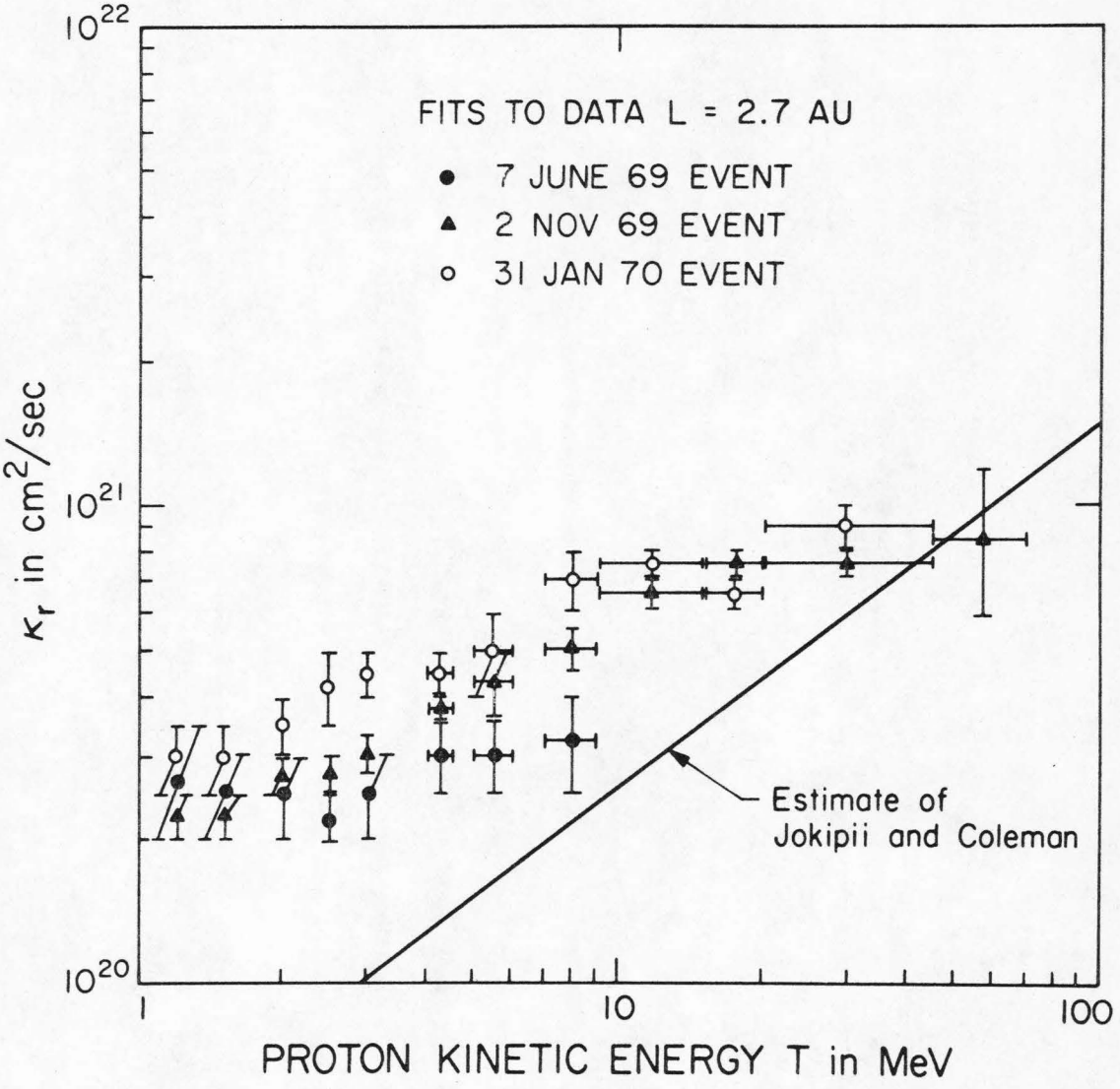

Figure V-11: The best-fit values of κ_r are plotted vs. proton energy T for all three flare events. The values were determined using the new solution with L = 2.7 AU. The estimate of Jokipii and Coleman based on Mariner IV field measurements is included for comparison (see Section V-B-2).

beyond 1 AU. Thus the physical significance of L = 2.7 AU depends on whether κ_r = constant is a good estimate of actual conditions between 1 AU and the boundary.

It is interesting to note that the best-fit values of κ_r(1 AU) obtained using Forman's solution are nearly identical to those obtained using $\kappa_r(r)$ = constant (compare Figures V-7 and V-9). One would expect that the decay rate at late times would depend on the average value of κ_r beyond 1 AU, since the majority of the particles are stored in this region. However, Forman's solution yields identical decay times with a $\kappa_r(r)$ that is everywhere beyond 1 AU greater than the κ_r of the new solution. The decay rate is thus not very sensitive to the r-dependence of κ_r, probably because the particle transport at low energies is dominated by convection at late times.

In contrast to the radial particle propagation described by the new solution, the azimuthal diffusion does not appear to be explained very well by the simple model used. Although the actual data have been fitted quite well (even for the 7 June event for which perpendicular diffusion is important), the best-fit values of κ_θ are not consistent from flare to flare and disagree with the estimates based on Mariner IV observations. Worst of all, the κ_θ value is in almost every case larger than the corresponding κ_r, which is in disagreement with the observations of McCracken et al.[15] as well as with the calculations of Jokipii[1].

McCracken et al.[15] have presented the picture that the particles spread rapidly in longitude near the sun, and at the same time begin to

move outward along the field lines. Later in the event, when the near-sun diffusion region has been depleted, the particles assume an azimuthal distribution in interplanetary space which has a shape defined by the specifics of the near-sun propagation, but which is smoothed out very slowly because $\kappa_\perp$ is small in interplanetary space.

This explanation, which seems to be a reasonable one, is completely different than the simple point-injection and 2-dimensional diffusion used here. It was found, however, that the solution for the directly-connected events was relatively insensitive to the value of κ_θ, simply because the azimuthal part of the solution doesn't play a very important role in determining the profile. The large values of κ_θ determined for the events of 2 Nov and 31 Jan can thus be taken as indications that the azimuthal part of the solution can (and should) really be ignored completely whenever the parent flare is close to the line-of-force passing through the earth.

However, for the 7 June 1969 event, the longitudinal solution cannot be neglected. Nor can the rise profile for this event be explained away as the effect of a rigid azimuthal distribution corotating by the earth: the gradient in longitude needed to explain the rise is much steeper than that observed by McCracken et al.[15] In fact, the effect of corotation on the event profile observed at earth seems to be small, contrary to the claim of McCracken et al. that the decay rate observed should depend critically on whether the earth is corotating toward or away from the peak of the longitudinal distribution. Based on McCracken's observations of the longitudinal

gradient $dn/d\theta \approx n/40^{o}$ [15], one finds that corotation will superimpose a ±5 hour effect on a typical decay constant of τ_{DEC} = 20 hours. Also, in our admittedly small sample of flare data, no correlation of decay time with corotation direction is evident -- in fact the measured decay times are remarkably similar for east and west limb events (compare 7 June with 2 Nov and 31 Jan).

It seems that the slow rise of the June event must be due to the finite evolution time of the near-sun longitudinal distribution. It is then not such a surprise that our simple $Q(\theta,\phi,t)$ function produces a profile which, when combined with the radial dependence $R(r,t)$, matches the actual data quite well: although our azimuthal solution was intended to describe a 2-dimensional diffusion process in interplanetary space, it can just as well describe a similar random walk within a narrow region near the sun. The values of κ_{θ} determined by fitting the 7 June event can thus be taken as an indication of the rate of near-sun propagation, rather than as a measure of $\kappa_{\perp}$ near the earth.

Finally, the results of the fitting procedure are consistent with the assumption that adiabatic deceleration is the only energy-change process operative. However, this question can only be answered by comparing the predictions of the new model directly with experimental evidence for the energy-change effect, such as that reported by Murray et al.[31] This energy-change problem will be discussed in a later section.

F. Vector Particle Anisotropy

Measurements of the solar flare proton flux in interplanetary space have shown that this flux is not completely isotropic, and that the anisotropy is most pronounced early in a flare event[15,26]. It is of interest to compare these observations with the predictions of the new solution.

1. Definition

We first define the following quantities:

$$j(\theta,\phi)d\Omega = \begin{pmatrix}\text{particle flux directed from a} \\ \text{given solid angle increment } d\Omega\end{pmatrix}$$

$$n(\theta,\phi)d\Omega = \frac{j(\theta,\phi)d\Omega}{w} = \begin{pmatrix}\text{contribution to the density from} \\ \text{a solid angle increment } d\Omega\end{pmatrix}$$

$$w = \text{particle velocity}$$

When the particle flux $j(\theta,\phi)$ is nearly isotropic, it can be written as

$$j(\theta,\phi) = I_o(1 + \xi\cos\theta) \tag{5-47}$$

where ξ is the particle anisotropy.

The omnidirectional flux is then simply

$$\left\langle j(\theta,\phi)\right\rangle_\Omega = \frac{1}{4\pi}\int d\Omega\, j(\theta,\phi) = I_o \tag{5-48}$$

and the net flux through a surface is identical to the particle current $\vec{S}$ discussed in Section V-D-2:

$$S = \int d\Omega\, j(\theta,\phi)\, \cos\theta = \int d\Omega\, I_o(1 + \xi\cos\theta)\, \cos\theta$$
$$= \frac{4\pi}{3} I_o \xi \tag{5-49}$$

The average density n, which is the quantity predicted by the solution, can be written as

$$n = \int d\Omega\, n(\theta,\phi) = \frac{4\pi I_o}{w} \tag{5-50}$$

Finally, the *vector* anisotropy $\vec{\xi}$ can be defined in terms of the density n and the previously discussed particle current S:

$$\vec{\xi} = \frac{3\vec{S}}{nw} = \frac{3}{w}\left(C\vec{V} - \frac{1}{n}\underline{\underline{\kappa}} \cdot \nabla n\right) \tag{5-51}$$

The magnitude of the anisotropy can easily be related to the maximum and minimum values of $j(\theta,\phi)$ measured with a cosmic ray telescope:

$$|\vec{\xi}| = \frac{j_{max} - j_{min}}{j_{max} + j_{min}} \tag{5-52}$$

2. Observations

No anisotropy measurements can be made from the OGO-6 spacecraft, because its orbit lies within the magnetosphere. We must therefore rely on measurements such as the Pioneer observations reported by McCracken et al.[15,26]. For 7 - 20 MeV protons at ~1 AU, they observe a large 25-50% anisotropy early in a solar event which is directed roughly along the field (from ~45°W). This strong initial anisotropy then changes in magnitude and direction so that at late times it has a strength of about 5-10% directed approximately

perpendicular to the field (from $\sim 45^{o}$E). The details of their anisotropy observations vary greatly from event-to-event, but the general features just described are nearly always present.

3. Anisotropy Predicted by the New Solution

At this point, the following conclusions have been drawn concerning the new solution and its ability to predict the features of solar flare events:

a) By taking the magnetic field as radial, and thus equating $\kappa_r = \kappa$ and $\kappa_\theta = \kappa_\phi = \kappa$, reasonable fits to the 1-20 MeV proton data have been achieved using L $\simeq$ 2.3 - 2.7 AU, C = 1.5 - 3.5, and $\kappa_r = 2 \times 10^{20}$ to 1×10^{21} cm^2/sec (all reasonable values).

b) The azimuthal diffusion is probably only significant in a small region near the sun, and as suggested by the observations of McCracken et al.[15], $\kappa_\theta << \kappa_r$ in interplanetary space. Except when the near-sun longitudinal diffusion process affects the event rise profile (as in the case of the 7 June 69 event), the azimuthal part of the solution is best ignored completely ($\kappa_\theta = \kappa_\phi = 0$).

Ng and Gleeson[13,14] have used another interpretation of the assumption that the diffusion tensor is diagonal in a frame aligned with the radial direction. Instead of neglecting the spiral nature of the field, they have completely neglected all perpendicular diffusion ($\kappa_\perp = 0$) and azimuthal gradients and have taken $\kappa_r(r) = \kappa_o r = \kappa_{\parallel}(r)\cos^2\psi$ where $\psi = \tan^{-1}\Omega r/V$ is the spiral angle. Thus their rather special form of $\kappa_{\parallel}(r) = \kappa_o r/\cos^2\psi$ is simply the r-dependence needed to produce $\kappa_r(r) = \kappa_o r$.

The nature of this assumption by Ng and Gleeson can be seen more clearly by writing the diffusion tensor in a reference frame aligned with the B-field,

$$\kappa_{ij} = \begin{pmatrix} \kappa_{\parallel} & 0 & 0 \\ 0 & \kappa_{\perp} & 0 \\ 0 & 0 & \kappa_{\perp} \end{pmatrix} \tag{5-53}$$

and then transforming it into a frame aligned with the radial direction

$$\kappa'_{ij} = \begin{pmatrix} \kappa_{\parallel}c^2 + \kappa_{\perp}s^2 & (\kappa_{\parallel} - \kappa_{\perp})cs & 0 \\ (\kappa_{\parallel} - \kappa_{\perp})cs & \kappa_{\parallel}s^2 + \kappa_{\perp}c^2 & 0 \\ 0 & 0 & \kappa_{\perp} \end{pmatrix} \tag{5-54}$$

where $c = \cos\psi$ and $s = \sin\psi$. Even if one sets $\kappa_{\perp} = 0$, the tensor is still non-diagonal due to diffusion in ϕ caused by $\kappa_{\parallel}$. Ng and Gleeson have neglected all the elements of the tensor except $\kappa_{rr} = \kappa_r = \kappa_{\parallel}\cos^2\psi$ and have thus used purely radial diffusion to describe diffusion along the spiral field.

This interpretation, which is only an approximation of the actual situation, can easily be applied to the solution developed in this dissertation. The r-dependence for $\kappa_{\parallel}$ becomes $\kappa_{\parallel}(r) = \kappa/\cos^2\psi$, and the gradient $\vec{\nabla}n = \cos\psi(\partial n/\partial r)$. Then we can write separate expressions for the diffusive and convective parts of the vector anisotropy:

$$\vec{\xi}_{\kappa} = -\frac{3}{w}\frac{\kappa}{R}\cos\psi\,\frac{\partial R}{\partial r}\,\hat{e}_B = -\frac{3}{w}\frac{\kappa}{\cos\psi}\,\frac{\partial R}{\partial r}\hat{e}_B \tag{5-55}$$

$$\vec{\xi}_V = \frac{3}{w} C V \hat{e}_r \qquad (5\text{-}56)$$

where $R(r,t)$ is the radial part of the solution, $\hat{e}_B$ is the unit vector directed outward along the spiral field, and $\hat{e}_r$ is the radial unit vector. The vectors $\hat{e}_r$ and $\hat{e}_B$ meet at an angle $\psi \simeq 48^o$ at 1 AU, and the resultant $\vec{\xi}$ has a direction which depends on the relative magnitudes $|\xi_V|$ and $|\xi_\kappa|$.

The calculated magnitudes of ξ_κ and ξ_V as a function of time are shown in Figure V-12 for several values of κ_r. Note that ξ_V is independent of time, while ξ_κ decreases in magnitude and eventually reaches an equilibrium value which is negative for typical values of κ_r.

The vector combination of these separate components is shown in Figure V-13, which depicts the evolution of $\vec{\xi}$ in one-day steps. A typical observation borrowed from McCracken et al.[15] is shown for comparison. The parameter values chosen are typical for ~10 MeV protons, and the agreement with the observations of McCracken et al. is quite good: $\vec{\xi}$ decreases in magnitude and changes direction from the west to the east. The strength of the anisotropy predicted at late times is ~3-8% (depending on the values of V, κ_r, and C chosen), a value which is in good agreement with the McCracken observations.

Figures V-5 and V-6 make it obvious why the anisotropy observed at 1 AU is directed from the east at late times. The typical equilibrium particle distribution has a peak situated beyond 1 AU. The diffusive anisotropy at 1 AU is thus directed inward along the field,

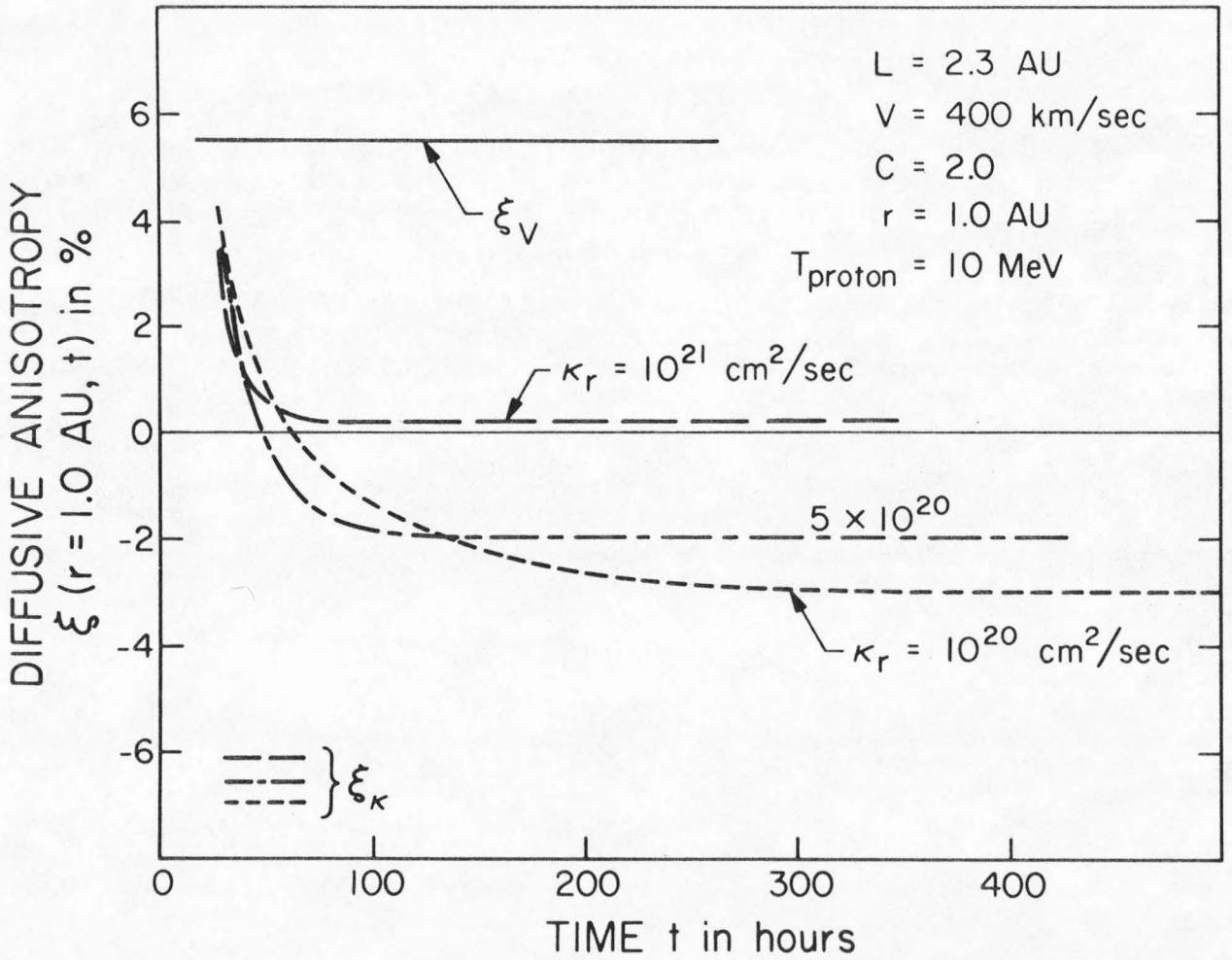

Figure V-12: The magnitudes of the diffusive and convective components of the anisotropy ξ_κ and ξ_V predicted by the new solution are plotted vs. time for various values of κ_r. Note that ξ_V is independent of time and of κ_r.

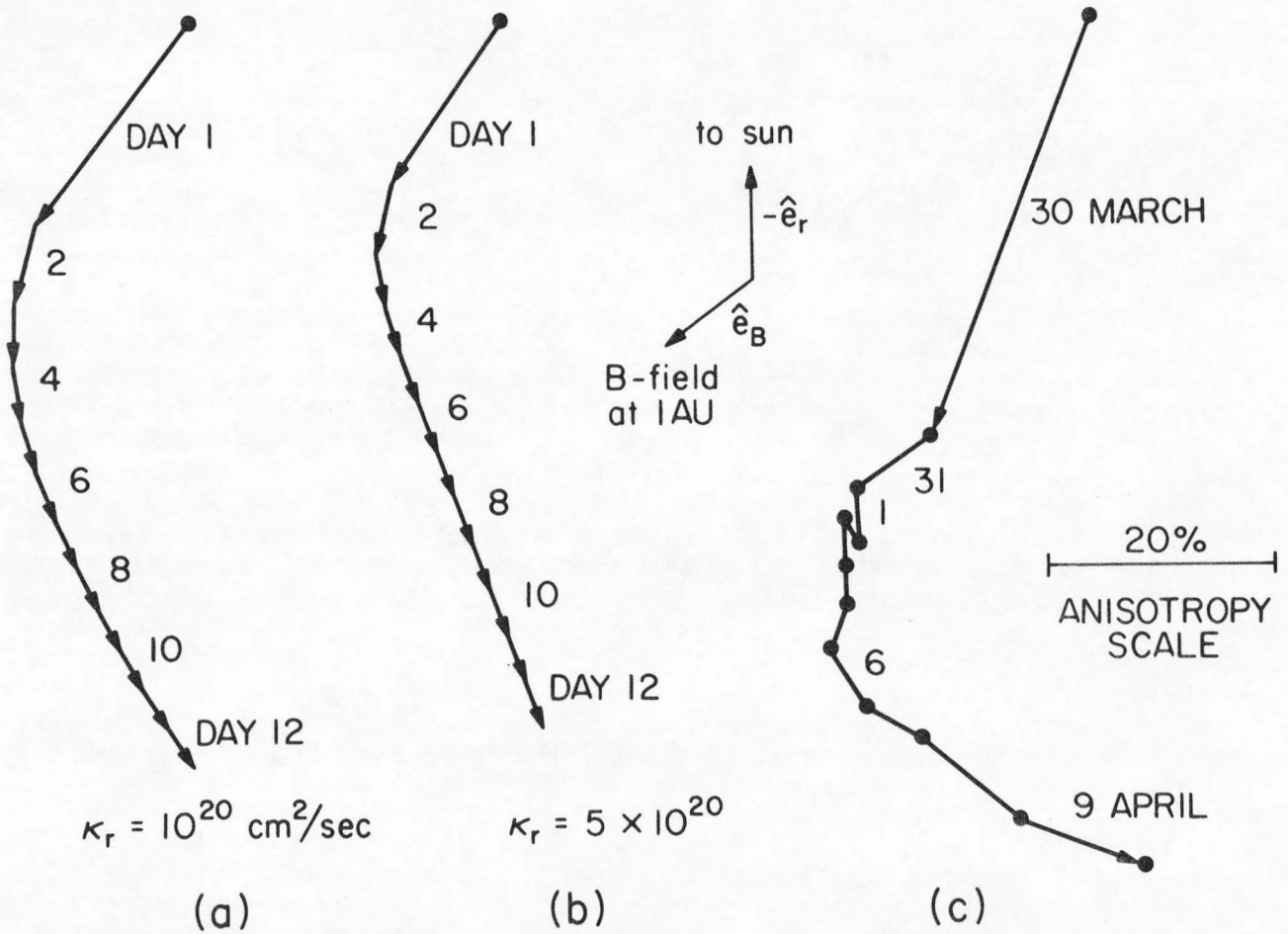

Figure V-13: A vector diagram of the time-evolution of the vector anisotropy at 1-day intervals. a) and b) are the predictions of the new solution using L = 2.3 AU, V = 400 km/sec, C = 2.0, r = 1.0 AU, and T_{proton} = 10 MeV. c) is a typical Pioneer 8 observation as reported by McCracken et al.[15] for 7.5-21.5 MeV protons during 30 March to 9 April, 1969.

and produces an eastward anisotropy when combined with the outward radial convective current. At early times, the large density gradient produces a strong outward diffusive anisotropy directed along the field. This is exactly the description used by McCracken et al. to explain the features of their anisotropy observations.[15].

G. The Energy-Change Effect

1. Statement of the Problem

Recently, Murray et al. reported a direct observation of the energy-change effect during the 7 June 1969 solar flare event[31]. Their observation consisted of mapping the time-evolution of a "kink" or "knee" in the proton differential energy spectrum. They found that this kink moved to lower energies at a rate characterized by an exponential time constant $\tau_{KINK} = 210 \pm 10$ hours, a result which appears to be at variance with the energy-change rate at 1 AU predicted assuming only adiabatic deceleration. They interpreted this as an indication that an acceleration process may be competing with the adiabatic deceleration and thus producing a slower energy-change rate.

In a companion paper, Jokipii suggested that solar flare particles could be energized via second-order Fermi acceleration by hydromagnetic waves travelling in the interplanetary medium[44]. He presents an estimate of the strength of the effect, and concludes that this Fermi acceleration may well be fast enough to offset a sizable fraction of the adiabatic deceleration.

Subsequent discussions of this problem have pointed out that the decay rate in energy of a spectral feature depends not only on whether or not a competing acceleration process is present, but also on the spatial distribution of particles with respect to the observer[45,46,47,48,61]. Based on an earlier solution by Forman[62], which ignored diffusion and radial gradients, Murray et al. compared the adiabatic time constant *at 1 AU* given by $\tau_E(1\ \text{AU}) = 3r/4V =$ 78 hours (for V = 400 km/sec), with the measured $\tau_{KINK} \tilde{}$ 210 hours. This approach is not generally correct when solar particles are diffusing over a large region of interplanetary space. The time constant $\tau_E(r) \propto r$ characterizes the instantaneous energy-loss rate experienced by a particle at position r in a frame moving with the solar wind. Thus, especially during the decay phase, a typical solar flare particle undergoes a random walk in position and thereby samples many different rates of energy-loss. One might then expect the energy-change rate to be described by the $\tau_E(r)$ at the position where the "average" particle spends its time, rather than by the $\tau_E(1\ \text{AU})$ at the position of the observer. This simple characterization will be investigated more rigorously.

2. Observations

Thus far two "well-behaved" flare events have been observed aboard OGO-6 which have a clearly-defined kink in their decay-phase spectra at ~3 MeV: the events of 7 June 1969 and 31 Jan 1970 (see Figure IV-2). The following procedure, similar to that employed by Murray et al.[31], has been used to investigate the energy vs. time

characteristics of these spectral features:

a) Separate power laws were fitted above and below the "kink" to each differential density spectrum over a ~3 day period. Both the slopes (γ_1 and γ_2), and the intensities (n_1 and n_2) were used as free parameters.

b) The average power law slopes above and below the kink (respectively $\langle \gamma_2 \rangle$ and $\langle \gamma_1 \rangle$) were determined from plots of γ_1 γ_2 vs. time. For both events these slopes were found to have negligible time-dependence.

c) The spectra were then re-fitted using the average values $\langle \gamma_1 \rangle$ and $\langle \gamma_2 \rangle$ with only n_1 and n_2 as free parameters.

d) A value of the intersection point $E_{INT}(t)$ of the power laws $n_1 T^{-\gamma_1}$ and $n_2 T^{-\gamma_2}$ was determined for each spectrum fitted.

Figure V-14 shows a plot of $E_{INT}(t)$ vs. t for both events. The open circles represent points which were deleted from the 31 Jan 1970 decay because of an energy-correlated particle increase which occurred between ~0700 UT on 3 Feb 1970 and ~1400 UT on 4 Feb 1970. Because of this puzzling feature, which is evident in Figure IV-1-d, the evidence for an energy-change process is not as unambiguous for the 31 Jan event as for the 7 June event. The large error bars for the 31 Jan data reflect the goodness-of-fit achieved and are the result of poor counting statistics. In each case there is definite evidence for an energy-loss effect, and a least-squares exponential fit yields τ_{KINK}(7 June) = 182 $\pm$ 6 hours and τ_{KINK}(31 Jan) = 160 $\pm$ 20 hours. The disagreement with the τ_{KINK}(7 June) of Murray et al. is a systematic effect due to the

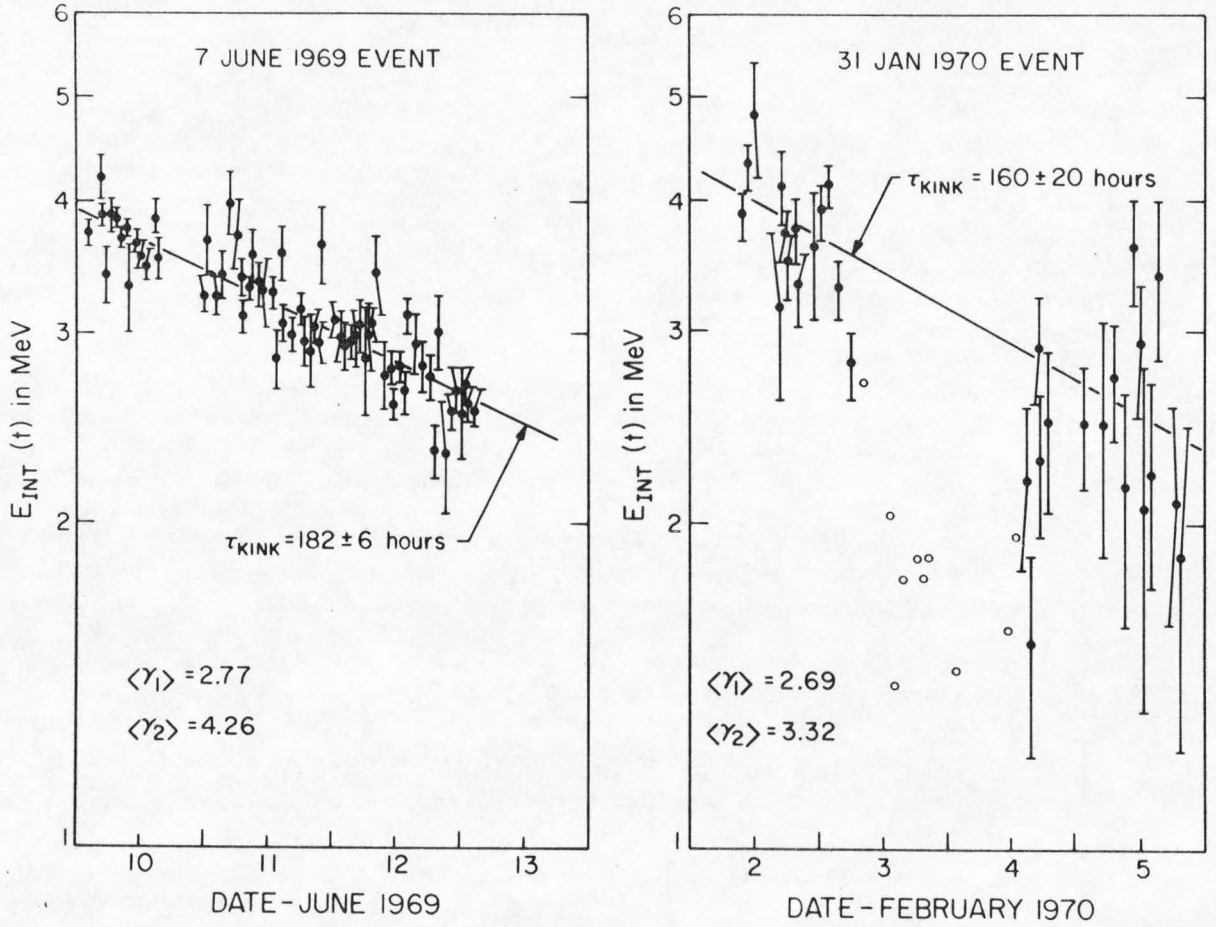

Figure V-14: The time-dependence of the intersection energy $E_{INT}(t)$ is shown for a period during the decay phase of the 7 June 1969 and 31 Jan 1970 flare events. This intersection energy was defined by fitting separate power laws with fixed slopes $\langle\gamma_2\rangle$ and $\langle\gamma_1\rangle$ above and below a kink at ~3 MeV. The open circles represent points which were deleted because of an unexplained energy-dependent particle increase which occurred during the decay of the 31 Jan event. The dashed lines are least-squares exponential fits.

specific choice made for $\langle \gamma_1 \rangle$ and $\langle \gamma_2 \rangle$, and the difference of ~28 ± 12 hours can be taken as an indication of this systematic uncertainty.

The fact that the power law asymptotes γ_1 and γ_2 as well as the "kink" are stable with time is an important observation in itself: it indicates that the energy "smearing" caused by the particle random walk in position is not so great as to erase a spectral feature within the ~3 day period needed to define the energy decay rate.

3. Energy-Change Predicted by the New Solution

Although considerable discussion has been waged concerning the energy-change process for solar flare particles, no prediction has yet been made using any model which can be compared directly to the available energy-decay observations of a convex-shaped spectral feature. Palmer[46] and Urch and Gleeson[47] have carried out calculations concerning the way in which an energy "spike" propagates. Gleeson and Ng[61], on the other hand, have applied their recent flare propagation solution[13] directly to the observations of Murray et al. They make the simple geometrical calculation that a *concave* power law kink (steeper at lower energies) defined by

$$n(T) = n_1 T^{-\gamma_1} + n_2 T^{-\gamma_2} \tag{5-57}$$

will move to lower energies at a rate defined by

$$\tau_{KINK} = \frac{\tau_1 \tau_2 (\gamma_2 - \gamma_1)}{(\tau_1 - \tau_2)} \tag{5-58}$$

where τ_1 is the decay constant associated with slope γ_1, etc.

Unfortunately, energy spikes and concave spectral kinks are rarely observed, and it is not immediately obvious how the evolution of such features can be related to the existing observations of a convex kink. For this reason, an attempt has been undertaken to predict the evolution of a convex kink using the new solution. The method is straightforward (see equation 5-38) but difficult to implement. At late times, the new solution predicts that a pure power law spectrum defined by slope γ will decay exponentially at τ_{DEC}. Any initial spectrum S(T) that can be written as a superposition of power laws

$$S(T) = \sum_i A_i T^{-\gamma_i} \qquad (5\text{-}59)$$

can then be propagated in time by

$$n(T,t) = \sum_i A_i T^{-\gamma_i} e^{-t/\tau_i} \qquad (5\text{-}60)$$

where the one-to-one correspondence between each γ_i and τ_i involves the calculation of the first Coulomb wave function eigenvalue and depends on τ_E, L, V, and κ_r. With some difficulty, a set of A_i's and γ_i's have been found which, when superimposed, produce a convex density spectrum S(T) with power law asymptotes of $\gamma_1 = 2$ and $\gamma_2 = 4$ above and below 3 MeV. These coefficients as well as a representative set of τ_i values are listed in Table V-2.

Figure V-15 shows the S(T) spectrum thus generated and also the way it evolves over a 200 hour period using typical values of the parameters. Several results are evident:

a) The S(T) generated is a good approximation to the observed

TABLE V-2

Power Law Superposition of a Density Spectrum
with a Convex Kink

assuming L = 2.3 AU
V = 400 km/sec
$\kappa_r = 3 \times 10^{20}$ cm^2/sec
τ_E(1 AU) = 78 hours

i	γ_i	A_i cm^{-3}	$C_i = \frac{2\gamma_i+1}{3}$	τ_i hrs
1	1.75	3.8133	1.50	31.88
2	2.00	-29.128	1.67	29.43
3	2.25	0.3227	1.83	27.38
4	2.50	561.42	2.00	25.62
5	2.75	-1767.9	2.17	24.10
6	3.00	1495.4	2.33	22.77
7	3.25	909.92	2.50	21.59
8	3.50	-954.86	2.67	20.54
9	3.75	-0.4838	2.83	19.60
10	4.00	-872.78	3.00	18.75
11	4.25	711.74	3.17	17.98
12	4.50	177.88	3.33	17.28
13	4.75	-115.51	3.50	16.63
14	5.00	-2.9039	3.67	16.03
15	5.25	-58.594	3.83	15.48
16	5.50	26.527	4.00	14.97

Figure V-15

An initial spectrum with a convex kink at ~3 MeV and power law asymptotes of $\gamma_1 = 2$ and $\gamma_2 = 4$ is shown. This spectrum $S(T) = \sum A_i T^{-\gamma_i}$ was generated by superimposing 16 separate power laws. The time-evolution of this input spectrum was calculated by assigning (via the new solution) a separate decay time constant τ_i to each power law element of S(T). For the parameter values chosen, the spectral shape is reasonably stable over an ~8 day period, and the "kink" moves exponentially to lower energies at a rate characterized by $\tau_{KINK} \simeq 106$ hours. The power law slope $\gamma(T)$ of the spectra are shown to emphasize the kink movement and to illustrate the slight rounding effect which occurs.

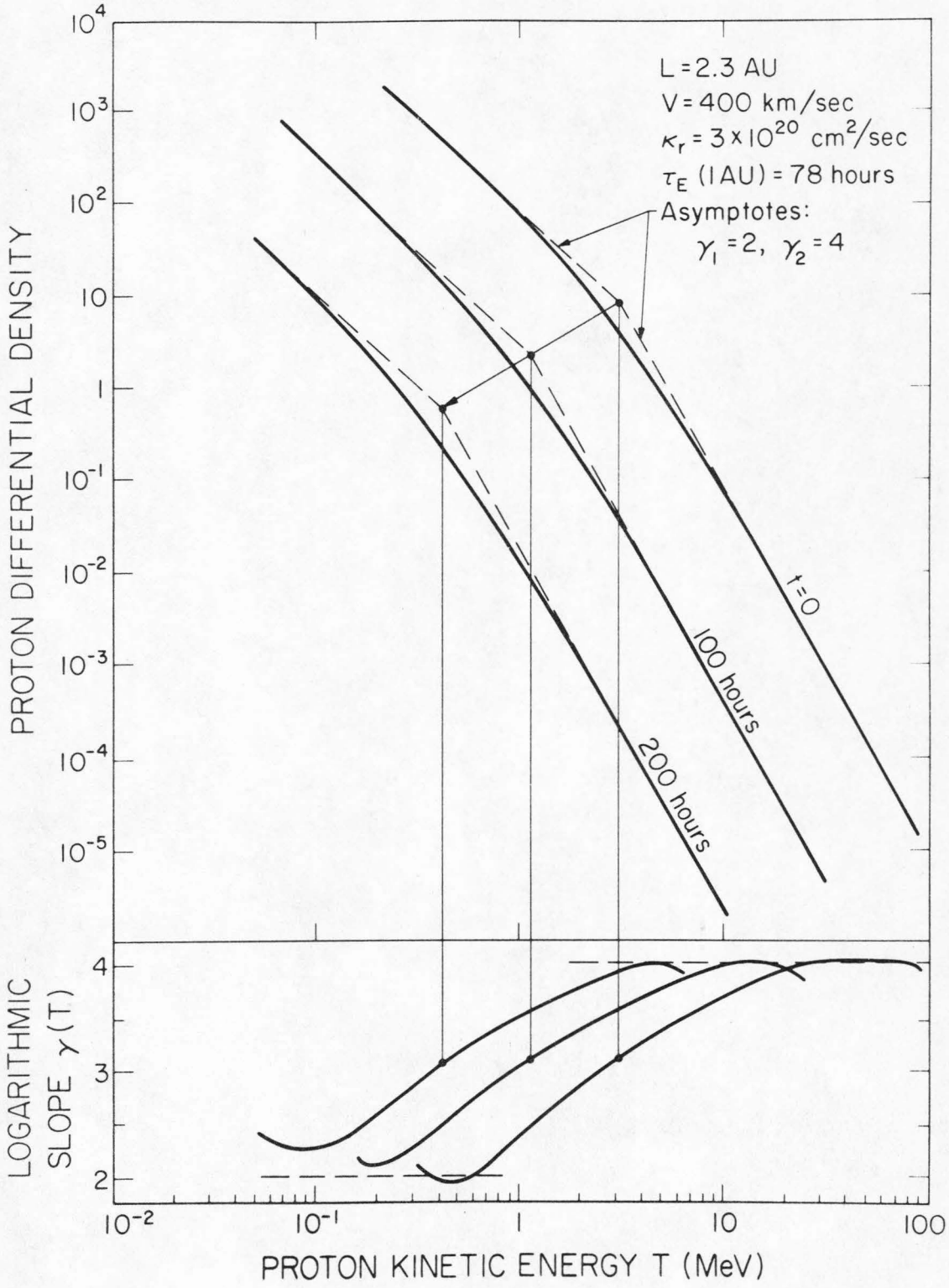
L = 2.3 AU
V = 400 km/sec
$\kappa_r = 3 \times 10^{20}$ cm^2/sec
τ_E (1 AU) = 78 hours
Asymptotes:
$\gamma_1 = 2$, $\gamma_2 = 4$
t=0
100 hours
200 hours
PROTON DIFFERENTIAL DENSITY
LOGARITHMIC SLOPE γ(T)
PROTON KINETIC ENERGY T (MeV)

spectra for 7 June 69 and 31 Jan 70.

b) The spectrum decays both in density *and* energy but retains retains its shape over a long (~8 day) period.

c) There is some "rounding" of the kink -- a result expected due to the particle random walk.

d) The kink decays at $\tau_{KINK} = 106 \pm 4$ hours for this choice of parameters -- a value still in disagreement with the observations.

The assumption that κ_r is independent of energy T (built into the new solution) must be discussed carefully when making predictions concerning the energy-change process. A strong dependence of κ_r on T would affect the time-evolution of the spectrum and make the model inapplicable. The κ_r energy dependence is in fact relatively weak: the best-fit values of κ_r for a given solar flare vary by only about a factor of 2 in the interval from 1 to 10 MeV (see Figure V-11). As will be shown in Figure V-17, the dependence of τ_{KINK} on κ_r is also weak, another indication that an energy-independent κ_r is a reasonable approximation.

The application of the formula of Gleeson and Ng using the asymptotes $\gamma_1 = 2$ and $\gamma_2 = 4$ yields a similar result:

$$\tau_{KINK} = \frac{(29.43h)(18.75h)(4 - 2)}{(29.43h - 18.75h)} = 103 \text{ hours}$$

Thus, even though this convex spectrum cannot be written as the superposition of two power laws (as in equation 5-57), the rate of kink

movement can be predicted by considering the independent evolution of the power law asymptotes using equation 5-58.

A glance at Figure V-5 shows that for V = 400 km/sec and $\kappa_r \simeq 3 \times 10^{20} cm^2/sec$, the particle distribution is peaked at r ≃ 1.4 AU and thus the "average" particle should lose energy at $\tau_E(1.4\ AU) \simeq$ 109 hours, in agreement with the more exact analysis just completed.

Further investigation has shown that the value of τ_{KINK} is relatively insensitive to the choice of the asymptotes γ_1 and γ_2. The complete power law superposition technique was used to generate a different convex spectrum with asymptotes of 2.6 and 4.2, a more accurate approximation to the 7 June 1969 spectrum. This kink was found to propagate at the same rate as the kink defined by $\gamma_1 = 2$ and $\gamma_2 = 4$. In addition, the simple formula (equation 5-58) was used to investigate the dependence of τ_{KINK} on γ_1 and $\gamma_2 = \gamma_1 + \Delta\gamma$ in more detail. Figure V-16 shows that τ_{KINK} varies by only ~10% over the entire range of reasonable values for the power law slope. One would then conclude that any spectrum, as long as it contains no very sharp features, will decay in energy at rate close to $(\tau_{KINK})^{-1}$ independent of shape.

The dependence of τ_{KINK} on V, L, κ_r and τ_E is explored in Figures V-17 and V-18 using both the simple formula and the power law superposition. The agreement between these two methods of calculating τ_{KINK} is almost exact. Increasing the distance to the boundary L decreases the energy-loss rate because the particles on the average spend their time further from the sun and thus experience a larger $\tau_E(r)$. Increasing the solar wind velocity also increases the distance to the peak in

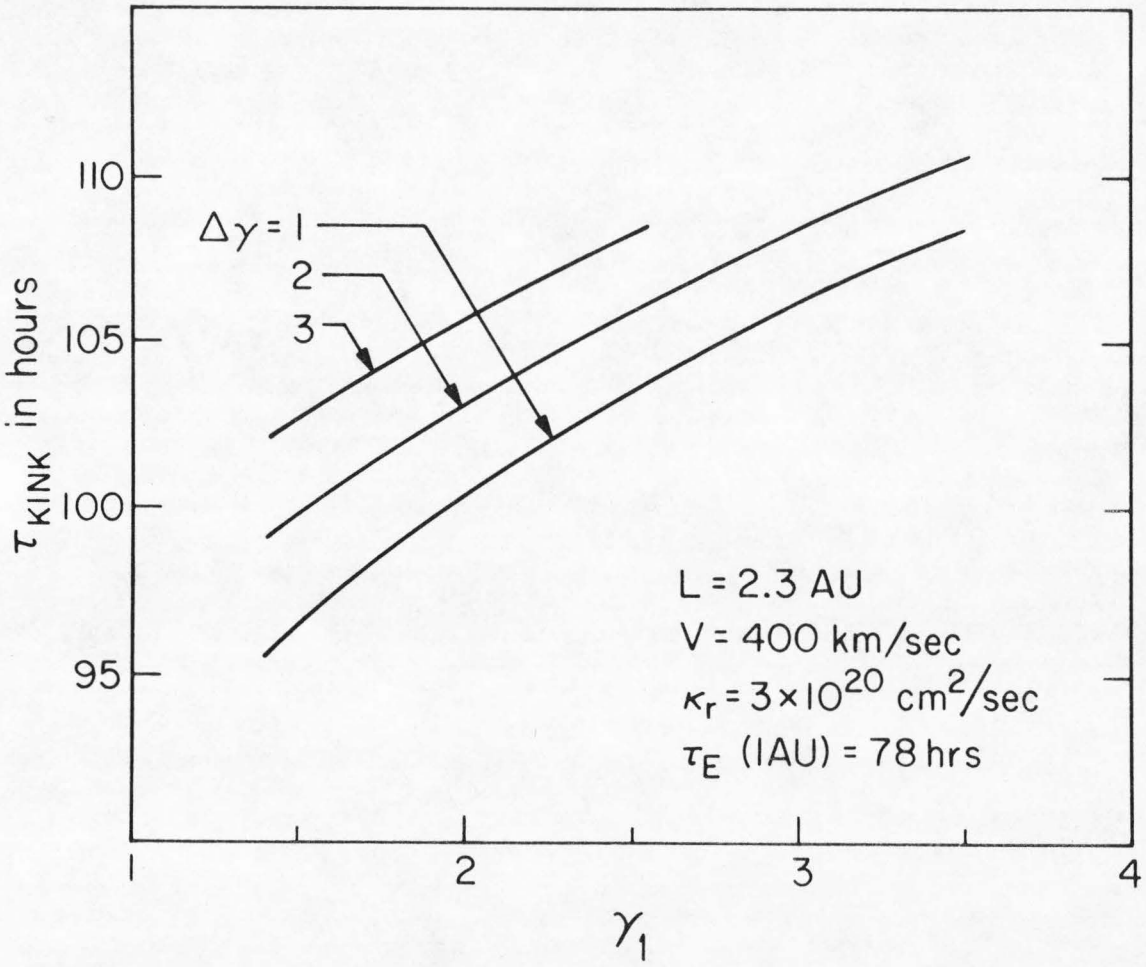

Figure V-16: The dependence of τ_{KINK} as calculated by the simple formula of Gleeson and Ng is shown as a function of the power law asymptotes γ_1 and $\gamma_2 = \gamma_1 + \Delta\gamma$. The conclusion is that the value of τ_{KINK} is relatively insensitive to the spectral shape used.

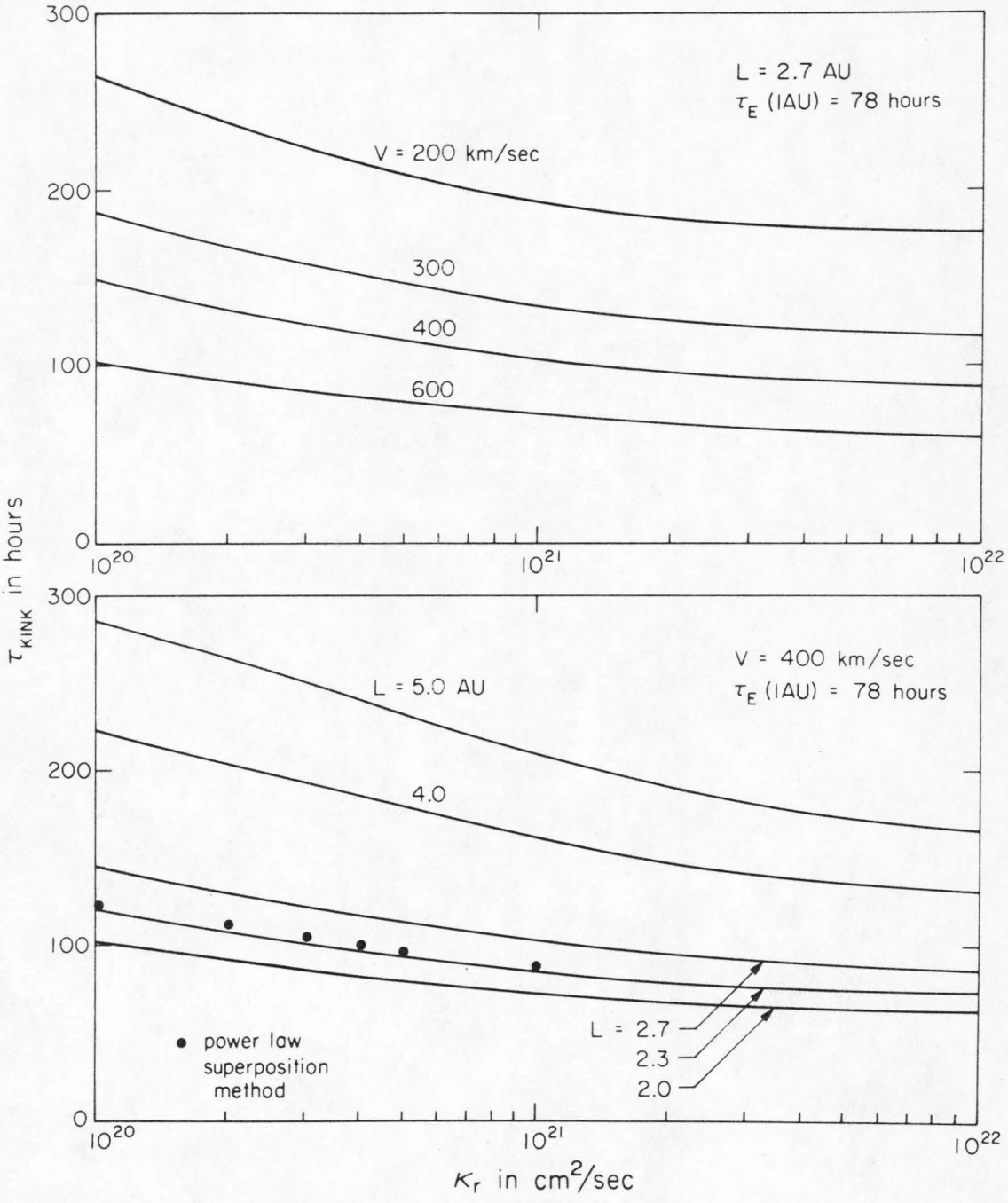

Figure V-17: The dependence of τ_{KINK} on V, L and κ_r is shown using both the simple formula and the complete power law superposition method.

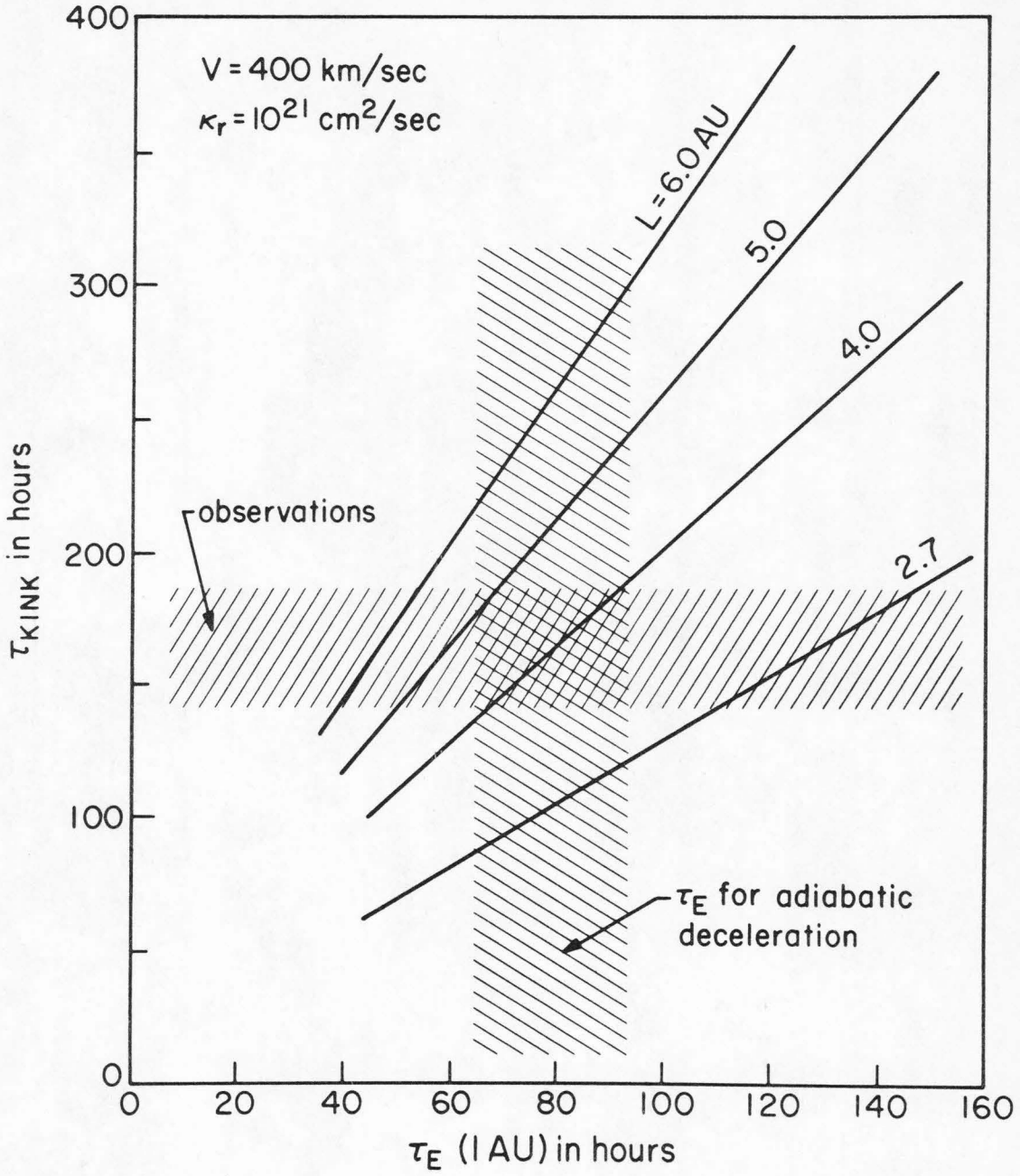

Figure V-18: τ_{KINK} is plotted vs. τ_E(1 AU) for various values of the boundary position L. The cross-hatched areas indicate the τ_E(1 AU) for pure adiabatic deceleration and the τ_{KINK} observations for the 7 June 69 and 31 Jan 70 flare events. The uncertainty in τ_E reflects the observed fluctuations in solar wind velocity.

the particle distribution, but this effect is overshadowed by the direct dependence of $\tau_E(r)$ on V -- an increase in V thus also increases the energy-loss rate because the solar wind expansion is everywhere occurring more rapidly. The dependence on κ_r is surprisingly weak, and is no doubt due to the variation of the particle distribution with the ratio V/κ (see Figure V-5).

Figure V-18 shows the linear dependence of τ_{KINK} on τ_E(1 AU) for various boundary positions L. The observed τ_{KINK} values for 7 June 69 and 31 Jan 70 are included for reference. This figure makes it clear that in order to duplicate the measured τ_{KINK} of 160 - 190 hours one must either a) move the boundary out to L = 4-5 AU while retaining pure adiabatic deceleration τ_E(1 AU) $\simeq$ 78 hours, or b) keep the boundary at the usual 2.3-2.7 AU but assume a weaker energy-change process characterized by τ_E(1 AU) $\simeq$ 110 - 140 hours. The observations could also be matched with the new solution by using V $\simeq$ 250 km/sec, but this is in direct conflict with the ~400 km/sec value measured in interplanetary space at the time.

In addition to the kink movement, it is evident from Figure V-15 that the kink in the power law superposition spectrum becomes slightly more rounded as it evolves. A quantitative expression of this "kink rounding" is given in Figure V-19, which plots the curvature $d\gamma(T)/d\ln T$ evaluated at $\gamma = 3.0$ as a function of time. The smearing effect, which is an expected result of the particle diffusion process, is unambiguous but small: the curvature changes by less than 10% over a 200 hour interval for this particular spectrum. Presumably a sharper

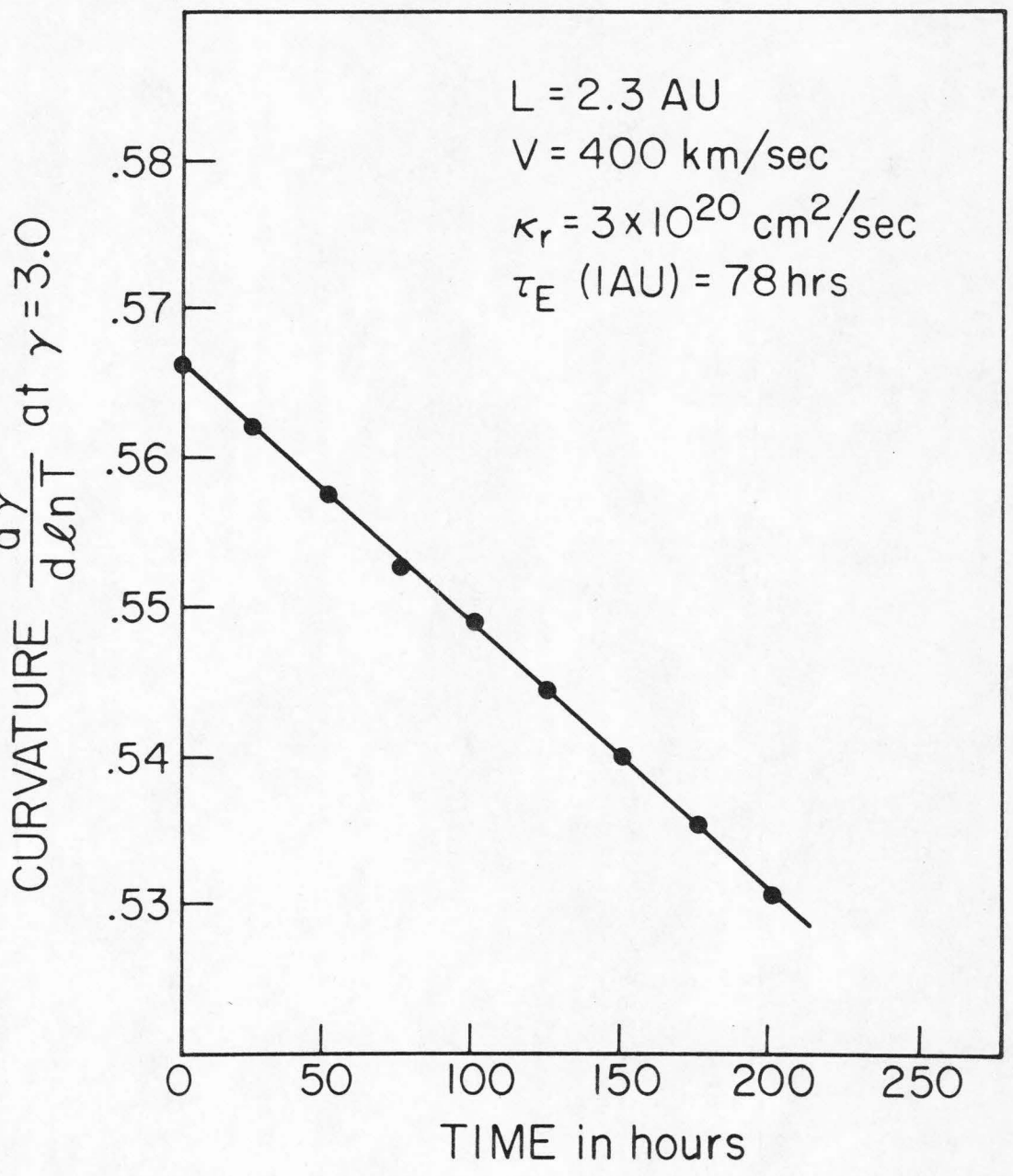

Figure V-19: The quantity $d\gamma(T)/d\ln T$ evaluated at $\gamma = 3.0$ via the power law superposition method is plotted vs. time. This quantity is a measure of the curvature or sharpness of the kink in the spectrum, and it is apparent that a finite but small (~10%) smearing effect occurs over the 200 hour time interval shown.

spectral feature would be initially smeared more rapidly. Unfortunately, this rounding is an order of magnitude too small to be measured by the OGO-6 experiment during a typical 3-4 day observation period. The fact that the analytic solution predicts a small finite rounding for this particular spectrum suggests that experimental verification could be made by comparing more accurately determined solar flare proton spectra with the evolution of better power law approximations.

4. Conclusions Concerning the Energy-Change Process

One would like to be able to decide either for or against the existence of a competing acceleration process, but the investigation thus far shows that the lower rate of kink movement observed can be produced equally well by a larger boundary distance or by an energy-change process roughly half as strong as the adiabatic process. A final attempt was made to settle the issue by re-fitting the event intensity vs. time profiles using parameters which produce a τ_{KINK} of 160 - 190 hours.

Figures V-20 and V-21 compare fits to the 7 June and 31 Jan events at 1.17 - 1.27 MeV using a) a larger boundary and b) a weaker energy-change process. For the directly-connected 31 Jan 70 event only the radial part of the solution was used (per the discussion in Section V-E-4). Unfortunately the fits are equally good for the two cases, and no conclusion can be drawn.

It is clear that moving the boundary out to L = 4-5 AU merely changes the peak in the particle distribution out to r $\simeq$ 2.3 AU, so that

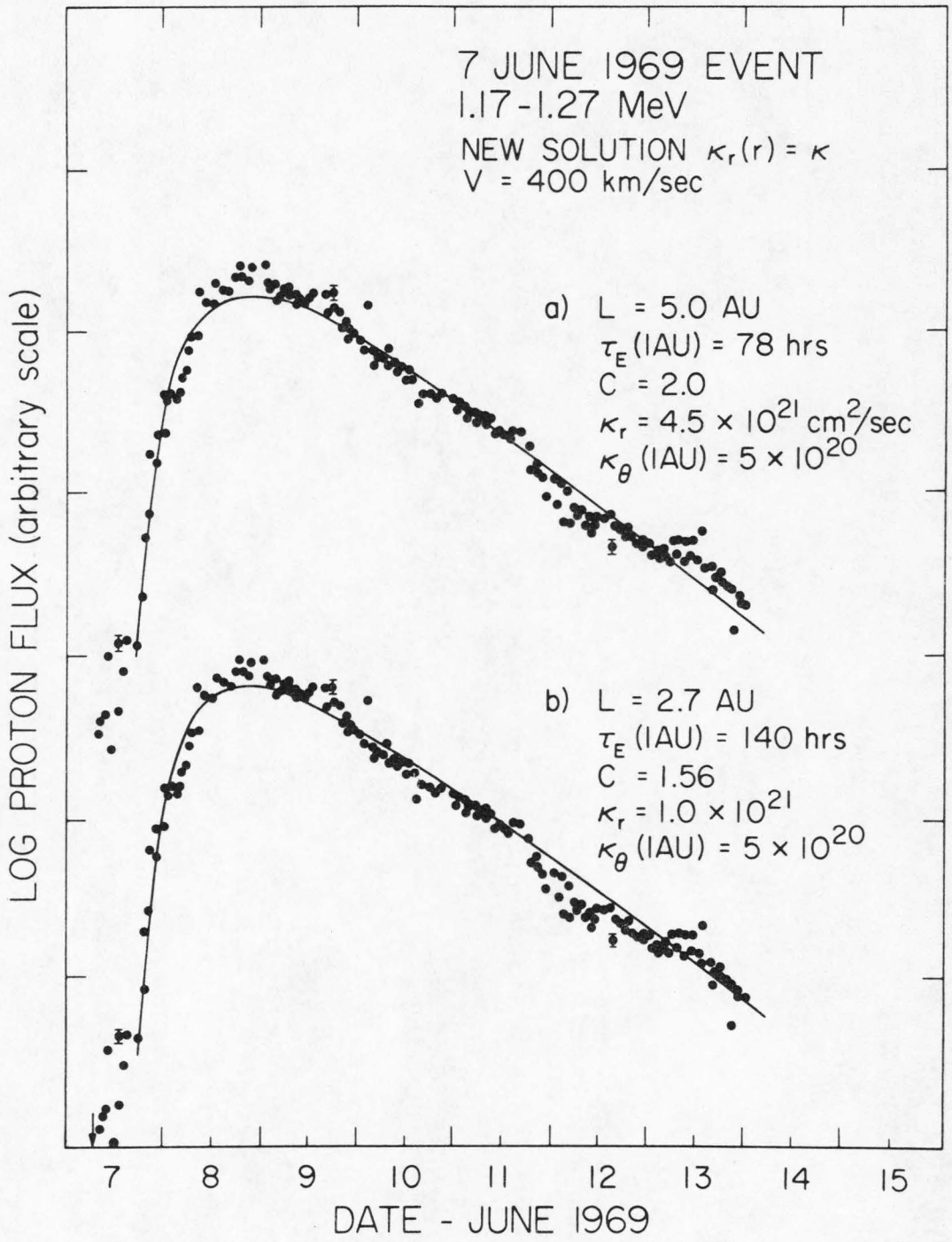

Figure V-20: Fits to the 7 June 1969 event at 1.17 - 1.27 MeV using the new solution. The observed $\tau_{KINK} \approx 182$ hours was matched by two different methods: by a) moving the boundary out to L = 5.0 AU and b) decreasing the strength of the energy change process to τ_E(1 AU) = 140 hours.

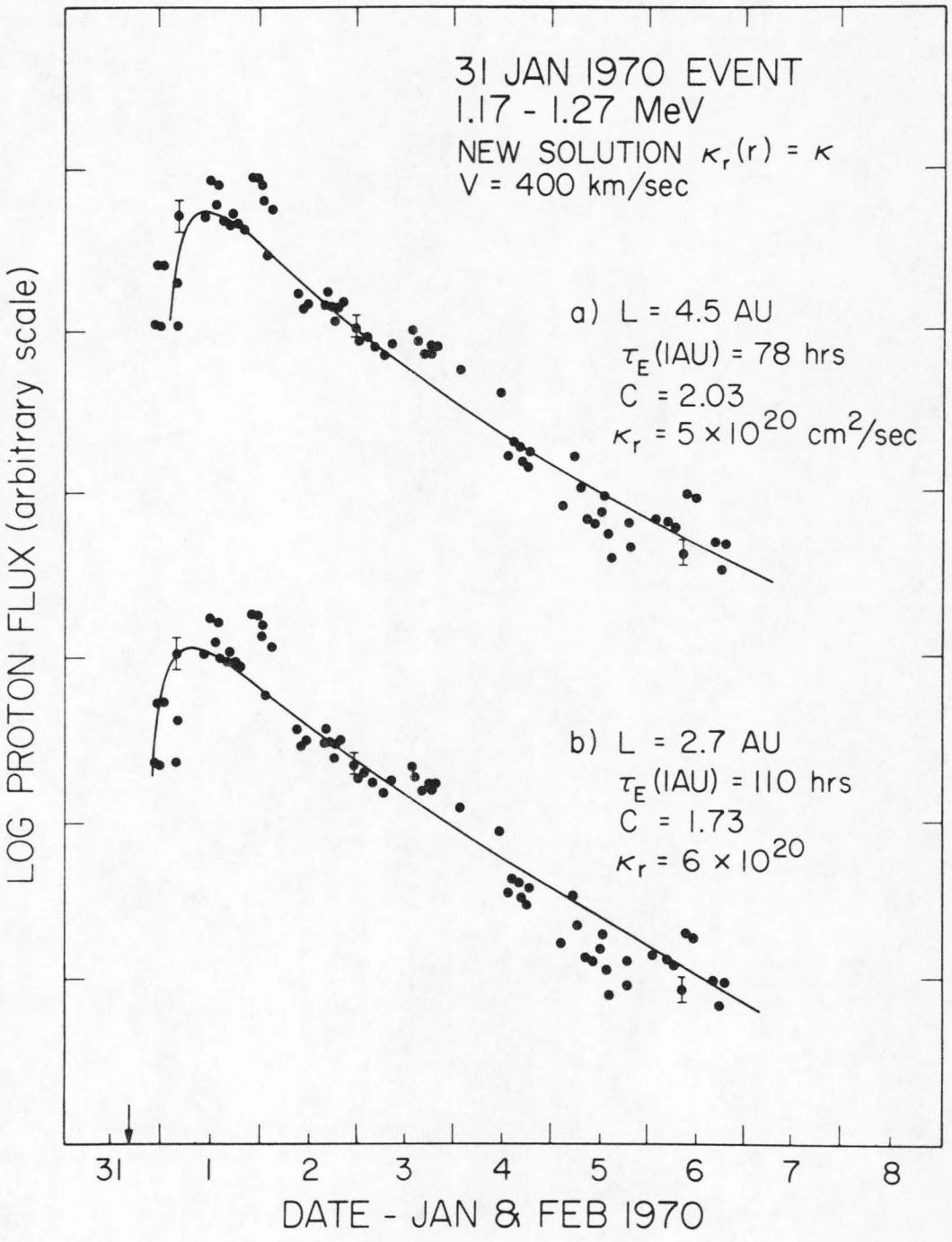

Figure V-21: Fits to the 31 Jan 1970 event at 1.17-1.27 MeV using the radial part of the new solution. The observed $\tau_{KINK} \simeq 160$ hours was matched by two different methods: a) moving the boundary out to L = 4.5 AU and b) by decreasing the strength of the energy-change process to τ_E(1 AU) = 110 hours.

$\tau_E(2.3\ \text{AU})$ matches the observed $\tau_{KINK} \simeq 180$ hours. Since any means of peaking the distribution at 2.3 AU will produce essentially the same energy-change effect, a third method for reproducing the observed energy-change rate can be evoked by employing a $\kappa_r(r)$ which depends on distance r (beyond 1 AU) in such a way that the particles are peaked much closer to the boundary. Although this approach is not within the assumptions of the new solution, it can be understood qualitatively in terms of the discussion present earlier in Section V-D-2. It can easily be seen that a $\kappa_r(r)$ which decreases beyond 1 AU will cause the particle distribution to be peaked at a larger radial distance. This effect can be explained by noticing that a smaller κ_r increases the ratio V/κ on the average and thus pushes the peak outward (see Figure V-5). It is interesting that this third method requires a form for $\kappa_r(r)$ which has the opposite radial dependence to the frequently-used $\kappa_r(r)$ which increases with distance.

It is apparent that this energy-change question cannot easily be answered with observations at 1 AU. One would like either to follow the energy vs. time history of a single particle or alternatively to at least determine the spatial distribution of particles so that the energy loss rate $\tau_E(r)^{-1}$ of the "average" particle is known. Gleeson and Palmer[45] have suggested (but not carried out) a rather difficult experiment which would afford a direct measurement of the energy-loss rate: they propose the simultaneous observation from two spacecraft situated on the same heliocentric radial line of a "pulse" of nearly

monoenergetic particles such as might be convected outward during a flare event.

VI. CONCLUSION

The new solution presented here consists of resolving the differential equation for the radial part of the particle propagation, using $\kappa_r(r)$ = constant, and including the effects of convection and energy-change known to be important at low energies. This new radial solution, when combined with the azimuthal solution used by Burlaga [10] and Forman [12], is capable of accurately reproducing both the rise and decay of the "classical" prompt solar flare proton event observed at 1 AU using reasonable values of the parameters.

The principal limitations of the new solution are that it assumes a diffusion tensor which is independent of energy and diagonal in a reference frame aligned with the radial direction (rather than with the B-field). Within these limitations, the comparison of the predictions of the new solution with actual data leads to the following conclusions concerning solar flare particle propagation in the interplanetary medium:

a) The Diffusion Tensor -- The success of the new solution in fitting both the rise and decay of flare events indicates that $\kappa_r(r)$ = constant is a better approximation to the actual conditions inside the 1 AU than is $\kappa_r(r) \propto r$. It is not necessary to invoke a scatter-free region near the sun in order to reproduce the fast rise time observed for directly-connected flare events. The κ_r values derived from fits to actual data have a weak energy

dependence and agree reasonably well with the estimates for $\kappa_{//}$ based on Mariner IV magnetic field measurements.

b) The Azimuthal Propagation -- The simple point-injection and 2-dimensional longitudinal diffusion adopted here does not seem to be an accurate description of the actual processes at work. Although it appears that the azimuthal solution can be neglected for directly-connected events, some kind of longitudinal propagation must be invoked to explain the slow rise times of east limb events. Even though this propagation may occur near the sun, the 2-dimensional interplanetary diffusion adopted in this discussion is capable of explaining at least qualitatively the slow rise profiles of these east limb flares.

c) Free-Escape Boundary -- The success of the new solution in fitting the decay phases of flare events indicates that the assumption of a free-escape boundary at some 2 - 5 AU is at least a reasonable approximation to the actual interplanetary conditions. For example a sharp boundary may not exist, but there might instead be a finite region of rapidly increasing diffusion coefficient.

d) Anisotropy -- Despite the limitations of the solution with respect to the actual spiral nature of the interplanetary field, it is possible to understand essentially all of the features of the observed vector anisotropy in terms of the solution. In fact, even the absolute value of the residual anisotropy predicted agrees well with the 5 - 10% observed.

e) The Energy-Change Process -- By superimposing power law spectra, it was possible to reproduce a spectrum with a convex kink and to verify, via the new solution, that such a feature will move to lower energies as has been observed. The existing energy-change observations can be explained in the light of the new solution in at least three different ways: 1) by means of a boundary at ~2.7 AU and an energy-change process weaker than pure adiabatic deceleration, 2) by pure adiabatic deceleration and a boundary at 4-5 AU, or 3) by a somewhat different solution with a boundary at ~2.7 AU and a form for $\kappa_r(r)$ which decreases beyond 1 AU. The resolution of this question must await more sophisticated spacecraft measurements.

Appendix A

OGO-6 Monthly Summary Plots for June 1969 through February 1970

Figure A-1 consists of computer-generated plots which summarize the OGO-6 range telescope polar counting rates (see Section II) as well as certain geophysical data from the ESSA Bulletins[27,28]. The nine months of June 1969 through February 1970 are covered. Full credit for these summary plots must go to L. C. Evans[63], for developing the necessary computer coding, and to T. L. Garrard[64] for generating the OGO-6 plots shown here.

For each month the following information, starting at the top, is plotted vs. time:

1) The average polar $D1\overline{D8}$ counting rate in cts/sec (labelled D1) is plotted logarithmically. This rate is nearly insensitive to electrons but responds to nuclei from ~1.2 to ~20 MeV/nucleon.

2) The average polar $D2\overline{D8}$ counting rate in cts/sec (labelled D2) is plotted logarithmically. This rate responds to electrons $\gtrsim$ 200 keV and to nuclei $\gtrsim$ 3 MeV/nucleon.

3) The average polar $D1D2\overline{D8}$ counting rate in cts/sec (labelled D1D2) is plotted logarithmically. This rate responds to nuclei from ~3 to ~20 MeV/nucleon.

4) The average polar $D2D3\overline{D8}$ counting rate in cts/sec (labelled D2D3) is plotted logarithmically. This rate responds to electrons $\gtrsim$ 1 MeV and nuclei $\gtrsim$ 19 MeV/nucleon.

5) The >10 MeV solar proton fluxes measured by the Solar Proton Monitoring Experiment aboard Explorer 41. This cosmic ray telescope which is described briefly in the ESSA descriptive text[28], also has some electron sensitivity. The large rate excursions repeated at ~4.3 day intervals are due to the periodic passage of the satellite through the earth's radiation belts. These excursions have been largely suppressed by the plotting program.

6) Normalized hourly average counting rates for 2 neutron monitors: Alert (upper line) and Deep River.

7) The standardized K-index of geomagnetic activity from twelve observations are averaged to obtain K_p. The quasi-logarithmic K_p scale ranges from 0(quiet) to 9 (very disturbed). The legend for the plots is identical to that adopted by ESSA.

8) Geomagnetic storm sudden commencements (labelled SC) are indicated by solid triangles if confirmed and by open triangles if unconfirmed.

9) Magnetogram sudden impulses (labelled SI) are indicated by solid diamonds if confirmed and open diamonds if unconfirmed.

10) Optical solar flares (labelled SOLAR FLARE) of importance greater than 2F observed by the world-wide system of solar observatories are indicated by a small vertical line plotted at the beginning time of the flare. The importance (2N, 3B, etc.) is included. Periods of no flare patrol are indicated by horizontal lines of appropriate length.

11) 2 - 12$\mathring{A}$ solar x-ray flares (labelled X RAY) with a peak flux

at least 4 times the ambient value are indicated by a vertical line. These data were collected by experiments aboard Explorers 33 and 35.

12) Occurrences of type-IV radio emission (labelled TP IV RADIO) are indicated by vertical lines. This radiation is normally associated with the acceleration of solar flare electrons.

The gaps in the OGO-6 data after November 1969 are in most cases due to incomplete processing rather than actual data coverage problems.

Figure A-1

OGO-6 Data Summary Plots

A description of these plots is given in the text of Appendix A:

Graph a: June 1969

Graph b: July 1969

Graph c: August 1969

Graph d: September 1969

Graph e: October 1969

Graph f: November 1969

Graph g: December 1969

Graph h: January 1970

Graph i: February 1970

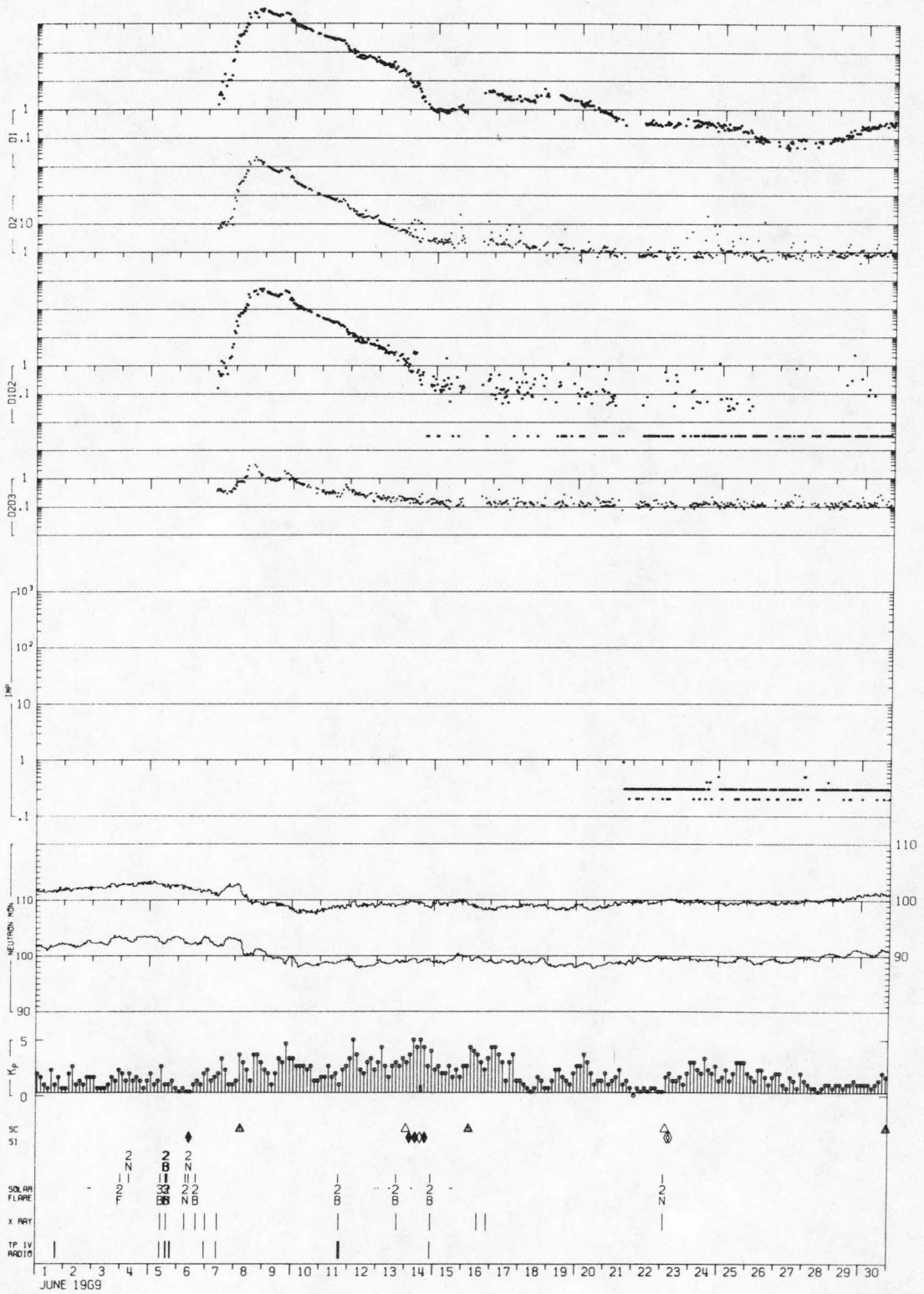
D1
D2
D102
D203
INP
NEUTRON MON
110
100
90
K_p
SC
SI
SOLAR FLARE
X RAY
TP IV RADIO
JUNE 1969

Figure A-1-a

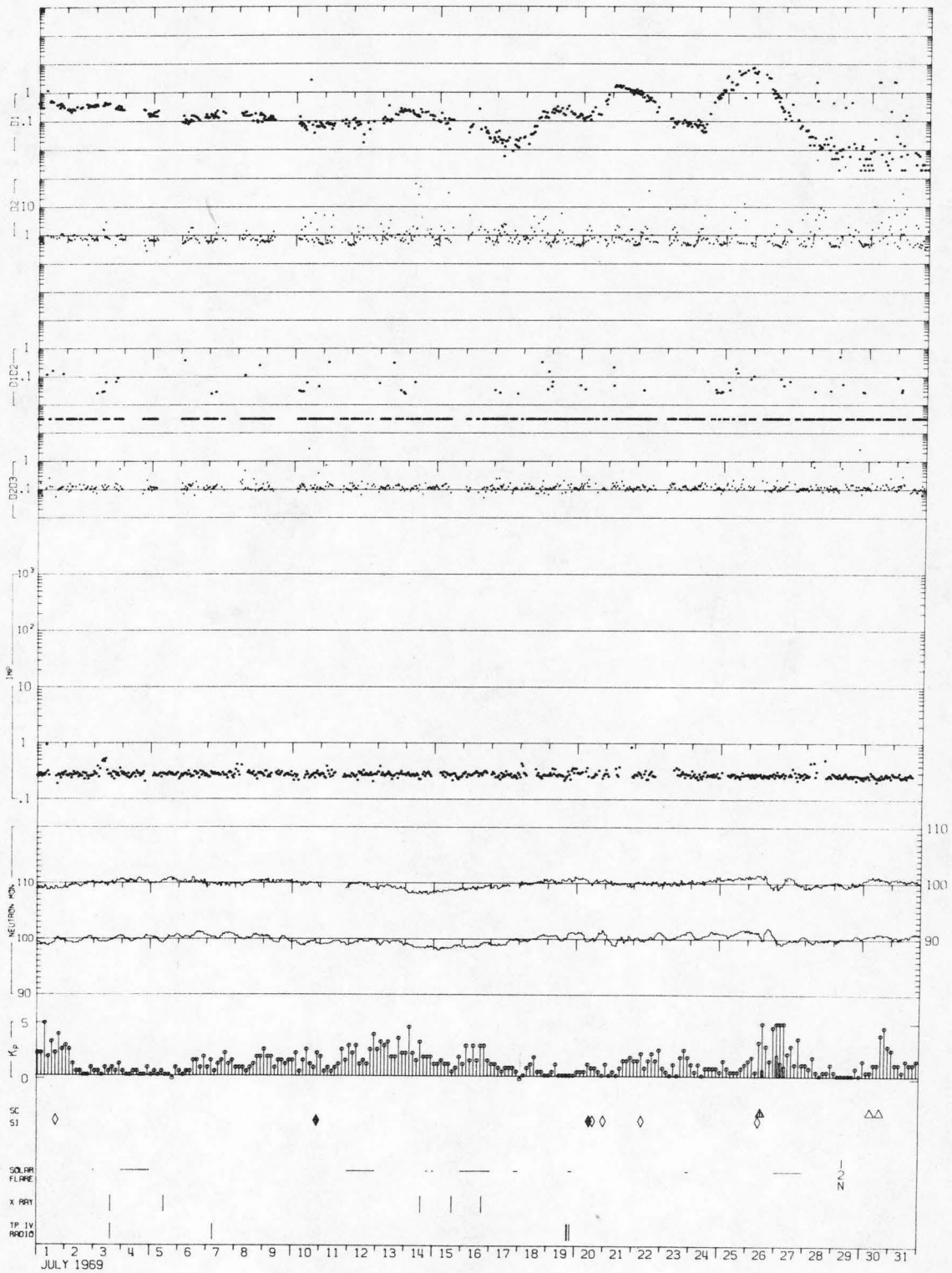
D1
D2D10
D1D2
D2D3
INP
NEUTRON MON
110
100
90
K_p
SC
SI
SOLAR FLARE
X RAY
TP IV RADIO
1 2 3 4 5 6 7 8 9 10 11 12 13 14 15 16 17 18 19 20 21 22 23 24 25 26 27 28 29 30 31
JULY 1969

Figure A-1-b

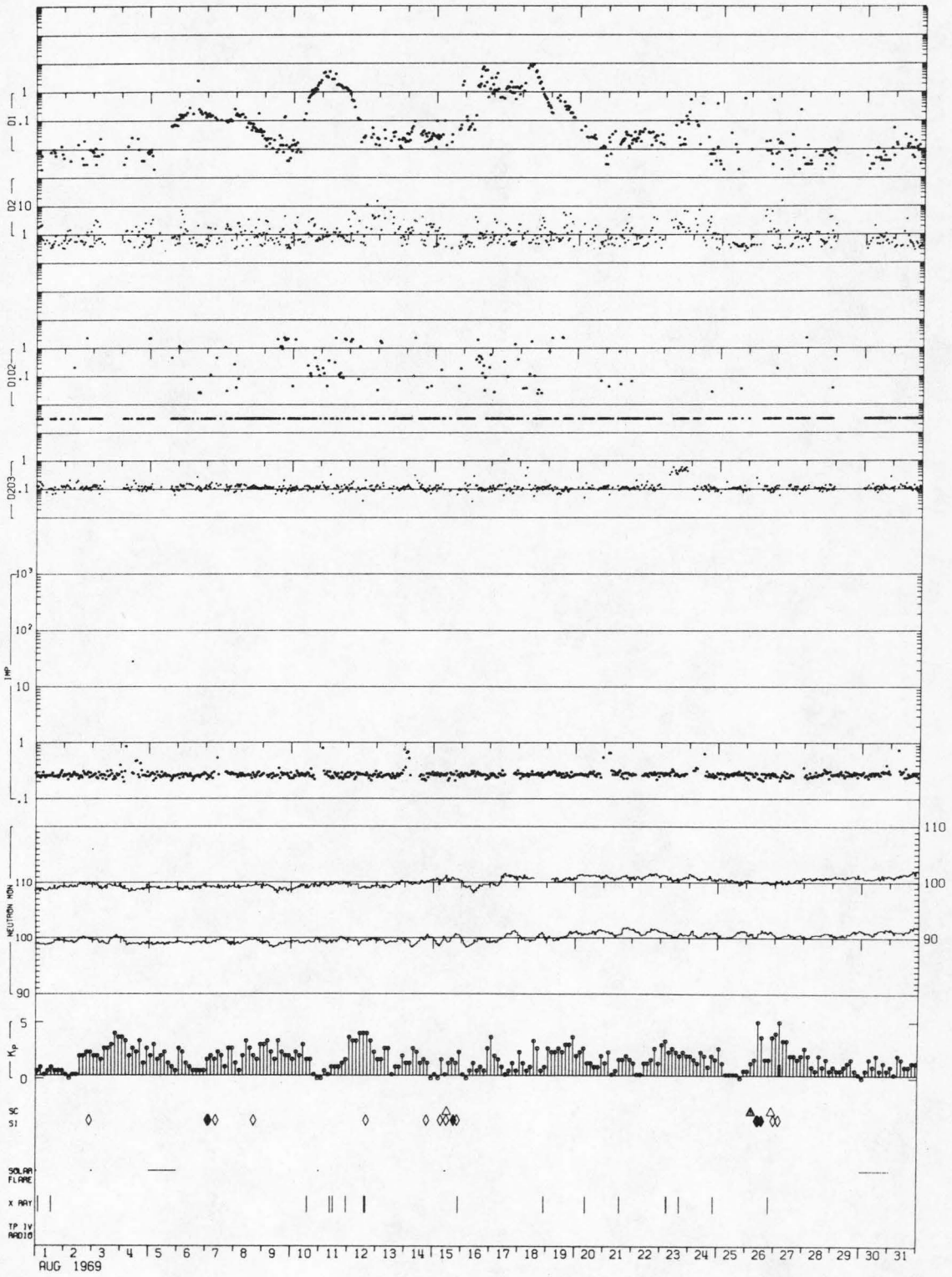
D1
D2
D102
D203
IMP
NEUTRON MON
Kp
SC
SI
SOLAR FLARE
X RAY
TP IV RADIO
1 2 3 4 5 6 7 8 9 10 11 12 13 14 15 16 17 18 19 20 21 22 23 24 25 26 27 28 29 30 31
AUG 1969

Figure A-1-c

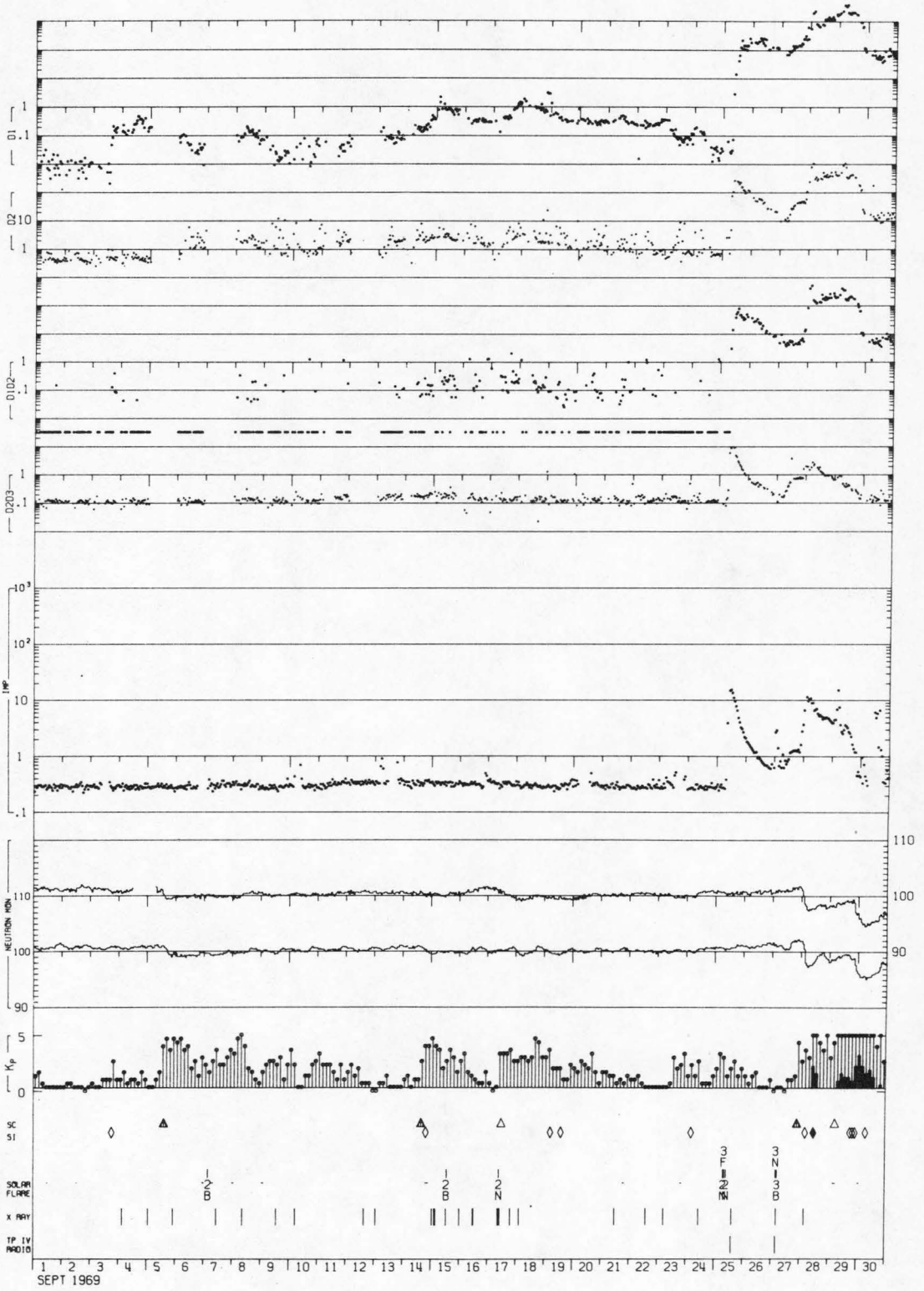
D1
D2
D102
D203
IMP
NEUTRON MON
Kp
SC
SI
SOLAR FLARE
X RAY
TP IV RADIO
2B
2B
2N
3F2N
3N3B
SEPT 1969

Figure A-1-d

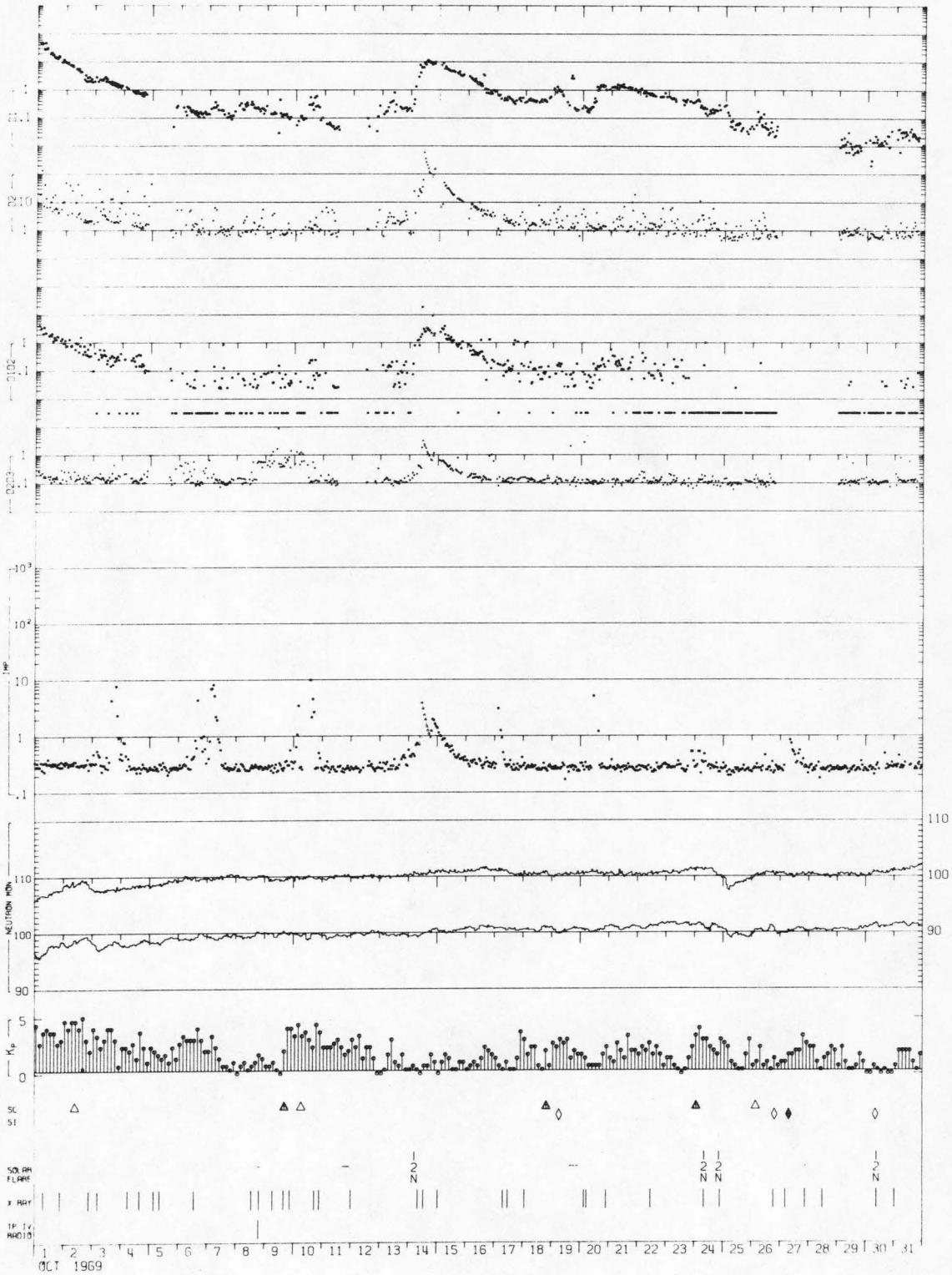
0.1
0210
0102
0203
10^3
10^2
10
1
.1
PHP
110
100
90
NEUTRON MON
110
100
90
5
0
K_p
SC
SI
SOLAR FLARE
X RAY
1P IV RADIO
1 2 3 4 5 6 7 8 9 10 11 12 13 14 15 16 17 18 19 20 21 22 23 24 25 26 27 28 29 30 31
OCT 1969

Figure A-1-e

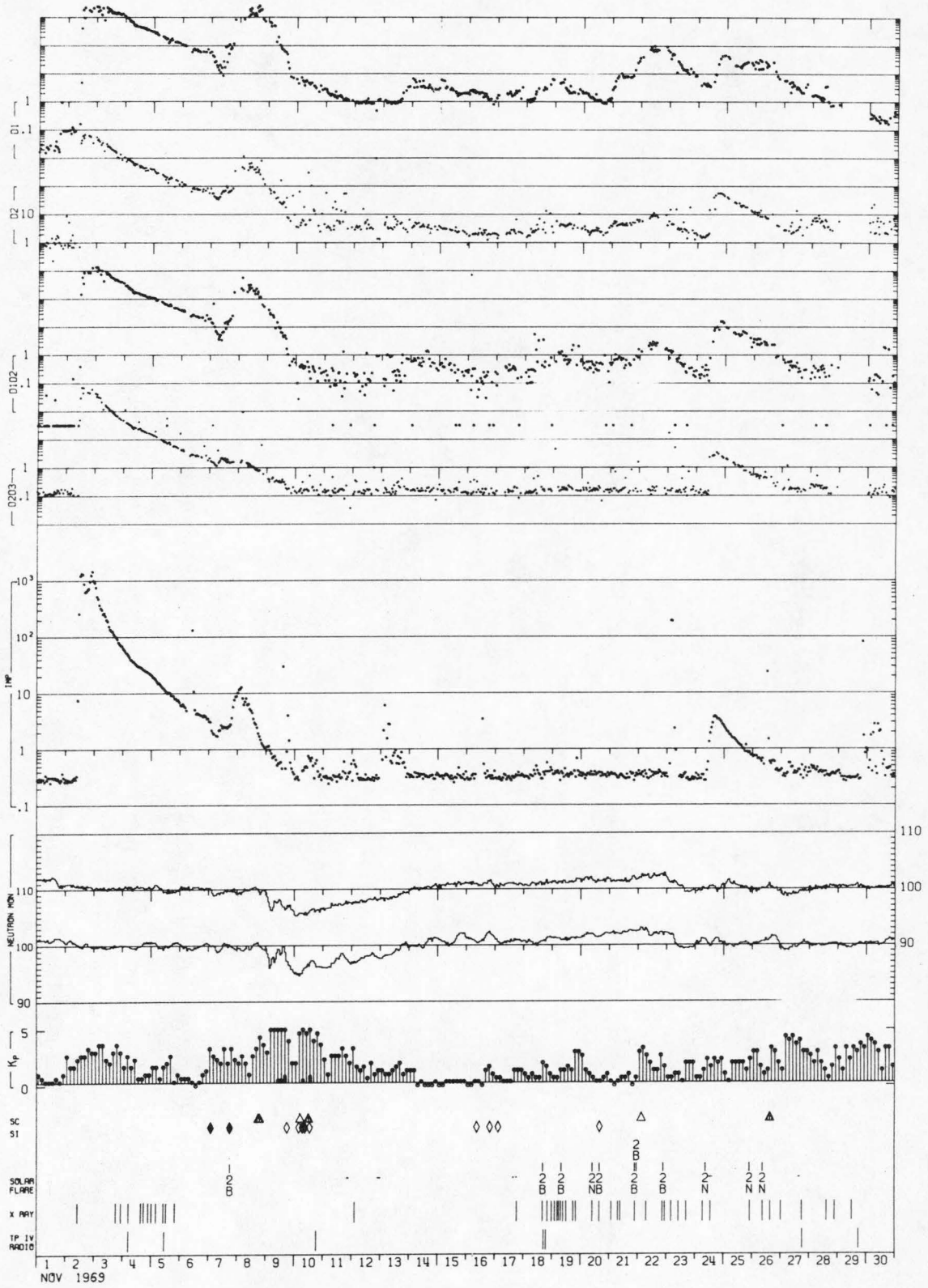
D1
D2
D102
D203
IMP
NEUTRON MON
Kp
SC
SI
SOLAR FLARE
X RAY
TP IV RADIO
NOV 1969

Figure A-1-f

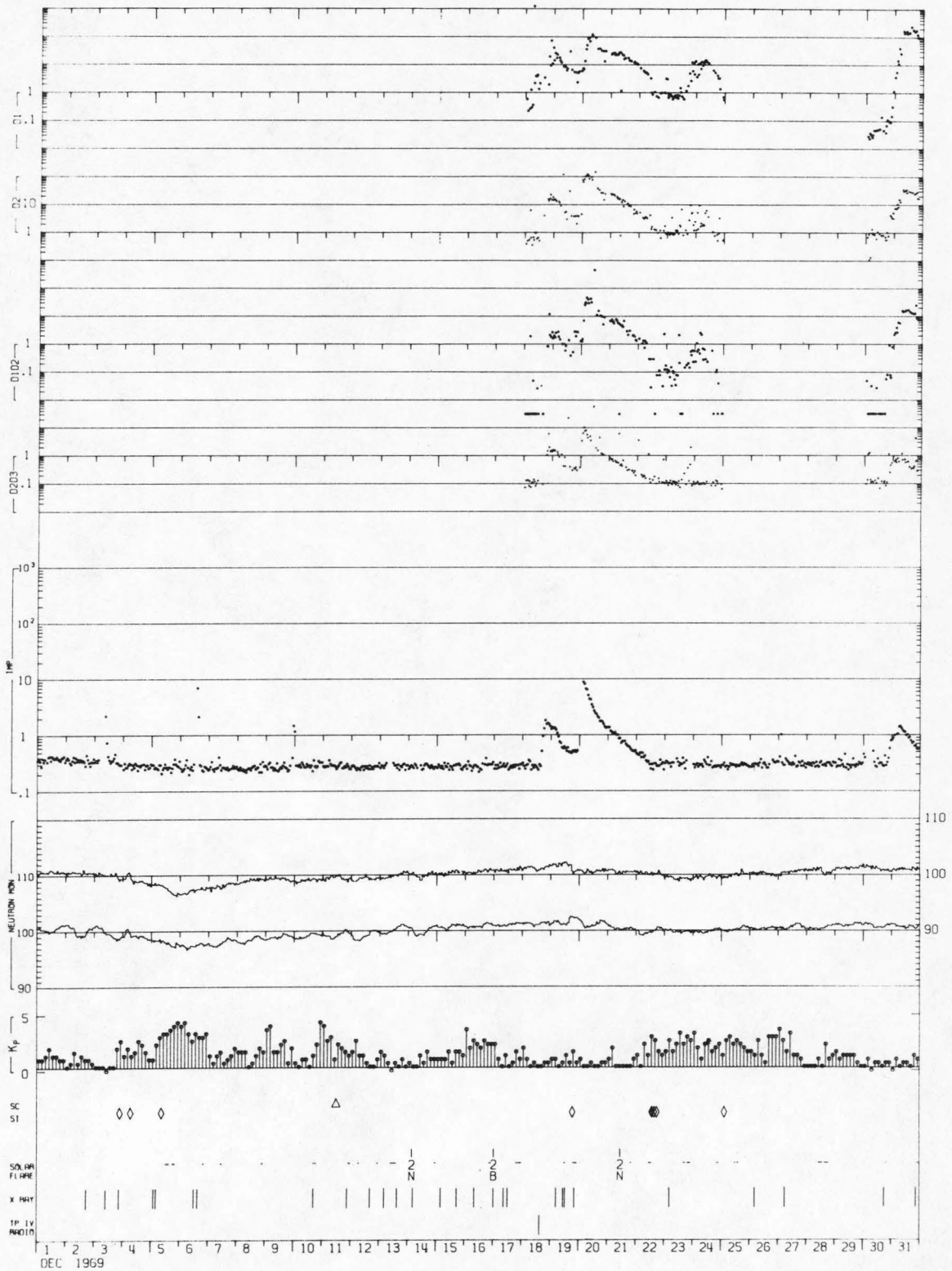
D1
D2
D102
D203
IMP
NEUTRON MON
110
100
90
K_p
SC
SI
SOLAR FLARE
X RAY
TP IV RADIO
1 2 3 4 5 6 7 8 9 10 11 12 13 14 15 16 17 18 19 20 21 22 23 24 25 26 27 28 29 30 31
DEC 1969

Figure A-1-g

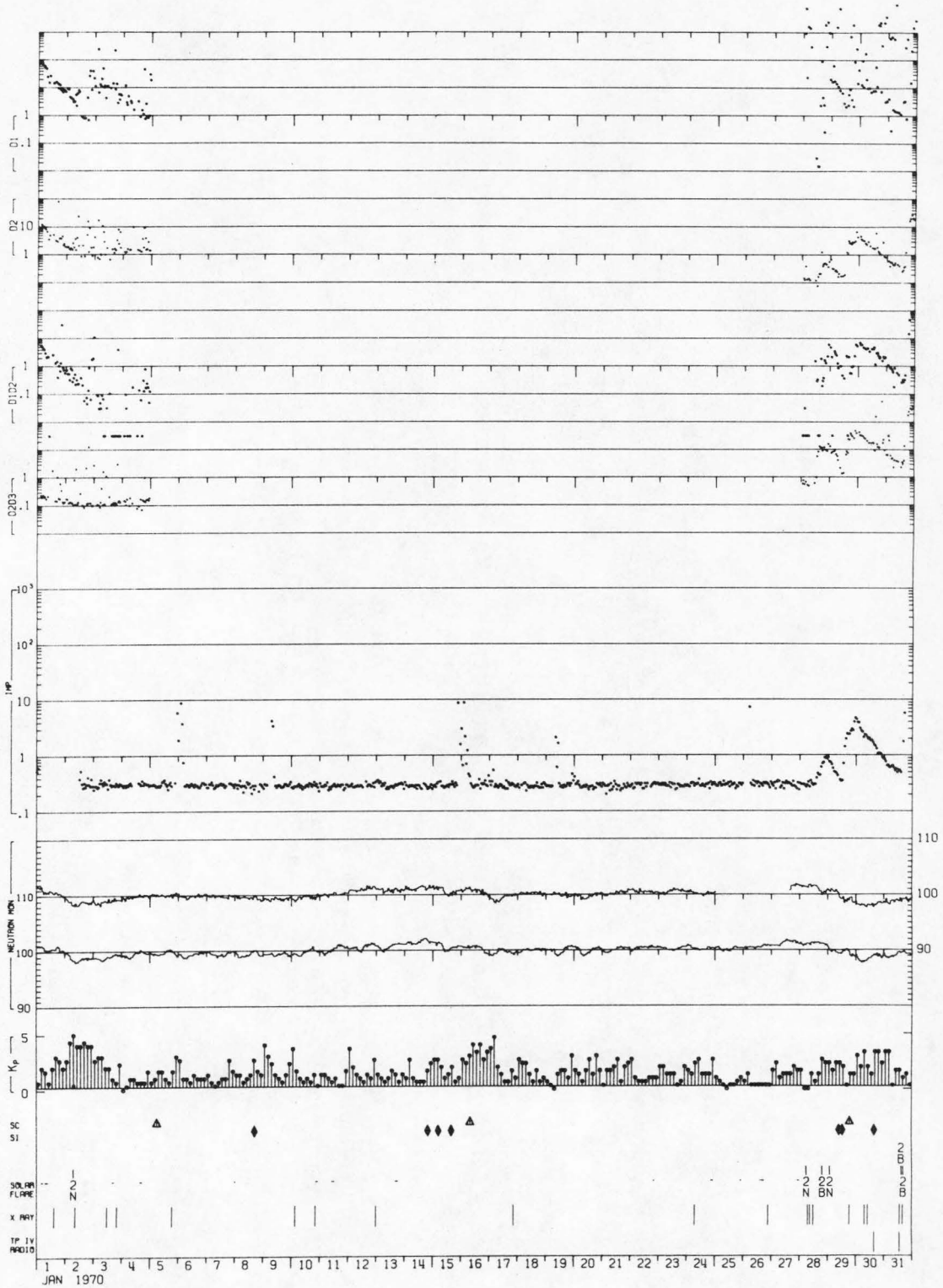
D1
D2
D1D2
D2D3
IMP
NEUTRON MON
110
100
90
K_p
SC
SI
SOLAR FLARE
X RAY
TP IV RADIO
1 2 3 4 5 6 7 8 9 10 11 12 13 14 15 16 17 18 19 20 21 22 23 24 25 26 27 28 29 30 31
JAN 1970

Figure A-1-h

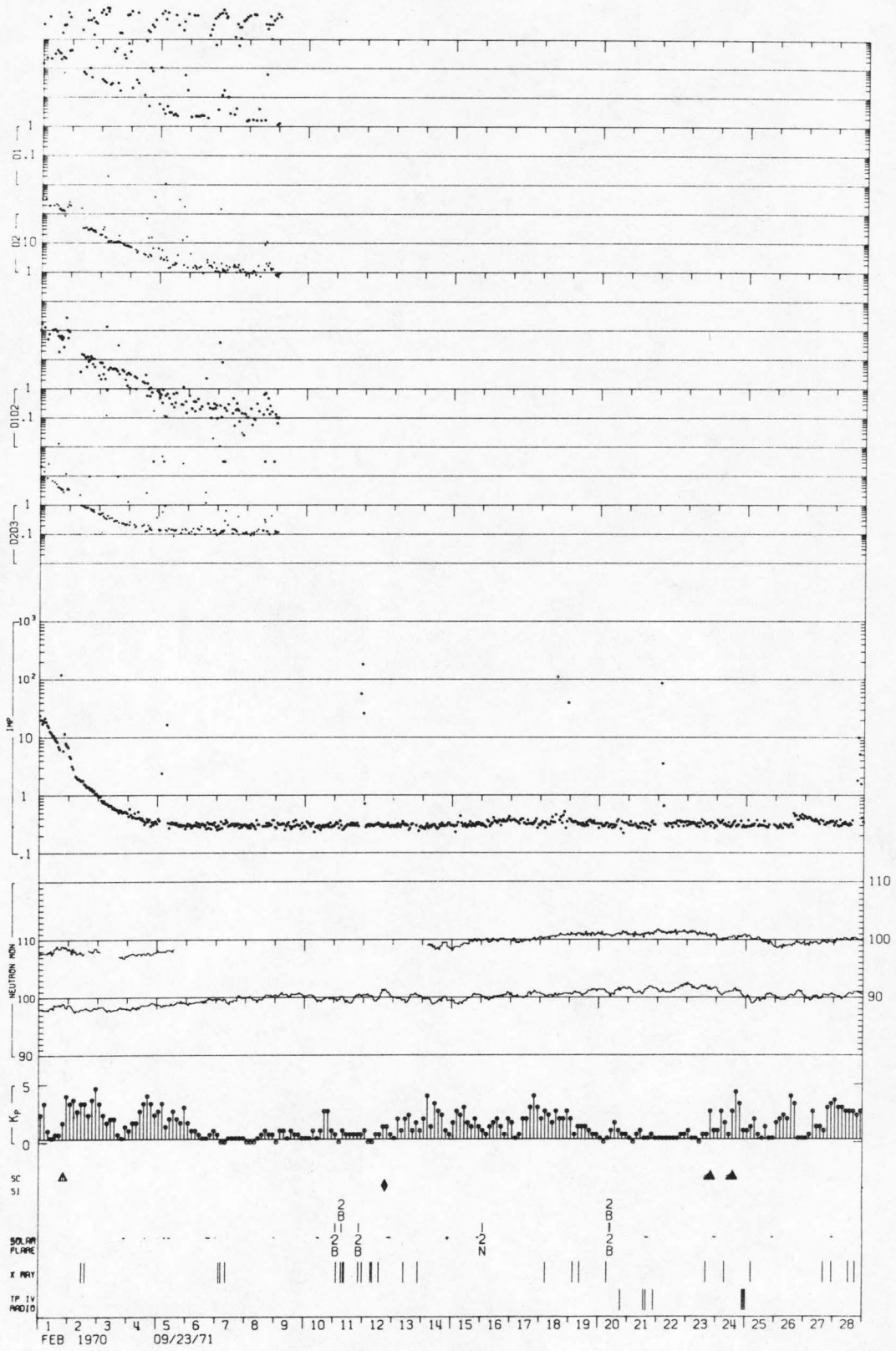
01
1
.1
02
10
1
0102
1
.1
0203
1
.1
IMP
10³
10²
10
1
.1
NEUTRON MON
110
100
90
110
100
90
Kp
5
0
SC
SI
SOLAR FLARE
X RAY
TP IV RADIO
2B
2B
2B
2N
2B
1 2 3 4 5 6 7 8 9 10 11 12 13 14 15 16 17 18 19 20 21 22 23 24 25 26 27 28
FEB 1970
09/23/71

Figure A-1-i

Appendix B

Solution for the Azimuthal Dependence

Assuming $\kappa_\theta(r) = \kappa_1 r^2$, the equation for $Q(\theta,\phi,t)$ in spherical polar coordinates centered at the sun is

$$\frac{\kappa_1}{\sin\theta}\frac{\partial}{\partial\theta}\sin\theta\frac{\partial Q}{\partial\theta} + \frac{\kappa_1}{\sin^2\theta}\frac{\partial^2 Q}{\partial\phi^2} = \frac{\partial Q}{\partial t} \qquad \text{(B-1)}$$

The separation of variables can be carried further by writing

$$Q(\theta,\phi,t) = \Theta(\theta)\, e^{\pm im\phi}\, e^{-\ell(\ell+1)\kappa_1 t} \qquad \text{(B-2)}$$

Then only a differential equation for Θ remains

$$\frac{1}{\sin\theta}\frac{\partial}{\partial\theta}\sin\theta\frac{\partial\Theta}{\partial\theta} - \frac{m^2}{\sin^2\theta}\Theta = -\ell(\ell+1)\Theta \qquad \text{(B-3)}$$

with the well-known solutions $P_\ell^m(\cos\theta)$, $Q_\ell^m(\cos\theta)$. The solution has the general form

$$Q(\theta,\phi,t) = \sum_\ell \sum_m \left[A_{\ell m} P_\ell^m(\cos\theta) + B_{\ell m} Q_\ell^m(\cos\theta)\right] e^{\pm im\phi}\, e^{-\ell(\ell+1)\kappa_1 t} \qquad \text{(B-4)}$$

Assuming δ-function injection at (θ_o, ϕ_o), we must require

$$Q(\theta,\phi,t=0) = f(\theta,\phi) = \frac{\delta(\theta-\theta_o)}{\sin\theta}\,\delta(\phi-\phi_o) \qquad \text{(B-5)}$$

The coefficients $A_{\ell m}$ and $B_{\ell m}$ can easily be determined by using the appropriate orthogonality integrals[65], and the specific solution

becomes:

$$Q(\theta,\phi,t) = \sum_{\ell=0}^{\infty} \sum_{m=-\ell}^{\ell} \frac{(\ell - m)!}{(\ell + m)!} \frac{2\ell + 1}{4\pi} P_\ell^m(\mu) P_\ell^m(\mu_o) e^{\pm im(\phi-\phi_o)} e^{-\ell(\ell+1)\kappa_1 t} \tag{B-6}$$

where $\mu = \cos\theta$ and $\mu_o = \cos\theta_o$. The addition theorem for spherical harmonics[66] can now be applied

$$P_\ell(\cos\gamma) = \frac{4\pi}{2\ell + 1} \sum_{m=-\ell}^{\ell} \frac{(\ell - m)!}{(\ell + m)!} P_\ell^m(\mu) P_\ell^m(\mu_o) e^{\pm im(\phi-\phi_o)} \tag{B-7}$$

γ is the angle between (θ,ϕ) and (θ_o,ϕ_o) given by

$$\cos\gamma = \cos\theta \cos\theta_o + \sin\theta \sin\theta_o \cos(\phi - \phi_o) \tag{B-8}$$

Our solution for 2-dimensional diffusion thus reduces to the 1-dimensional solution

$$Q(\gamma,t) = \sum_{\ell=0}^{\infty} \frac{2\ell + 1}{4\pi} P_\ell(\cos\gamma) e^{-\ell(\ell+1)\kappa_1 t} \tag{B-9}$$

Evidently the 2-dimensional random walk in θ and ϕ is completely equivalent to a 1-dimensional diffusion problem because the gradient $\vec{\nabla}Q$ is directed radially outward from (θ_o, ϕ_o). This will be the case as long as the injection profile $f(\theta,\phi)$ is symmetric about the point (θ_o, ϕ_o) and $\kappa_\theta(r) = \kappa_\phi(r)$.

Appendix C

Derivation of the New Solution to the Radial Equation

1. Derivation of the Solution

A solution $R(r,t)$ will now be derived to the equation

$$\frac{\partial^2 R}{\partial r^2} + \left(\frac{2}{r} - \frac{V}{\kappa}\right)\frac{\partial R}{\partial r} - \frac{2CV}{\kappa r} R = \frac{1}{\kappa}\frac{\partial R}{\partial t} \qquad \text{(C-1)}$$

using the assumptions and boundary conditions listed in Section V-C-1.

It can easily be shown that if we write

$$R(r,t) = y(r)\,\frac{1}{r}\,e^{+Vr/2\kappa}\,e^{-t/\tau} \qquad \text{(C-2)}$$

then the function $y(r)$ is the solution to

$$\frac{d^2 y}{dr^2} + \left(\alpha - \frac{\beta}{r}\right) y = 0 \qquad \text{(C-3)}$$

where $$\alpha = \frac{1}{\kappa\tau} - \frac{V^2}{4\kappa^2} > 0 \qquad \text{(C-4)}$$

and $$\beta = \frac{V}{\kappa}(2C - 1) > 0 \qquad \text{(C-5)}$$

A simple change of variable, $\rho = \sqrt{\alpha}r$ reduces equation C-3 to a form of the Coulomb wave equation

$$\frac{d^2 y}{d\rho^2} + \left[1 - \frac{\beta}{\sqrt{\alpha}}\frac{1}{\rho}\right] y = 0 \qquad \text{(C-6)}$$

with solutions which are the regular and irregular Coulomb wave functions, $F_o(\beta/2\sqrt{\alpha},\ \sqrt{\alpha}r)$ and $G_o(\beta/2\sqrt{\alpha},\ \sqrt{\alpha}r)$.[60]

The general solution to equation C-1 can then be written

$$\mathcal{R}(r,t) = \frac{e^{Vr/2\kappa}}{r} \sum_n \left[A_n F_o(\beta/2\sqrt{\alpha_n}, \sqrt{\alpha_n}\, r) + B_n G_o(\beta/2\sqrt{\alpha_n}, \sqrt{\alpha_n} r) \right] e^{-t/\tau_n} \tag{C-7}$$

If we require that $\mathcal{R}(r,t)$ remain finite as $r \to 0$, then $B_n = 0$ and only the regular Coulomb functions are involved. The eigenvalues α_n are defined by the outer boundary condition $\mathcal{R}(L,t) = 0$. The eigenvalue equation for α_n is thus

$$F_o(\beta/2\sqrt{\alpha_n}, \sqrt{\alpha_n}\, L) = 0 \tag{C-8}$$

which must be solved by an iterative technique.

The coefficients A_n are determined by the requirement of impulsive δ-function injection at $r = r_s$:

$$\mathcal{R}(r,t=0) = \frac{\delta(r - r_s)}{r^2} \tag{C-9}$$

We can thus write

$$\mathcal{R}(r,0) = \frac{\delta(r - r_s)}{r^2} = \frac{e^{Vr/2\kappa}}{r} \sum_{n=1}^{\infty} A_n\, y_n(r) \tag{C-10}$$

where $y_n(r) = F_o(\beta/2\sqrt{\alpha_n}, \sqrt{\alpha_n}\, r)$. If we left-multiply by $\int_0^L y_m(r)\, r \exp(-\frac{V}{2\kappa} r) dr$, we have

$$\int_0^L y_m(r) \frac{\delta(r - r_s)}{r} e^{\left(-\frac{V}{2\kappa} r\right)} dr = \sum_{n=1}^{\infty} A_n \int_0^L y_n(r)\, y_m(r)\, dr \tag{C-11}$$

In Section 2 of this Appendix, the following orthogonality relationship for the regular Coulomb wave functions will be derived:

$$\int_0^L y_n(x)\, y_m(x)\, dx = N_m\, \delta_{nm} \qquad \text{(C-12)}$$

where δ_{nm} is the Knonecker delta and $y_n(0) = y_n(L) = 0$. Using this relation, we can write

$$y_m(r_s)\, \frac{e^{-\frac{V}{2\kappa} r_s}}{r_s} = \sum_n A_n\, N_m\, \delta_{nm} = N_m\, A_m \qquad \text{(C-13)}$$

Thus

$$A_n = \frac{e^{-\frac{V}{2\kappa} r_s}}{N_n\, r_s}\, F_o(\beta/2\sqrt{\alpha_n}, \sqrt{\alpha_n}\, r_s) \qquad \text{(C-14)}$$

and the radial solution for the specific boundary conditions assumed is

$$R(r,t) \propto \frac{\exp\left[V(r - r_s)/2\kappa\right]}{r\, r_s} \sum_{n=1}^{\infty} \frac{F_o(\beta/2\sqrt{\alpha_n}, \sqrt{\alpha_n}\, r_s)\, F_o(\beta/2\sqrt{\alpha_n}, \sqrt{\alpha_n}\, r)\, e^{-t/\tau_n}}{N_n} \qquad \text{(C-15)}$$

with $\beta = V(2C-1)/\kappa$ (C-16)

$$\tau_n = 4\kappa/(4\kappa^2\alpha_n + V^2) \qquad \text{(C-17)}$$

$$N_n = \int_0^L \left[F_o(\beta/2\sqrt{\alpha_n}, \sqrt{\alpha_n}\, x)\right]^2 dx \qquad \text{(C-18)}$$

2. The Orthogonality Relation for Regular Coulomb Wave Functions

We wish to demonstrate that $\int_0^L y_n(x)\, y_m(x)\, dx = 0$ for $n \neq m$ given that $y_n(x)$ is the solution to

$$\frac{d^2 y_n}{dx^2} + \left(\alpha_n - \frac{\beta}{x}\right) y_n = 0 \qquad \text{(C-19)}$$

with boundary conditions $y_n(L) = y_n(x) = 0$. We merely write down separate equations for two different eigenvalues α_n and α_m, multiply by y_m and y_n respectively, and subtract:

$$y_m\, y_n'' + \left(\alpha_n - \frac{\beta}{x}\right) y_m\, y_n = 0$$

$$y_n\, y_m'' + \left(\alpha_m - \frac{\beta}{x}\right) y_n\, y_m = 0$$

$$y_m\, y_n'' - y_m''\, y_n = (\alpha_m - \alpha_n)\, y_n\, y_m$$

$$\frac{d}{dx}\left(y_m y_n' - y_m' y_n\right) = (\alpha_m - \alpha_n)\, y_n\, y_m$$

If we left-multiply by $\int_0^L dx$, we have

$$\left[y_m\, y_n' - y_m'\, y_n\right]_0^L = (\alpha_m - \alpha_n) \int_0^L y_m\, y_n\, dx \qquad \text{(C-20)}$$

But since $y_m(0) = y_m(L) = y_n(0) = y_n(L) = 0$, the left side vanishes, and

$$\int_0^L y_n(x)\, y_m(x)\, dx = 0 \qquad \text{for } n \neq m \qquad \text{(C-21)}$$

Q.E.D.

3. Evaluating the Orthogonality Integral

Equation C-21 can be generalized as

$$\int_0^L y_n(x)\, y_m(x)\, dx = N_n\, \delta_{mn} \qquad \text{(C-22)}$$

The problem remains to evaluate the normalization integral N_n. Using equation C-21, one can write this as the following limit:

$$N_n = \lim_{\alpha_m \to \alpha_n} \frac{\left[y_m y_n' - y_m' y_n \right]_0^L}{\alpha_m - \alpha_n} \qquad \text{(C-23)}$$

applying l'Hopitals Rule, we have

$$N_n = \left\{ \frac{\partial}{\partial \alpha_m} \left[y(\alpha_m,x)\, y'(\alpha_n,x) - y'(\alpha_m,x)\, y(\alpha_n,x) \right]_{\alpha_m=\alpha_n} \right\}_0^L$$

$$= \left[y_\alpha(\alpha_n,x)\, y'(\alpha_n,x) - y_\alpha'(\alpha_n,x)\, y(\alpha_n,x) \right]_0^L \qquad \text{(C-24)}$$

where $y(\alpha_n,x) = y_n(x)$ and $y_\alpha(\alpha_n,x) = \frac{\partial}{\partial \alpha} y(\alpha,x) \Big|_{\alpha=\alpha_n}$.

However, $y(\alpha_n,0) = y(\alpha_n,L) = y_\alpha(\alpha_n,0) = 0$

and

$$N_n = y_\alpha(\alpha_n,L)\, y'(\alpha_n,L) \qquad \text{(C-25)}$$

In terms of the Coulomb wave functions, this becomes

$$N_n = \left[\frac{x}{2} (F_o')^2 - \frac{\beta}{4\alpha_n} F_o' \frac{\partial F_o}{\partial \eta} \right]_{x=L} \qquad \text{(C-26)}$$

where $F_o(\eta,\rho) = F_o\left(\frac{\beta}{2\alpha_n}, \sqrt{\alpha}_n x\right)$ and $F_o' = \frac{\partial F_o}{\partial \rho}$.

Equation C-26 is not a simple evaluation of N_n, but it greatly facilitates the calculation because time-consuming numerical integration can be avoided.

Appendix D

Notes on Calculating the New Solution

The solution $n(r,\theta,\phi,t) = R(r,t)\ Q(\theta,\phi,t)$, as expressed by equations 5-13, 5-17, 5-23, and 5-32 through 5-37, has been implemented on the computer in FORTRAN IV via a main control program and 8 subprograms. These routines, which are shown with their linkages in Figure D-1, can be described as follows:

FO -- Calculates the regular Coulomb wave function $F_o(\eta,\rho)$. For $0 \leq \eta \leq 10$ and $0 \leq \rho \leq 30$, the standard power series is adequate, but for $\rho > 30$, the "asymptotic" expansion is necessary. A useful discussion of the methods for calculating this function at various locations in the $\eta - \rho$ plane has been given by Fröberg[67]. The most complete tables have been published by Tubis[68].

FOPR -- Calculates $F_o' = \partial F_o(\eta,\rho)/\partial\rho$. Again, both the power series and the asymptotic formula are used depending on the value of ρ.

FOZER -- Calculates the n^{th} zero of $F_o(\eta,\rho)$ by making an initial estimate of the zero and then closing in with Newton's method. This subprogram obviously uses both FO and FOPR.

DFODET -- Calculates $\partial F_o(\eta,\rho)/\partial\eta$ using the power series derived in the NBS Tables[69]. This method breaks down for $\rho > 30$ and $\partial F_o/\partial\eta$ is then calculated directly by varying $F_o(\eta,\rho)$.

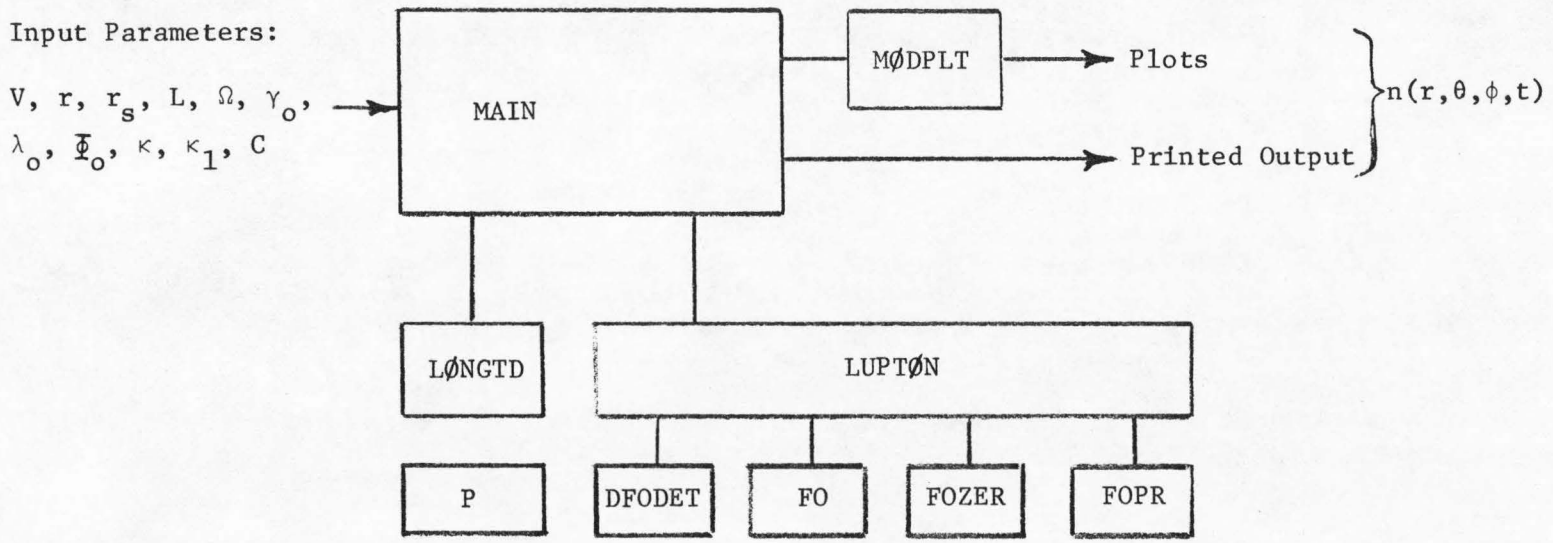

Figure D-1: Computer routines used to calculate the new solution. The input and output parameters are defined in Section V.

LUPTØN -- Calculates the new radial solution $R(r,t)$ using the subprograms FO, FOPR, FOZER and DFODET. Using the input parameters V, r, r_s, L, κ, t and NMAX, LUPTØN carries out the following operations:

a) Defines $\beta = V(2C-1)/\kappa$

b) Calculates the eigenvalues $\alpha(n)$ for n = 1, NMAX using FOZER.

c) Calculates the value of the normalization integral N_n for n=1, NMAX (see Appendix C) without any numerical integration using FOPR and DFODET.

d) Sums the eigenvalue series (Equation 5-32) and finds $R(r,t)$.

P -- Evaluates the Legendre polynomial $P_\ell(\gamma)$ using a recursion relation.

LØNGTD -- Calculates the azimuthal solution $Q(\gamma,t)$ via subprogram P for injection uniform over a cone of half-angle γ_o.

MAIN -- The main control program. Converts $Q(\gamma,t)$ into the function $Q(\gamma',t)$ including field spiral and corotation. Then MAIN either prints $n(r,\gamma',t)$ or plots n vs. t using MØDPLT.

REFERENCES

1. J. R. Jokipii, "Propagation of Cosmic Rays in the Solar Wind," Reviews of Geophysics and Space Physics, 9, 27, 1971.

2. J. R. Jokipii and E. N. Parker, "On the Convection, Diffusion, and Adiabatic Deceleration of the Cosmic Rays in the Solar Wind," Astrophys. J., 160, 735, 1970.

3. P. Meyer, E. N. Parker, and J. A. Simpson, "Solar Cosmic Rays of February 1956 and their Propagation through Interplanetary Space," Phys. Rev., 104, 768, 1956.

4. E. N. Parker, "The Passage of Energetic Charged Particles through Interplanetary Space," Planet. Space Sci., 13, 9, 1965.

5. J. R. Jokipii, "Cosmic Ray Propagation 1, Charged Particles in a Random Magnetic Field," Astrophys. J., 146 , 480 , 1966 .

6. J. R. Jokipii, "Cosmic Ray Propagation 2, Diffusion in the Interplanetary Magnetic Field," Astrophys. J., 149, 405, 1967.

7. J. R. Jokipii, "Addendum and Erratum to Cosmic-Ray Propagation 1," Astrophys. J., 152, 671, 1968.

8. E. C. Roelof, "Transport of Cosmic Rays in the Interplanetary Medi um," Canad. J. Phys., 46, 5990, 1968.

9. K. Hasselmann and G. Wibberenz, "Scattering of Charged Particles by Random Electromagnetic Field," Zeitschrift für Geophysik, 34, 353, 1968.

10. L. F. Burlaga, "Anisotropic Diffusion of Solar Cosmic Rays," J. Geophys. Res., 72, 4449, 1967.

11. L. A. Fisk and W. I. Axford, "Effect of Energy Changes on Solar Cosmic Rays," J. Geophys. Res., 73, 4396, 1968.

12. M. A. Forman, "Convection-Dominated Transport of Solar Cosmic Rays," J. Geophys. Res., 76, 759, 1971.

13. C. K. Ng and L. J. Gleeson, "On the Propagation of Solar Cosmic Rays," paper SOL-23 presented at the XIIth International Conference on Cosmic Rays, Hobart, Tasmania, August 1971.

14. C. K. Ng and L. J. Gleeson, to be published in Solar Phys., 1971.

15. K. G. McCracken, U. R. Rao, R. P. Bukata, and E. P. Keath, "The Decay Phase of Solar Flare Events," Solar Phys., 18, 100, 1971.

16. W. E. Althouse, E. C. Stone, R. E. Vogt, and T. H. Harrington, "A Solar and Galactic Cosmic Ray Satellite Experiment," IEEE Transactions on Nuclear Science, 15, 229, 1967.

17. S. S. Murray, "Propagation of 1-10 MeV Solar Protons in Interplanetary Space," Ph.D. Thesis, California Institute of Technology, 1970.

18. J. E. Lupton and E. C. Stone, "Measurements of Electron Detection Efficiencies in Solid State Detectors," to be published in Nucl. Instr. and Methods, 1971.

19. J. E. Lupton, "OGO-6 Electron Response," SRL Internal Report No. 28, California Institute of Technology, 1971.

20. E. Fermi, Nuclear Physics, Univ. of Chicago Press, Chicago, 1970, pp. 225-236.

21. E. C. Stone, "Local Time Dependence of the Non-Stormer Cutoff for 1.5 MeV Protons in the Quiet Geomagnetic Field," J. Geophys. Res., 69, 3577-3582, 1964.

22. T. A. Fritz and D. A. Gurnett, "Diurnal and Latitudinal Effects Observed for 10 keV Electrons at Low Satellite Altitudes," J. Geophys. Res., 70, 2485-2502, 1965.

23. J. F. Janni, Calculations of Energy Loss, Range, Pathlength, Straggling, etc., Tech. Report AFWL-TR-65-150, 1960.

24. L. C. Evans and E. C. Stone, "Access of Solar Protons into the Polar Cap: A Persistent North-South Asymmetry," J. Geophys. Res., 74, 5127, 1969.

25. F. B. McDonald, "Sattelite Observations of Solar Cosmic Rays," in Intercorrelated Satellite Observations Related to Solar Events, ed. by V. Manno and D. E. Page, D. Reidel Publ. Co., Dordrecht-Holland, 1970, pp. 34-52.

26. K. G. McCracken and U. R. Rao, "Solar Cosmic Ray Phenomena," Space Science Reviews, 11, 155, 1970.

27. Solar Geophysical Data, Vols. 299-307, World Data Center A, ESSA, Boulder, Colorado, 1969-70.

28. Solar Geophysical Data, IER-FB-294 (Supplement), "Descriptive Text," World Data Center A, ESSA, Boulder, Colorado, Febr. 1969.

29. L. D. Kavanagh, Jr., A. W. Schardt, and E. C. Roelof, "Solar Wind and Solar Energetic Particles: Properties and Interactions," Reviews of Geophys. and Space Phys., Vol. 8, No. 2, 389, 1970.

30. It was later discovered by the author that the D1 noise was correlated with the spacecraft exposure to sunlight and that the failure was probably caused by a broken Range Telescope mylar window.

31. S. S. Murray, E. C. Stone, and R. E. Vogt, "Interplanetary Deceleration of Solar Cosmic Rays," Phys. Rev. Letters, 26, 663, 1971.

32. A. J. Masley and P. R. Salterblom, "Solar Cosmic Ray Observations During the September and November 1969 Events," paper SOL-33 presented at the XIIth International Conference on Cosmic Rays, Hobart, Tasmania, August 1971.

33. Report UAG-13, "Data on the Solar Proton Event of Nobember 2, 1969 through the Geomagnetic Storm of November 8-10, 1969," compiled by D. B. Bucknaw and J. V. Lincoln, World Data Center A, NOAA, Boulder Colorado, 1971.

34. E. N. Parker, "Dynamics of the Interplanetary Gas and Magnetic Field," Astrophys. J., 128, 664, 1958.

35. E. N. Parker, "Cosmic Ray Modulation by the Solar Wind," Phys. Rev., 110, 1445, 1958.

36. S. M. Krimigis, "Interplanetary Diffusion Model for the Time Behavior of Intensity in a Solar Cosmic Ray Event," J. Geophys. Res., 2943, 1965.

37. J. E. Lupton and E. C. Stone, "Transport of Solar Flare Protons -- Comparison of a New Analytical Model with Spacecraft Measurements," paper SOL-22 presented at the XIIth International Conference on Cosmic Rays, Hobart, Tasmania, August 1971.

38. J. R. Jokipii and P. J. Coleman, Jr., "Cosmic Ray Diffusion Tensor and Its Variation Observed with Mariner 4," J. Geophys. Res., 73, 5495, 1968.

39. J. R. Jokipii and E. N. Parker, "Cosmic Ray Life and the Stochastic Nature of the Galactic Magnetic Fluid," Astrophys. J., 155, 799, 1969.

40. E. P. Keath, R. P. Bukata, K. G. McCracken, and U. R. Rao, "The Anomalous Distribution in Heliocentric Longitude of Solar Injected Cosmic Radiation," Solar Phys., 18, 503, 1971.

41. R. P. Bukata, U. R. Rao, K. G. McCracken, and E. P. Keath, "Observation of Particle Fluxes over Extended Solar Longitudes during the Solar Flare Event of March 31 to April 10, 1969," paper SOL-27 presented at the XIIth International Conference on Cosmic Rays, Hobart, Tasmania, Aug. 1971.

42. R. P. Lin, S. W. Kahler, and E. C. Roelof, "Solar Flare Injection and Propagation of Low-Energy Protons and Electrons in the Event of 7-9 July, 1966," Solar Phys., 4, 338, 1967.

43. J. Kunstmann and G. Webberenz, "The Structure of Interplanetary Space During the March 24, 1966 Solar Event," paper SOL-16 presented at the XIIth International Conference on Cosmic Rays, Hobart, Tasmania, Aug. 1971.

44. J. R. Jokipii, "Deceleration and Acceleration of Cosmic Rays in the Solar Wind," Phys. Rev. Letters, 26, 666, 1971.

45. L. J. Gleeson and I. D. Palmer, "On the Direct Observation of Cosmic-Ray Energy Losses," Astroph. and Sp. Sci., 12, 123, 1971.

46. I. D. Palmer, "Cosmic Ray Energy Losses at 1 AU during Solar Proton Events," paper SOL-25 presented at the XIIth International Conference on Cosmic Rays, Hobart, Tasmania, August, 1971.

47. I. H. Urch and L. J. Gleeson, "Energy Changes of Solar Cosmic Ray Particles," paper SOL-24 presented at the XIIth International Conference on Cosmic Rays, Hobart, Tasmania, August, 1971.

48. M. A. Forman, "Convection-Dominated Transport of Solar Cosmic Rays," paper SOL-26 presented at the XIIth International Conference on Cosmic Rays, Hobart, Tasmania, August, 1971.

49. K. G. McCracken, U. R. Rao, and R. P. Bukata, "Cosmic-Ray Propagation Processes, 1, A Study of the Cosmic-Ray Flare Effect," J. Geophys. Res., 72, 4293, 1967.

50. U. R. Rao, K. G. McCracken, F. R. Allum, R. A. R. Palmeira, W. C. Bartley, and I. Palmer, "Anisotropy Characteristics of Low Energy Cosmic Ray Population of Solar Origin," paper SOL-29 presented at the XIIth International Conference on Cosmic Rays, Hobart, Tasmania, August, 1971.

51. J. M. Wilcox and N. F. Ness, "Quasi-stationary Corotating Structure in the Interplanetary Medium," J. Geophys. Res., 70, 5793, 1965.

52. W. I. Axford, "Anisotropic Diffusion of Solar Cosmic Rays," Planet. Space Sci., 13, 1301, 1965.

53. L. F. Burlaga, "Anisotropic Solar Cosmic Ray Propagation in an Inhomogeneous Medium," presented at the XIth International Conference on Cosmic Rays, Budapest, Hungary, August, 1969.

54. J. R. Jokipii, "Modulation of Low Rigidity Cosmic Rays and the Power Law Spectrum of the Interplanetary Magnetic Field in 1962 and 1965," Canadian J. Phys., 46, 5950, 1968.

55. J. R. Jokipii, personal communication, 1971.

56. J. R. Jokipii, "Fokker-Planck Equations for Charged Particle Transport in Random Fields," preprint, California Institute of Technology, 1971.

57. K. G. McCracken, "Anisotropies in Cosmic Radiation of Solar Origin," in Solar Proton Manual, NASA Tech. Report R-169, ed. by F. B. McDonald, pp. 57-88, 1963.

58. R. C. Englade, "Effects of the Solar Boundary Condition on Flare-Particle Propagation," J. Geophys. Res., 76, 6190, 1971.

59. J. Feit, "Confinement of Solar Flare Cosmic Rays to Sections of the Corotating Solar Magnetic Field," J. Geophys. Res., 74, 5579, 1969.

60. M. Abramowitz and I. A. Stegun, Handbook of Mathematical Functions, Dover, New York, 1964, p. 538.

61. L. J. Gleeson and C. K. Ng, "Energy Changes of Cosmic Rays in Interplanetary Space," preprint, Monash University, Australia, 1971.

62. M. A. Forman, "The Equilibrium Anisotropy in the Flux of 10 MeV Solar Flare Particles and Their Convection in the Solar Wind," J. Geophys. Res., 75, 3147, 1970.

63. L. C. Evans, "OGO-4 Data Coverage Plots," SRL Internal Report No. 25, California Institute of Technology, 1971.

64. T. L. Garrard, "OGO-6 Monthly Summary Plots," SRL Internal Report No. 27, California Institute of Technology, 1971.

65. J. Mathews and R. L. Walker, Mathematical Methods of Physics, W. A. Benjamin, Inc., New York, 1965, pp. 162-171.

66. J. D. Jackson, Classical Electrodynamics, John Wiley and Sons, New York, 1963, pp. 67-69.

67. C. E. Fröberg, "Numerical Treatment of Coulomb Wave Functions," Rev. Mod. Phys., 27, 399, 1955.

68. A. Tubis, Tables of Non-Relativistic Coulomb Wave Functions, La-2150, Los Alamos Scient. Lab., Los Alamos, N. Mex., 1958.

69. National Bureau of Standards, Tables of Coulomb Wave Functions, Vol. I, Applied Math. Series 17, U. S. Govt. Printing Office, Wash., D. C., 1952.